

Influence of structural and electrostatic disorder on transport properties of monolayers of two-dimensional semiconductors

THÈSE N° 7678 (2017)

PRÉSENTÉE LE 19 MAI 2017

À LA FACULTÉ DES SCIENCES ET TECHNIQUES DE L'INGÉNIEUR
LABORATOIRE D'ÉLECTRONIQUE ET STRUCTURES À L'ÉCHELLE NANOMÉTRIQUE
PROGRAMME DOCTORAL EN MICROSYSTÈMES ET MICROÉLECTRONIQUE

ÉCOLE POLYTECHNIQUE FÉDÉRALE DE LAUSANNE

POUR L'OBTENTION DU GRADE DE DOCTEUR ÈS SCIENCES

PAR

Dmitry OVCHINNIKOV

acceptée sur proposition du jury:

Prof. E. D. N. Matioli, président du jury
Prof. A. Kis, directeur de thèse
Prof. J. Ye, rapporteur
Prof. G. Fiori, rapporteur
Prof. O. Yazyev, rapporteur



ÉCOLE POLYTECHNIQUE
FÉDÉRALE DE LAUSANNE

Suisse
2017

What thou lovest well remains,
the rest is dross
What thou lov'st well shall not be reft from thee
What thou lov'st well is thy true heritage

Ezra Pound
Canto LXXXI

To the ones I love

Acknowledgments

PhD thesis is a path which one takes in order to understand whether he or she is suitable for scientific research or other related activities. As soon as the main goal is to make a discovery of fundamental or practical use, this activity assumes work on something which nobody worked on before. A PhD student working in experimental physics learns several important steps on the way from project initiation to final result. Among them the most important are design of experiment, device fabrication, measurement techniques, data interpretation and scientific writing. I believe that interaction with people during a PhD work is very crucial. Both due to the knowledge transfer from senior to young scientists and due to the fact that two brains can be complementary to each other. During the last four years I interacted with many people, thus this section will be a bit more detailed than one would expect.

During my PhD work I had an opportunity to work in the laboratory with high scientific standards and to participate in a number of exciting projects and collaborations with the people inside the group and with external colleagues. I am very grateful to Prof. Andras Kis for giving me an opportunity to work in this group on a variety of projects spanning from electron microscopy to low temperature transport measurements. Especially I would like to thank Andras for providing me freedom to be creative, giving me time to find my way through the projects and for trusting my opinion.

Before moving on to my colleagues, I would like to acknowledge Prof. Elisa Matioli, Prof. Oleg Yazyev, Prof. Jianting Ye and Prof. Gianluca Fiori for being in my thesis jury, for careful reading of my thesis and for interesting questions and useful comments.

I would like to thank Dr. Adrien Allain for sharing his passion to science and for giving me huge amount of help on cryogenic measurements. I was happy to work in one team with such creative and structured mind and hopefully I was able to adsorb some knowledge from you.

I would like to thank Dr. Dumitru Dumcenco for providing his CVT and CVD crystals, as well as for collaboration with his former group in Taiwan, in particular with Prof. Ying-

Acknowledgments

Sheng Huang and Prof. Ching-Hwa Ho. The excellent crystals from Taiwanese group served as a basis for many exciting experiments.

I would like to acknowledge help of Kolyo Marinov and our collaboration on Kelvin Probe Force Microscopy. I can not enough express my appreciation for help on numerous occasions in the lab. I am also fascinated by his very unique sense of humour and by his ability to work very hard. Kolyo will always be an example of versatility and dedication for me.

Many thanks go to Yen-Cheng Kung for his wonderful engineering skills and his help on transfers of material, which speeded up some of the experiments which I was performing. I will never forget your strong character and your kind support during these years.

I would like to thank Ming-Wei Chen for our collaboration on his MBE material. Together we were able to perform a number of interesting experiments on both electron microscopy and polymer electrolyte gating of his material.

I am very grateful to Dr. Fernando Gargiulo from Prof. Oleg Yazyev's group for his creative approach to theoretical calculations and for his great help with understanding the unusual behaviour of ReS_2 with polymer electrolyte gating. Hours spent discussing near the white board in your office helped me to better understand transport physics and localization problem.

I am very grateful for tons of help from Dr. Oriol Lopez Sanchez on Raman characterization of ReS_2 samples and collaboration on variety of projects. I am constantly impressed by Oriol's dedication to work and ability to solve complex problems.

I would like to acknowledge collaboration with Dr. Daniele Vella from the group of Prof. Christoph Gadermaier. The months working with him were very intense and the output appeared to be productive.

I am grateful to Sajedeh Manzeli for our collaboration on a review paper and many interesting discussions. Very often struggling on my own experiments I was remembering your suspended devices and this thoughts encouraged me due to the fact that my stuff was much more easy to handle.

I would like to thank Dr. Ahmet Avsar for many discussions which we had during the last several months on (mostly) scientific subjects. Your professionalism, attitude, sense of humour and high scientific standards are of great value.

Special thanks go to Simone Bertolazzi for our work on early stages of my PhD thesis and for thorough advice and useful comments on my experiments. I would like to thank Dr. Dominik Sebastian Lembke for many of his useful suggestions and extreme expertise on device fabrication. Thank you also go to Francesca Volpetti and Dr. Nicolino Stasio, you are both an example to me as human beings and scientists. I would like to thank Dr. HoKwon Kim for working on his MOCVD samples and for collaboration on STEM/KPEEM measurements in Grenoble. I would like to thank the rest of my colleagues: Alberto, Anuj, Branimir, Daniil, Daria, Dmitrii, Jaiandong, Juan, Ke, Malik, Michael, Shikhar, Wei for help, advice and support. Although we did not work a lot together, our interactions throughout these years were great fun! I would like also to say big thank you to Prof. Aleksandra Radenovic and all her group members.

I am very grateful to people who helped me to learn transmission electron microscopy and who made some tricky experiments together with me. Thanks go to Dr. Duncan Alexander, who was very patient training me on several microscopes. I would like to say big thank you to Dr. Sorin Lazar from FEI for his extremely high level of microscopy imaging and for sharing numerous hints in sample preparation and imaging. I would like to also thank Dr. Davide Deiana, Dr. Marco Cantoni, Dr. Thomas Lagrange, Dr. Hanako Okuno, Dr. Emad Oveisi and Dr. Sergei Lopatin.

I would like to say thank all of my friends, old and new, who regardless of distance stayed in touch with me and from whom I was able to learn many things. Especially I would like to thank Elena Gorina for our long friendship and your beautiful mind. I would like to thank Artem, Daria, Esther, Lerika, Lucy, Marina, Martha, Mikhail, Stanislav and Veronika for showing me the world from different perspectives and constantly inspiring me. I would like also express appreciation to Mr. Oleg Buldakov and Mr. Dan Simmons.

I am grateful for my parents and my sister Maria for infinitely strong support and love which they have been giving to me throughout my life. I think the most precious thing in any family is the possibility of being yourself. I am happy to say that I had even more than that.

Finally, I would like to thank my dear Anna for staying with me and loving me. Love, support and understanding you gave me are extremely valuable. I am happy that we were able to explore many parts of this planet together. I believe that I've never met a person as strong and bright as you are.

Lausanne, May 2017

Dmitry Ovchinnikov

Abstract

Two-dimensional (2D) materials are under intensive investigation recently due to variety of electronic properties, ranging from insulators (h-BN) to semi-metals (graphene), semiconductors (MoS_2 , WSe_2) with wide variability of band-gap and correlated phases (NbSe_2 , TaS_2). Recently, focus of research has been moved from graphene, which is now a well understood material, towards less explored materials, in particular monolayers of semiconducting transition metal dichalcogenides (TMDCs) such as MoS_2 with direct band-gap in optical range (1.5 – 2eV) and potential towards scalable electronics applications immune to short channel effects.

This thesis in fact explores materials beyond exfoliated MoS_2 with the focus on electrical and structural properties of monolayers of WS_2 , ReS_2 and synthesized by means of chemical vapour deposition (CVD) monolayers of MoS_2 , MoSe_2 and WSe_2 .

Four main chapters discuss the following aspects of these materials. Chapter 4 studies in details transport properties of monolayer WS_2 for the first time. We demonstrate wide tuning of transport in this material from insulating regime through localized states to band-like transport with insulator to metal transition (MIT) in between, with mobilities $\mu_{\text{FE}} = 50 \text{ cm}^2 \cdot \text{V}^{-1} \cdot \text{s}^{-1}$ at room temperature. In Chapter 5 we employ electrolyte gating for fabrication of the first electric double-layer transistor (EDLT) based on monolayers and multilayers of ReS_2 . Furthermore, we employ this as a system for variation of electrostatic disorder and find an unusual and strong modulation in conduction band of ReS_2 . The discovered modulation of conductivity *via* controllable introduction of electrostatic disorder can help to understand this material as well as other ultrathin 2D systems and to optimize the design of devices based on them. In Chapter 6 we use atomically smooth sapphire for demonstration of first epitaxial monolayer MoS_2 growth. We can control the orientation of single-crystalline grains on the substrate and create large area continuous films, where grain boundaries between the grains have no impact on transport properties in contrast to other reports. Finally, Chapter 7 discusses further advances in CVD growth of TMDCs, with the first demonstration of ambipolar insulator to metal transition in devices, based on monolayers of MoSe_2 and WSe_2 .

In conclusion, this thesis establishes connection between transport properties of monolayers of 2D semiconductors and structural or electrostatic disorder. These results are important for both fundamental understanding of transport in two-dimensional materials

Abstract

and practical applications.

Keywords: Two-dimensional (2D) material, transition metal dichalcogenides (TMDC), molybdenum disulphide (MoS_2), molybdenum diselenide (MoSe_2) tungsten disulfide (WS_2), tungsten diselenide (WSe_2), rhenium disulfide (ReS_2), electric double layer transistor (EDLT), chemical vapour deposition (CVD), electrostatic disorder.

Résumé

Depuis quelques années les matériaux bidimensionnels font l'objet des études exhaustives grâce à la variété de leurs propriétés électroniques comme l'isolation (h-BN) de semi-métaux (graphène), de semi-conducteurs (MoS_2 , WSe_2) avec une grande variation de la bande interdite et les phases corrélées (NbSe_2 , TaS_2). Récemment, l'attention de la communauté scientifique a été détournée du graphène, qui est déjà bien étudié, aux matériaux qui sont moins étudiés : par exemple les monocouches de Transition métal dichalcogénide monolayers (TMDCs) comme MoS_2 avec la bande interdite directe dans le tétramètre optique (1.5 – 2eV) et le potentiel des applications électroniques évolutives à l'abri de l'effet de canal court.

Cette thèse explore les matériaux au-delà de MoS_2 exfolié avec le focus sur les propriétés électroniques et structurales des monocouches de WS_2 , ReS_2 et synthétisés par les moyennes du dépôt chimique en phase vapeur (CVD) de monocouches de MoS_2 , MoSe_2 et WSe_2 .

Les quatre premiers chapitres discutent des aspects mentionnés ci-dessus. Le Chapitre 4 vise à étudier en détails les propriétés de transmission de monocouche de WS_2 pour la première fois. Nous démontrons une vaste gamme de transmission de matériel de régime isolant d'états localisés à transmission avec l'isolation de métal de transition entre les deux, avec la mobilité $\mu_{\text{FE}} = 50 \text{ cm}^2 \cdot \text{V}^{-1} \cdot \text{s}^{-1}$ à la température ambiante. Dans le Chapitre 5, nous utilisons le déclenchement d'électrolyte pour la fabrication du premier transistor électrique de double-couche (EDLT) basé sur les monocouches et les multicouches de ReS_2 . Prochainement, nous utilisons ces derniers dans le système de variation de désordre électrostatique, et nous trouvons une modulation forte et anormale des propriétés de transmission de la bande de conduction de ReS_2 . Nous découvrons la modulation de la conductivité *via* introduction du contrôle de désordre électrostatique qui nous aide à comprendre des autres systèmes 2D ultra-minces et à modéliser des appareils basés sur eux. Dans le Chapitre 6, nous utilisons saphir atomiquement lisse pour démontrer la croissance sur monocouche épitaxiale MoS_2 . Nous pouvons contrôler l'orientation de monocristallins grains dans le substrat et créer les propriétés de transmission contrairement aux autres rapports. Finalement, dans le Chapitre 7, nous discutons les avancées dans la croissance de CVD de TMDCs, avec la démonstration de l'isolant ambipolaire de transition de métal dans les appareils basées sur les monocouches de MoSe_2 et WSe_2 .

Résumé

Dans la conclusion, la thèse établit la connexion entre les propriétés de la transmission électrique de monocouches de semi-conducteurs 2D et le désordre structural ou électrostatique. Les résultats obtenus sont très importants pour la compréhension fondamentale de la transmission de matériaux bidimensionnels et leur application pratique.

Mots-clés : matériaux bidimensionnels (2D), disulfure de molybdène (MoS_2), tungstène de diséléniure (WSe_2), disulfure de tungstène (WS_2), disulfure de rhénium (ReS_2), dépôt chimique en phase vapeur (CVD), désordre électrostatique.

Contents

Acknowledgments	i
Abstract	v
Contents	xi
List of Figures	xiii
1 Introduction	1
2 Properties and synthesis of TMDCs	3
2.1 Introduction	3
2.2 Crystal structure	3
2.3 Semiconductors	5
2.3.1 Optical properties	5
2.3.2 Valley physics in group VI TMDCs	7
2.4 Superconductivity	7
2.5 Devices and integrated circuits based on TMDCs	8
2.6 Contacts to 2D materials	10
2.7 Synthesis of TMDCs	11
2.7.1 Exfoliation	11
2.7.2 Molecular beam epitaxy	12
2.7.3 Chemical vapor deposition	12
2.7.4 Heterostructures	15
2.7.5 Conclusions	15
2.8 Conclusion & Outlook	15
3 Experimental techniques	17
3.1 Introduction	17
3.2 Device Fabrication Techniques	17
3.2.1 Electron-beam lithography	19
3.2.2 Metal evaporation	20
3.2.3 Etching	20

Contents

3.3	Electrical measurements	21
3.3.1	Field-effect transistor characterization	21
3.3.2	Electric double layer transistors	22
3.3.3	Polymer electrolytes used in this thesis	23
3.3.4	Typical measurement procedure for EDLT	23
3.4	Material characterization	24
3.4.1	Transmission electron microscopy	25
3.4.2	Kelvin probe force microscopy	26
4	Electrical Transport Properties of Single-Layer WS₂	31
4.1	Introduction	31
4.2	Results: Electrical Transport Properties of Single-Layer WS ₂	33
4.2.1	Device performance in air and in vacuum	34
4.2.2	Effect of in situ annealing on device characteristics at room temperature	34
4.2.3	Accuracy of electrical measurements	38
4.2.4	Choice of metal contact for monolayer WS ₂	38
4.2.5	Performance of FET based on monolayer WS ₂	39
4.2.6	Temperature-dependent electrical transport	40
4.2.7	Metallic state	41
4.2.8	Insulating state in 1L WS ₂	42
4.3	Conclusion & Outlook	44
5	Disorder engineering and conductivity dome in ReS₂ with electrolyte gating	47
5.1	Introduction	47
5.2	Electrostatic disorder	48
5.2.1	Disorder in graphene devices	48
5.2.2	Disorder in TMDCs	50
5.2.3	EDLT as a disorder modulating tool	51
5.3	Structural and electrical characterization of ReS ₂	53
5.4	Results: disorder engineering and conductivity dome in ReS ₂ with electrolyte gating	56
5.4.1	Monolayer ReS ₂ EDLT characterization	56
5.4.2	Temperature dependent transport in monolayer ReS ₂	59
5.4.3	Comparison with multilayers of ReS ₂	60
5.4.4	Insulating state at high carrier densities in multilayer ReS ₂	64
5.5	Theoretical calculations	66
5.5.1	Band structure of ReS ₂	66
5.5.2	Alternative explanations for conductivity suppression	67
5.5.3	Discussion and transport calculations	68
5.6	Evidence of disorder effect in different monolayer TMDCs	72

5.7	Follow-Up Work	73
5.8	Conclusion & Outlook	74
6	Epitaxial monolayer MoS₂	77
6.1	Introduction	77
6.2	Results: Epitaxial CVD MoS ₂	78
6.2.1	Substrate preparation and CVD growth	78
6.2.2	Structural characterization	82
6.2.3	Electrical properties of large area MoS ₂ films	84
6.2.4	Kelvin Probe Force Microscopy	86
6.3	Conclusion & Outlook	88
7	High-quality synthetic 2D transition metal dichalcogenide semiconductors	89
7.1	Introduction	89
7.2	Results: monolayer MoS ₂ grown with H ₂ S as sulfur source	89
7.2.1	Structural characterization by STEM	90
7.2.2	Transport properties at room temperature	92
7.2.3	Conclusions	93
7.3	Results: Band-like transport and ambipolar insulator to metal transition in CVD grown WSe ₂ and MoSe ₂	94
7.3.1	Electrolyte capacitance optimization	94
7.3.2	Ambipolar insulator to metal transition in CVD grown WSe ₂	95
7.3.3	Ambipolar insulator to metal transition in CVD grown MoSe ₂	97
7.3.4	Contact resistance in MoSe ₂	99
7.3.5	Disorder in MoSe ₂ EDLT	100
7.3.6	Conclusions	101
7.4	Conclusion & Outlook	101
8	Conclusion	103
	Abbreviations & Symbols	105
	Bibliography	127
	List of Publications	129
	Curriculum Vitae	131

List of Figures

2.1	Three main types of crystal structure of TMDCs within monolayer	4
2.2	Different types of stacking in bulk MoS ₂	4
2.3	Optical properties of MoS ₂	5
2.4	Optical properties of ReS ₂	6
2.5	Valley physics in TMDCs	7
2.6	Electronic and optoelectronic devices based on monolayer MoS ₂	9
2.7	Contacts to 2D materials	11
2.8	Bulk and thin flakes on TMDCs	11
2.9	Molecular Beam Epitaxy of 2D materials	13
2.10	CVD MoS ₂ grown on SiO ₂ substrates	14
2.11	CVD MoS ₂ grown on SiO ₂ substrates	15
3.1	Process flow illustration for fabrication of "directional" devices based on ReS ₂	18
3.2	Schematic of field-effect transistor and measurement scheme	21
3.3	Schematic of EDLT based on KTaO ₃	22
3.4	Principle of operation of transmission electron microscope	25
3.5	Schematic of electron-sample interaction in HAADF-STEM	26
3.6	Electronic energy levels of the sample and AFM tip	27
3.7	Example of graphene work function imaging by KPFM	28
4.1	Ionic liquid gating of WS ₂	32
4.2	Fabrication of monolayer WS ₂ field-effect transistor.	33
4.3	Characterization of double-layer WS ₂ transistor in vacuum and the effect of annealing.	35
4.4	Performance of the single-layer WS ₂ transistor in vacuum.	36
4.5	Saturation of four-probe mobility after 145 hours of <i>in situ</i> annealing for monolayer WS ₂ device	37
4.6	Accuracy of four-terminal measurements at room temperature	38
4.7	Contact quality of different metals to monolayer WS ₂	39
4.8	Contact quality of different metals to monolayer WS ₂	39
4.9	Performance of monolayer WS ₂ transistor.	40

List of Figures

4.10	Metal-insulator transition in monolayer WS ₂	41
4.11	Electrical transport in the insulating regime of single-layer WS ₂	43
5.1	Comparison between graphene samples	49
5.2	Electrical transport properties of semiconducting TMDCs encapsulated in h-BN.	50
5.3	Schematic cross section of interface between electrolyte and semiconducting channel in EDLT.	52
5.4	EDLT based on bulk WSe ₂	52
5.5	EDLT based on STO and the effect of electrostatic disorder	53
5.6	STEM micrograph of multilayer ReS ₂	54
5.7	Thickness calibration for ultrathin ReS ₂ flakes	55
5.8	Monolayer ReS ₂ FET performance in vacuum	55
5.9	EDLT based on ReS ₂	56
5.10	Room temperature monolayer ReS ₂ EDLT characterization	57
5.11	Anisotropy measurements for monolayer ReS ₂ at room temperature	58
5.12	Monolayer ReS ₂ EDLTs based on LiClO ₄ electrolyte	59
5.13	Effect of electrolyte deposition on temperature dependent transport in monolayer ReS ₂	60
5.14	Multilayer ReS ₂ EDLT	61
5.15	Anisotropy and Hall effect in ReS ₂	62
5.16	Hall effect measurements in trilayer ReS ₂	64
5.17	Insulating state at high carrier densities in ReS ₂	65
5.18	Band structure of ReS ₂	67
5.19	EDLT based on organic semiconductor rubrene	69
5.20	Potential distribution at different ionic concentrations on the surface of ReS ₂	71
5.21	Calculations of electronic transport for monolayer ReS ₂	72
5.22	Disorder in an EDLT based on monolayer TMDCs.	72
5.23	Disorder in EDLT based on monolayer MoS ₂	73
5.24	Multilayer ReS ₂ and the effect of disorder	74
6.1	Effect of annealing in air on the morphology of c-plane sapphire	79
6.2	CVD furnace setup	80
6.3	Epitaxial CVD MoS ₂ on sapphire substrates	81
6.4	Effect of sapphire surface annealing on the lattice orientation of CVD-grown MoS ₂	82
6.5	Relative orientation of crystal lattice and triangle edges	83
6.6	Diffraction patterns from different island orientations	84
6.7	Electrical properties of large-area monolayer MoS ₂	85
6.8	Electrical properties of large-area monolayer MoS ₂	86

6.9 Mapping the local electrical properties across grain boundaries in large-area monolayer MoS ₂	87
7.1 Monolayer CVD MoS ₂	90
7.2 Monolayer CVD MoS ₂ characterization	91
7.3 Characterization of field-effect transistor based on CVD MoS ₂	93
7.4 Capacitance extraction for EMIM-TFSI on monolayer WSe ₂ at 278K	95
7.5 Ambipolar insulator to metal transition in monolayer WSe ₂	96
7.6 Temperature dependence of field effect mobility in monolayer WSe ₂	97
7.7 EDLT based on monolayer MoSe ₂	97
7.8 Ambipolar insulator to metal transition in monolayer MoSe ₂	98
7.9 Temperature dependence of field effect mobility in monolayer MoSe ₂	99
7.10 Contact resistance in CVD-grown monolayer MoSe ₂	99
7.11 Electrostatic disorder effect on monolayer MoSe ₂	100

1 Introduction

The discovery of graphene [1, 2, 3] and subsequent Nobel prize in Physics moved attention of material scientist and electrical engineers towards two-dimensional (2D) materials, their fundamental physics and numerous practical applications. The family of 2D materials hosts a variety of crystals with a wide range of electronic properties, crystal structures and possible applications. Molybdenum disulphide (MoS_2) is a layered semiconductor, one of the family of transition metal dichalcogenides (TMDCs). These materials have been known since 1960s [4] and in fact MoS_2 was used as a lubricant due to atomically smooth surfaces and low friction between the layers. Nowadays, there is increase of interest to this particular type of 2D materials due to the fact that applications of semiconductors appear to be much more diverse than for example of semi-metals like graphene. Although graphene is a "clean" high-mobility system, due to absence of the band gap it is barely suitable for digital electronic applications.

2D semiconductors propose possible solution for the problem of scaling of electronic circuits, as soon as they are immune to short channel effects and have smooth interfaces [5]. Recent advances in fabrication of heterostructures point towards the possibility of "all 2D" circuits, where interconnects, dielectric and transistor operating channel all consist of 2D materials [6]. Another foreseen application of 2D semiconductors is in flexible electronics [7], where combination of high quality transport [5] and outstanding mechanical properties [8] could allow TMDCs to outperform organic electronics. From the fundamental point of view, similar to graphene, which was in fact re-discovered, monolayers of TMDCs have a rich hidden physics. For example, direct optical transitions, broken inversion symmetry and large spin-orbit interaction result in a number of interesting device concepts in fields of spintronics, as well as revival of interest to valleytronics, where a valley degree of freedom is proposed as an information carrier [9].

This thesis stands somewhere in between practical applications and fundamental studies. On the one hand we aimed to explore new materials and study their transport properties

Chapter 1. Introduction

with the target of transistor applications. Large amount of effort was put into understanding of structural and electrical properties of large-area synthetic materials, grown by chemical vapour deposition (CVD) technique in close collaboration with growth experts and theoreticians [10, 11]. Chapters 6 and 7 discuss high quality monolayers of MoS_2 , MoSe_2 and WSe_2 grown by CVD. On the other hand, this thesis approaches optimization of transistors from fundamental point of view. We tried to answer the following question - what do we need to know about the material, about the device itself, to design high-performance transistors? For this purpose we performed electrical transport measurements as a function of temperature and were able to shed light on transport mechanisms in different doping regimes. Chapters 4, 5 and 7 are dedicated to transport studies of monolayers of WS_2 [12], ReS_2 [13], MoSe_2 and WSe_2 . Another important contribution is the use of special type of device - electric double layer transistor (EDLT) based on ReS_2 as a system, where electrostatic disorder could be modulated [13]. This issue is discussed in details in Chapter 5. Electrostatic disorder appears to be a key quantity for careful device design, confirmed by recent transport measurements in "clean" graphene [14, 15] and TMDCs [16] samples. Finally, we discuss the contributions of this thesis to the overall knowledge on 2D semiconductors and provide a brief overview on the field of two-dimensional materials in Chapter 8.

2 Properties and synthesis of TMDCs

2.1 Introduction

Transition metal dichalcogenides in the form of layered crystals exhibit a rich plethora of electronic properties, arising mainly from their composition and crystal symmetry. Although this thesis covers mainly semiconductors of TMDCs, in particular MoS₂, MoSe₂, WS₂, WSe₂ and ReS₂, it is necessary to outline important properties of semiconductors (group VI and VII sulfides and selenides) as well as neighbouring materials and to review different structural phases. We will also discuss devices, based on 2D materials, problem of contact formation between 2D semiconductors and metals, as well as optical properties and spin-valley physics of 2D materials. Furthermore, we are going to discuss production methods of TMDCs, as soon as investigation of synthetic ultrathin TMDCs is an important part of this thesis. We find it more convenient not to revise in this Chapter certain topics, for instance, device physics, transport properties and electrostatic disorder. These topics will be discussed in details in Chapters 4 and 5.

2.2 Crystal structure

Transition metal dichalcogenides exist in several structural phases. We begin with the discussion of coordination of atoms within single layer of TMDC. In contrast to graphene, where a single layer of material consists of hexagonal lattice consisting of single sheet of carbon atoms, monolayer of TMDC consists of a layer of metal atoms sandwiched between two layers of chalcogen atoms. The side view of all 3 main phases is schematically shown on the bottom panels of Figure 2.1. Furthermore, the phases differ in coordination spheres of transition metal atoms, which could be either trigonal prismatic (H phases) or distorted octahedral (T phases).

Furthermore, the T phase can be further distorted (T prime phase), as shown on top

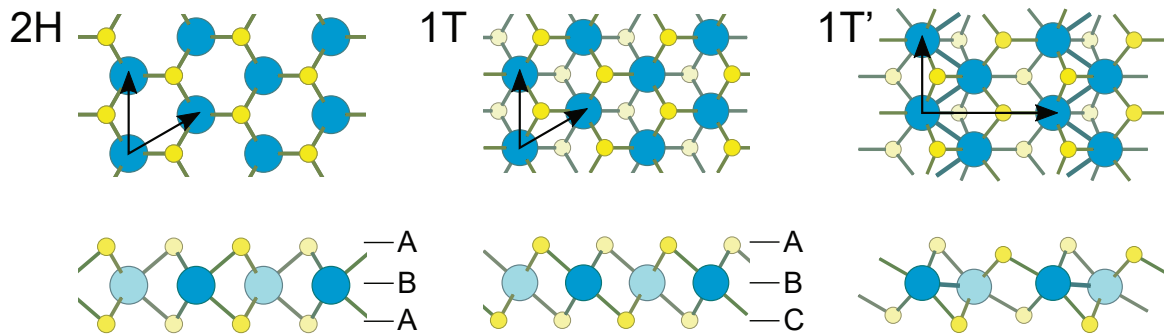


Figure 2.1 – Stick and ball models of three main types of crystal structure of TMDCs within monolayer.

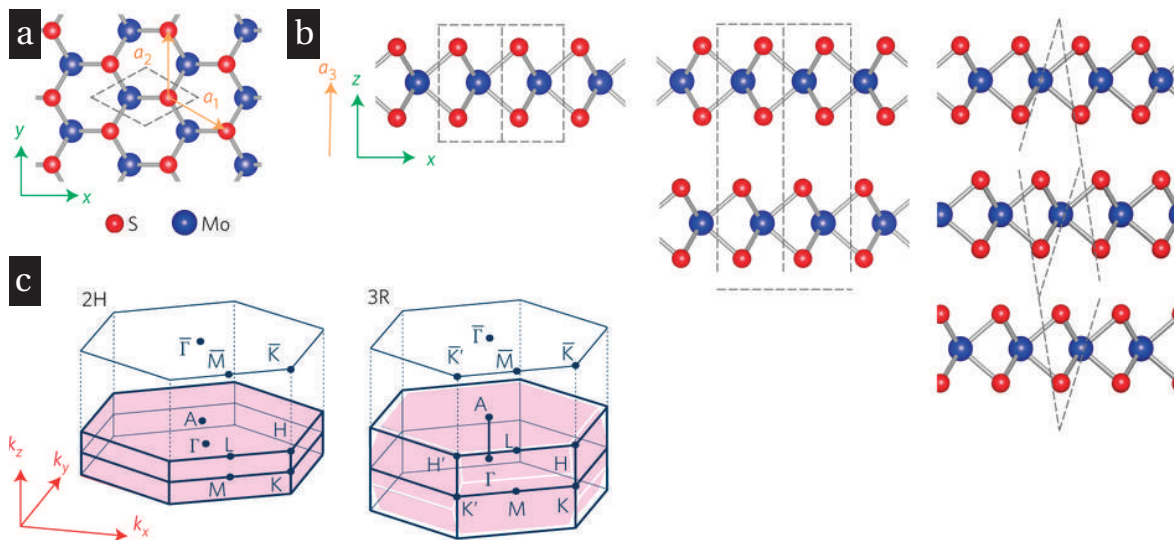


Figure 2.2 – Different types of stacking in bulk MoS₂. (a) Ball and stick top view of monolayer 2H MoS₂. (b) Side view on monolayer, 2H crystal and 3R crystal (from left to right). (c) First Brillouin zones of 2H- and 3R-MoS₂. Solid blue lines and pink shaded areas represent the conventional and primitive Brillouin zones, respectively. Reprinted by permission from Macmillan Publishers Ltd: [Nature Nanotechnology] R. Suzuki, M. Sakano, Y.J. Zhang, R. Akashi, D. Morikawa, A. Harasawa, K. Yaji, K. Kuroda, K. Miyamoto, T. Okuda, K. Ishizaka, R. Arita, and Y. Iwasa, "Valley-dependent spin polarization in bulk MoS₂ with broken inversion symmetry", *Nature Nanotechnology*, vol. 9, no. 8, pp. 611-617, © (2014).

panels of Figure 2.1. 1T prime phase is the pronounced case which leads to anisotropic optical properties, as will be discussed in Chapter 5 in case of ReS₂. Coming back to the side view, the above mentioned structural phases could be seen in terms of stacking order of three atomic planes. H phases would correspond to A-B-A stacking, while T phases correspond to A-B-C stacking.

When the layer stacking is fixed, different stacking configurations can be represented within the bulk. Typical example is 2H and 3R stacked MoS₂ is shown on Figure 2.2, Ref. [17].

Depending on particular combination of metal and chalcogen atoms in TMDCs, each would have a certain stable phase. For example, for five of six possible chemically distinct bulk TMDCs formed by the group VI transition metals (M = Mo, W; X = S, Se, Te) the 2H phase is the thermodynamically stable one, while the other can still be obtained in metastable form. There are more exotic compounds, for example ReS₂ with distorted 1T phase structure. Other, less prominent distortions can lead to charge-density-wave (CDW) phases formation, for example in group V chalcogenides (TaS₂, NbSe₂).

2.3 Semiconductors

2.3.1 Optical properties

One of the reasons for vast growth of interest to TMDCs is their optical properties. We revise below the most important of them. First is the transition from indirect to direct bandgap, which is happening, when the material is thinned down to monolayer limit [18, 19].

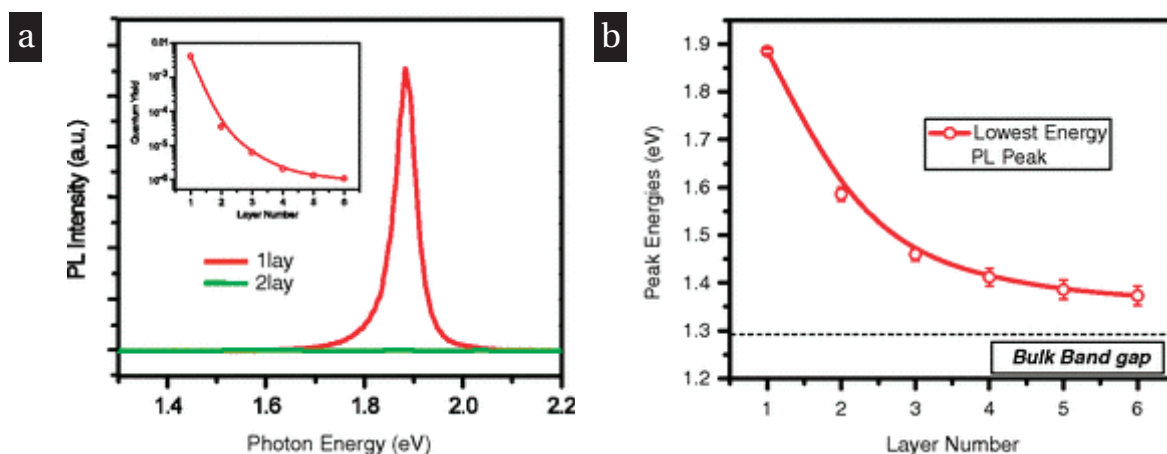


Figure 2.3 – Optical properties of MoS₂. (a) Normalized photoluminescence intensity for mono- and bilayer MoS₂. Inset - quantum yield as a function of layer number. (b) Photoluminescence peak energy as a function of layer number. Reprinted with permission from K.F. Mak, C. Lee, J. Hone, J. Shan and T. F. Heinz "Atomically thin MoS₂: a new direct gap semiconductor", *Physical Review Letters*, vol. 105, no. 13, p. 136805, © (2010) by the American Physical Society.

This was clearly observed in the very first experiments [18, 19], where photoluminescence (PL) intensity was significantly higher in monolayers than in bulk samples (Figure 2.4a),

while PL quantum yield decreased dramatically in thicker layers. Movement of peak towards lower energies (Figure 2.4b) suggested significant band structure differences in monolayers and bulk samples. The reason behind PL enhancement is the transition from indirect to direct bandgap. The respective values of the band gap calculated using density functional theory are 0.88 eV and 1.71 eV [20]. Other important properties due to 2D nature of these materials are excitons which have extremely high binding energies [21] and possibility to excite and emit light with certain helicity [22]. The latter will be discussed in the following Section 2.3.2.

In case of group VII dichalcogenides, for example ReS₂ and ReSe₂ due to different crystal structure the band structure and optical transitions are different. ReS₂ was believed to be a direct gap semiconductor from monolayer to bulk form [23]. Recent independent experiments on optical adsorption [24] and ionic liquid gating [25] on multilayers, however, argue with this hypothesis, clearly showing that the lowest energy transition has indirect nature.

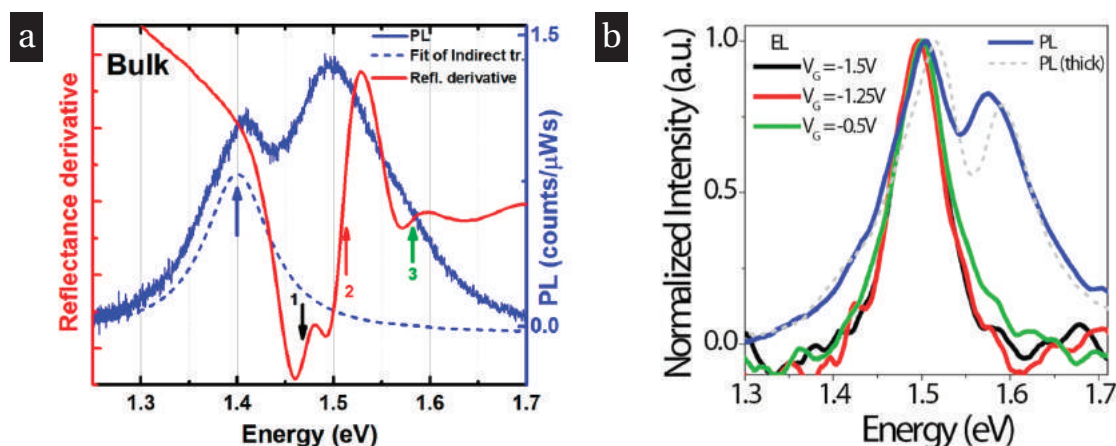


Figure 2.4 – Optical properties of bulk ReS₂. (a) Photoluminescence and reflectance measurements on bulk ReS₂. Adapted with permission from O.B. Aslan, D.A. Chenet, A. M. van der Zande, J.C. Hone and T.F. Heinz, "Linearly polarized excitons in single- and few-layer ReS₂ crystals", *ACS Photonics*, vol. 3, no. 1, pp. 96-101, © (2016) American Chemical Society. (b) Photoluminescence and electroluminescence from light-emitting transistors based on bulk ReS₂ flakes. Adapted from I. Gutiérrez-Lezama, B.A. Reddy, N. Ubrig, and A.F. Morpurgo, "Electroluminescence from indirect band gap semiconductor ReS₂", *2D Materials*, vol. 3, no. 4, p. 045016, © (2016) IOP Publishing Ltd.

Another distinct feature of ReS₂, which will be discussed from the point of view of electrical transport in Chapter is crystal anisotropy. This in turn gives rise to optical response anisotropy, for instance linear polarization of excitons [24]. In ReS₂ anisotropy in optical properties can be directly correlated with crystal structure [26].

2.3.2 Valley physics in group VI TMDCs

Optical properties of discussed semiconductors gave revival to the field of valleytronics. The possibility of manipulation of so-called valley degree of freedom, where the valley index of carriers is considered as information carrier, dates back to the 1970s, when it was studied in Si and inversion layers [27, 28]. However, this topic was much less explored than for example spintronics, as soon as valley energy splitting was more difficult to manipulate.

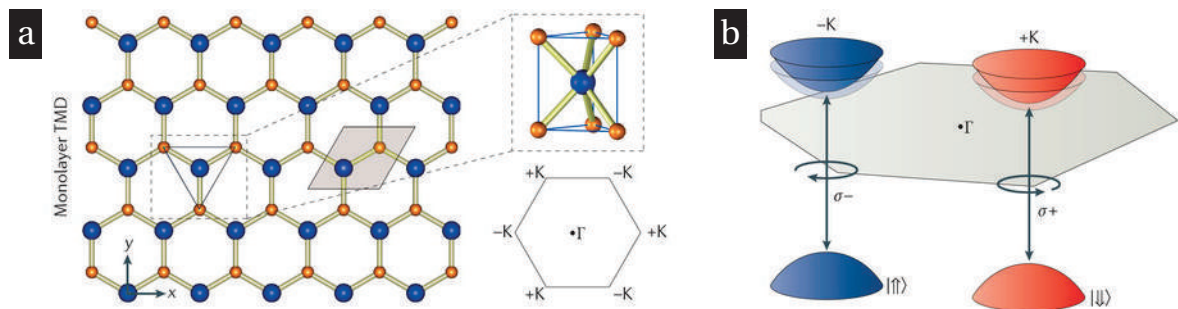


Figure 2.5 – Valley physics in TMDCs. (a) Crystal structure of 2H TMDC, top view. (b) Simplified band diagram, showing two valleys $-K$ and $+K$ and corresponding optical transitions. Adapted by permission from Macmillan Publishers Ltd: [Nature Reviews Materials] J.R. Schaibley, H. Yu, G. Clark, R. Rivera, J.S. Ross, K.L. Seyler, W. Yao, and X. Xu, "Valleytronics in 2D materials", *Nature Reviews Materials*, vol. 1, p. 16055, © (2016).

One of the unique characteristics of group 6 TMDCs is the broken inversion symmetry in monolayer limit (Figure 2.5a), which leads to the fact that the topmost valence band is located at two inequivalent points of Brillouin zone, which can be labelled as $+K$ and $-K$ (Figure 2.5a). Furthermore, in TMDCs, where spin-orbit coupling is very pronounced, the spin splitting has opposite signs in opposite valleys. This leads to coupling between spin and valley physics [29]. Furthermore, each valley can be addressed optically, for instance with circular polarized light [22]. Monolayers, however, are not only hosts of valley phenomena. For instance, bulk 3R-MoS₂ exhibits similar valley-dependent properties [17]. We refer to comprehensive reviews on the discussed topic in Ref. [9, 30].

2.4 Superconductivity

Due to variety of materials in TMDCs family, many of them can exhibit intrinsic or induced superconducting state at low temperatures. We will briefly discuss these materials, although superconducting materials were not studied in the framework of this thesis. The reason is close relationship between doping induced superconductivity in TMDCs and ionic liquid gating technique. Also, interesting connections between valley physics and superconductivity could be found.

All bulk TMDCs, which exhibit CDW state behavior, also exhibit superconductivity, with exception of NbS₂, which is known to be only superconducting [31]. While some TMDCs exhibit intrinsic superconductivity, in others it can be induced by electrostatic doping, chemical doping or applied pressure. The examples of materials which exhibit both superconductivity and CDW behavior include 2H NbSe₂, TaS₂, TaSe₂ [32, 33, 34, 35]. It is important to notice, that superconductivity persists in the 2D limit. Recently, the very first evidence of truly two-dimensional intrinsic superconductivity in TMDCs was reported for monolayer 2H-NbSe₂ [36]. Further characterization showed, that superconducting state in two dimensions is of Kosterlitz-Thouless type [37] with characteristic current-voltage dependence near critical temperature [38]. It appears that in monolayer limit superconducting state is significantly different from the bulk, not only in critical temperature, but also with enhancement of in-plane critical field, which is required to destroy superconducting state [38]. The current understanding of such behavior suggests, that it arises from the combination of reduced dimensionality and strong spin-orbit coupling [39]. In a 2H-phase monolayers of TMDCs spin-splitting in the valence band can be seen as effective magnetic field, which pins spins of electrons in Cooper pairs in out-of plane direction. Similar to intrinsic superconductivity, superconductivity can be induced in bulk and monolayer group VI TMDCs by electrostatic doping, for example by ionic liquid gating. At charge accumulation around 10^{14}cm^{-2} MoS₂, MoSe₂ and WS₂ appear to be superconducting [40, 41, 42, 43]. We point on the fact, that doping-induced superconductivity in bulk TMDCs samples has a 2D nature, as soon as doping is inhomogeneous and only layers, close to the surface are doped. Experiments on bulk MoS₂ with similar to Ref. [38] Ising-pairing support this hypothesis [44, 45]. It is interesting to notice, that all reports on doping induced superconductivity in semiconducting TMDCs so far have reached superconducting state for electrons, while materials like 2H NbSe₂, which exhibit intrinsic superconductivity, can be seen as heavily hole-doped MoSe₂. This demonstrates, that there are many open questions and discoveries to be made in this vast topic. The reader is referred to recent review on superconductivity in two-dimensional crystalline systems for more details [46].

2.5 Devices and integrated circuits based on TMDCs

Although physics of TMDCs is rich and diverse, as discussed in previous sections, the very first foreseen practical applications are integrated circuits and optoelectronic devices. These applications and current progress are briefly discussed in this section.

Bulk TMDCs are known from the 1960s and transport properties of bulk crystals were extensively investigated at that time [4]. Although the properties of first crystals were impressive, the modulation of bulk carrier density is barely possible, especially in case

2.5. Devices and integrated circuits based on TMDCs

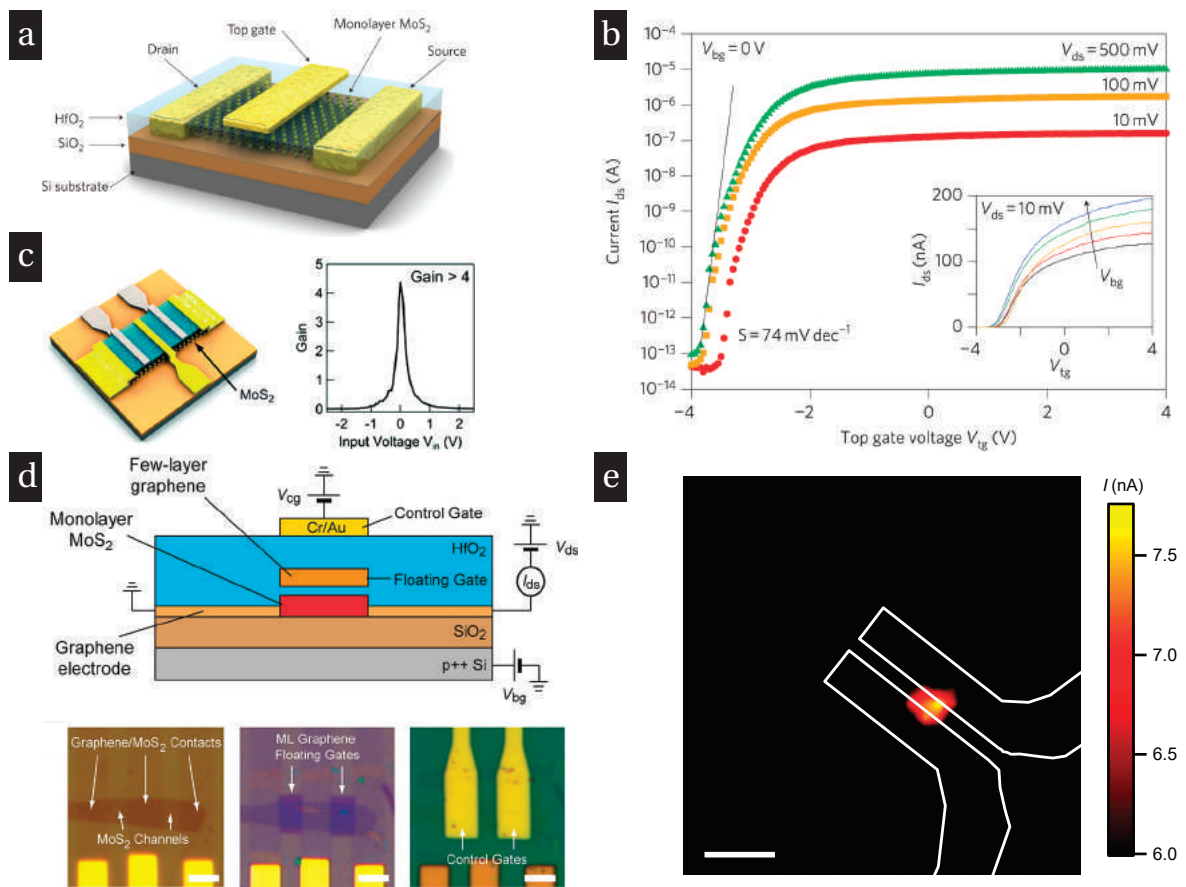


Figure 2.6 – Electronic and optoelectronic devices based on monolayer MoS₂. (a) Schematic representation of the dual-gated device, based on monolayer MoS₂. (b) Current-top gate voltage characteristic I_{ds} - V_{tg} at different values of drain-source bias V_{ds} . (a, b) adapted by permission from Macmillan Publishers Ltd: [Nature Nanotechnology] B. Radisavljevic, A. Radenociv, J. Brivio, V. Giacometti, and A. Kis, "Single-layer MoS₂ transistors", *Nature Nanotechnology*, vol. 6, no. 3, pp. 147-150, © (2011). (c) Schematic representation of MoS₂ inverter and gain as a function of input voltage. Adapted from B. Radisavljevic, M.B. Whitwick, and A. Kis, "Small-signal amplifier based on single-layer MoS₂", *Applied Physics Letters*, vol. 101, p. 043103, 2012, with the permission of AIP Publishing. (d) Top panel - schematic cross section of a memory cell, based on 2D materials - MoS₂ as an active channel and graphene as a trapping layer. Bottom panel - heterostructure fabrication for flash-memory cell. Adapted from S. Bertolazzi, D. Krasnozhan, and A. Kis, "Nonvolatile memory cells based on MoS₂/graphene heterostructures", *ACS Nano*, vol. 7, pp. 3246-3252, 2013, © (2013) American Chemical Society. (e) Photocurrent map for photodetector based on monolayer MoS₂. Scale bar - 5 μ m. Adapted by permission from Macmillan Publishers Ltd: [Nature Nanotechnology] O. Lopez-Sanchez, D. Lembke, M. Kayci, A. Radenovic, and A. Kis, "Ultrasensitive photodetectors based on monolayer MoS₂", *Nature Nanotechnology*, vol. 8, no. 7, pp. 497-501, © (2013).

of doped crystals, which leads to poor I_{on}/I_{off} ratio at room temperature [48]. Even with ionic liquid gating, which can lead to very high charge accumulation, carrier density

modulation is barely possible in bulk samples [49]. In this respect the demonstration of high-performance device based on monolayer MoS₂ by Radisavljevic and co-authors [5] was a breakthrough, with the possibility of modulation of current by 8 orders of magnitude and almost perfect subthreshold swing (SS) values of 74 mV/dec (Figure 2.6a,b). As soon as potential of monolayer MoS₂ was fully revealed, a number of studies demonstrated different types of integrated circuits [50]. Inverters, as shown on Figure 2.6c could have gain value up to 4. Furthermore, first heterostructures emerged, which were used to fabricate flash-memory cell [47], the schematic is shown on Figure 2.6d. MoS₂ although having lower mobility of charged carriers than for instance graphene can be employed in fabrication of radio-frequency devices [51, 52]. Finally, optoelectronic devices, employing direct bandgap of monolayer MoS₂ with high sensitivity were demonstrated [53]. Other optoelectronic devices include for instance solar-cell demonstration [54], polarized light-emitting diodes [55], electroabsorption modulator [56].

2.6 Contacts to 2D materials

The choice of contacting material for efficient carrier injection into 2D semiconductor is a crucial topic being under intensive investigation. High contact resistances can degrade the output characteristic of the resulting device. In semiconductor technology based on Si low resistance contacts are achieved by degenerate doping of material by means of ion implantation. Bulk semiconductor to metal contact can appear by means of covalent bonds formation, as shown on Figure 2.7a, while 2D materials in general lack dangling bonds and the contact can be formed either in presence of vdW gap (Figure 2.7b) or by alloying between metal and semiconductor (Figure 2.7c).

At the moment state of the art contacts to 2D semiconductors are in fact formed by means of approach, similar to semiconducting industry, when part of material is transformed from semiconducting 2H phase to metallic 1T phase (similar to ion implantation which turns semiconductor into degenerately doped semiconductor). 1T phase is furthermore contacted by metal, which provides a low resistance ohmic contact [57]. Another approach, proven to be robust even for low temperature studies, is ionic liquid gating, with low resistance contacts to intrinsic semiconductors such as monolayer WSe₂ demonstrated [58]. This technique will be discussed in details in Chapter 3, while in Chapters 5 and 7 it will be used for low resistance contacts to ReS₂, MoSe₂ and WSe₂. Furthermore, such approaches as molecular doping of the contact region [59], as well as contacting of 2D semiconductors by means of graphene are being extensively investigated [16]. The interested reader can refer to recent review on this topic by Allain et al., Ref. [60].

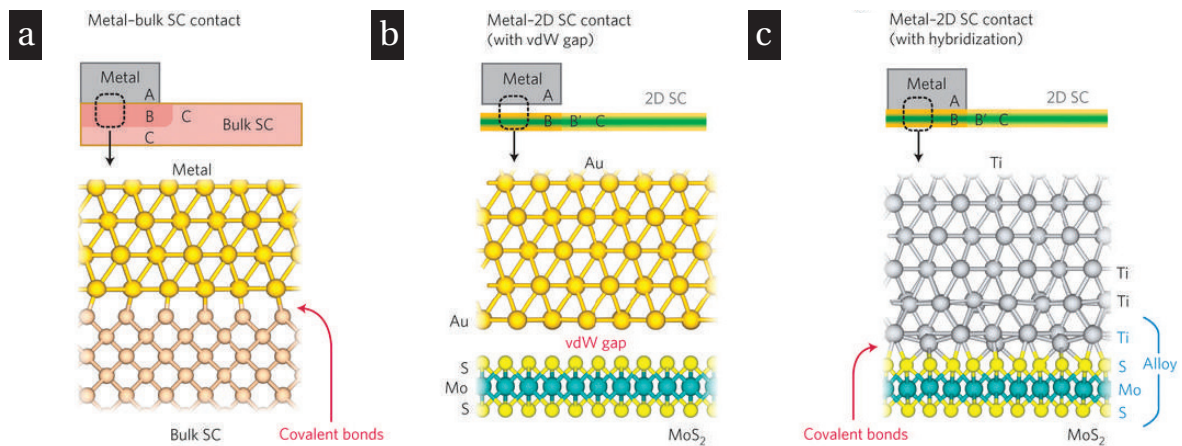


Figure 2.7 – Contacts to 2D materials. (a) Metal-bulk semiconductor contact. (b) Metal - 2D semiconductor contact with vdW gap. (c) Metal - 2D semiconductor contact with covalent bonds formation. Reprinted by permission from Macmillan Publishers Ltd: [Nature Materials] A. Allain, J. Kang, K. Baneree, and A. Kis, "Electrical contacts to two-dimensional semiconductors", *Nature Materials*, vol. 14, no. 12, pp. 1195-1205, © (2015).

2.7 Synthesis of TMDCs

2.7.1 Exfoliation

MoS₂ is the only TMDC which is abundant in nature, typical crystal is shown on Figure 2.8a. Other bulk crystals can be grown by means of chemical vapor transport (CVT) method, where slow cooling of three-zone furnace is used for high quality synthetic crystals growth [61]. Already in 1960s properties of bulk TMDCs were studied in details [4]. We refer to the detailed review for further details on bulk crystals growth [62].

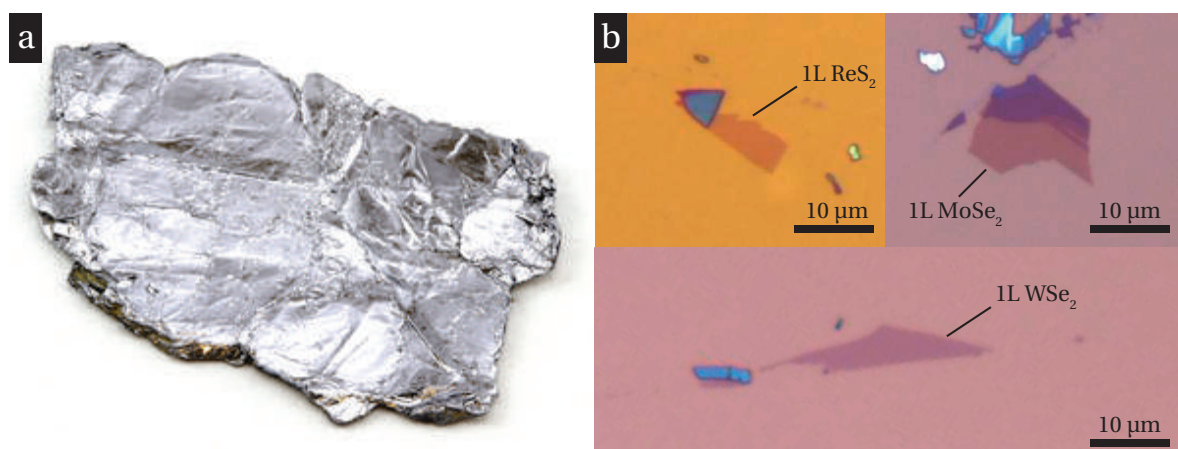


Figure 2.8 – (a) Optical micrograph of mined MoS₂ crystal. (b) Optical micrographs of thin flakes of ReS₂, MoSe₂ and WSe₂.

Furthermore, these crystals can be mechanically exfoliated and deposited on arbitrary substrates. Monolayer flakes of ReS₂, MoSe₂ and WSe₂ are shown on Figure 2.8b. The initial requirements for fast device fabrication with this method require bulk crystals, adhesive tape and optical microscope for flake detection. First high-performance devices were prepared on this type of material [5]. Exfoliation has contributed significantly to fast prototyping of devices. However, irregular shape of the flakes, limited size and no obvious root towards scalability pushed researchers to further explore production methods. One example is liquid phase exfoliation, with first reports dating back in 1970s [63]. Recently, this method is being reconsidered and successfully employed for a wide variety of studies, where large area homogeneous films are required [64, 65]. The main disadvantage of this method is low electrical quality of material, which might originate from stitching between the small flakes of material [66].

2.7.2 Molecular beam epitaxy

One of the scalable methods, which were developed on the early stages of research of TMDCs for large area production of material was the molecular beam epitaxy (MBE). An ultra-high vacuum (UHV) chamber with the pressure typically below 10^{-10} mbar contains several sources (in the case of MoSe₂ growth these are Mo and Se) to form molecular beams. Deposition is performed on the pre-heated substrate with *in-situ* thickness and substrate crystallinity monitored by reflection high-energy electron diffraction (RHEED). The Koma group has published numerous reports on the MBE growth of TMDCs in the 1980's and 1990's, with successful growths of MoSe₂, GaSe on a number of substrates, including other layered materials [67, 68]. The example of MBE growth of GaSe is shown on Figure 2.9a with triangular GaSe islands. Recent advances in electron microscopy allowed to resolve the atomic structure of MBE-grown material. For example, Figure 2.9b demonstrates MoSe₂ grown on SiO₂ with multiple dislocations and grain boundaries observed [69]. Electrical measurements on similar material reported high-resistance samples and hopping conduction through localized states [70]

Current status of MBE-grown TMDCs material suggest that this method is more suitable for fundamental studies. MBE chambers combined with scanning tunnelling microscopy (STM) or angle-resolved photoelectron spectroscopy (ARPES) provide access to intrinsic properties of air-sensitive materials [36, 71].

2.7.3 Chemical vapor deposition

Chemical vapor deposition (CVD) is probably the most practical method for synthesis of high-quality TMDCs. In this section we briefly revise current state of the art in CVD growth.

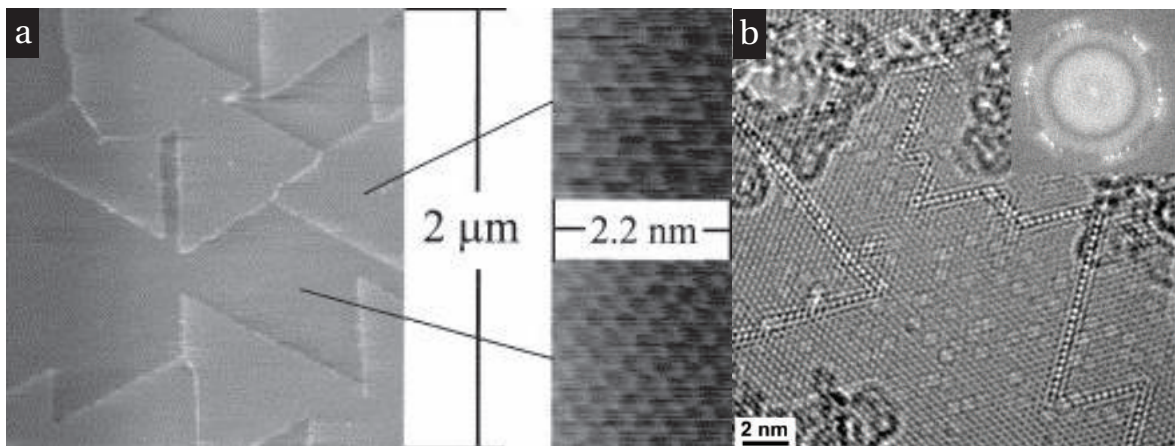


Figure 2.9 – (a) Optical micrograph of MBE grown GaSe. Reprinted from "Van der Waals epitaxy for highly lattice-mismatched systems", *Journal of Crystal Growth*, vol. 201-202, A. Koma, pp.236-241, © (1999), with permission from Elsevier. (b) TEM micrograph of MBE-grown MoSe₂ on SiO₂. Adapted with permission from O. Lehtinen, H.-P. Komsa, A. Pulkin, M.B. Whitwick, M.-W. Chen, T. Lehnert, M.J. Mohn, O.V. Yazyev, A. Kis, U. Kaiser, and A.V. Krasheninnikov, "Atomic Scale Microstructure and Properties of Se-Deficient Two-Dimensional MoSe₂", *ACS Nano*, vol. 9, no. 3, pp. 3274-3283. © (2015) American Chemical Society.

Important contribution in this field was the development of process, which can result in large monolayer domain growth on SiO₂ substrates [72, 73].

Optical micrograph of as-grown islands of MoS₂ is shown on Figure 2.10a with well defined islands of triangular shape. The as grown domains on SiO₂ have good optical and electrical properties with room temperature field-effect mobilities in the order of $5 \text{ cm}^2 \cdot \text{V}^{-1} \cdot \text{s}^{-1}$. As soon as triangles merge, they form different types of grain boundaries. The example is shown on Figure 2.10c, where grain boundary is investigated by means of scanning transmission electron microscopy (STEM). The formed grain boundaries in turn contribute to transport properties of large area films. On Figure 2.10d mobility and ON/OFF ratio as a function of channel length is plotted [74]. The decay of mobility is attributed to scattering on grain boundaries, as well as bilayer formation.

It is important to notice, however, that the single crystal performance of CVD material could be comparable with exfoliated counterparts [75]. In particular, samples grown on SiO₂ substrates and transferred on fresh SiO₂ substrates show n-type doping and metal-insulator transition. These measurements are summarized on Figure 2.11, where four-probe measurements were performed and metal-insulator transition with band-like transport was observed.

Our contribution to this field, in particular, development of epitaxial CVD MoS₂ growth with superior structural and electrical quality will be discussed in Chapter 6.

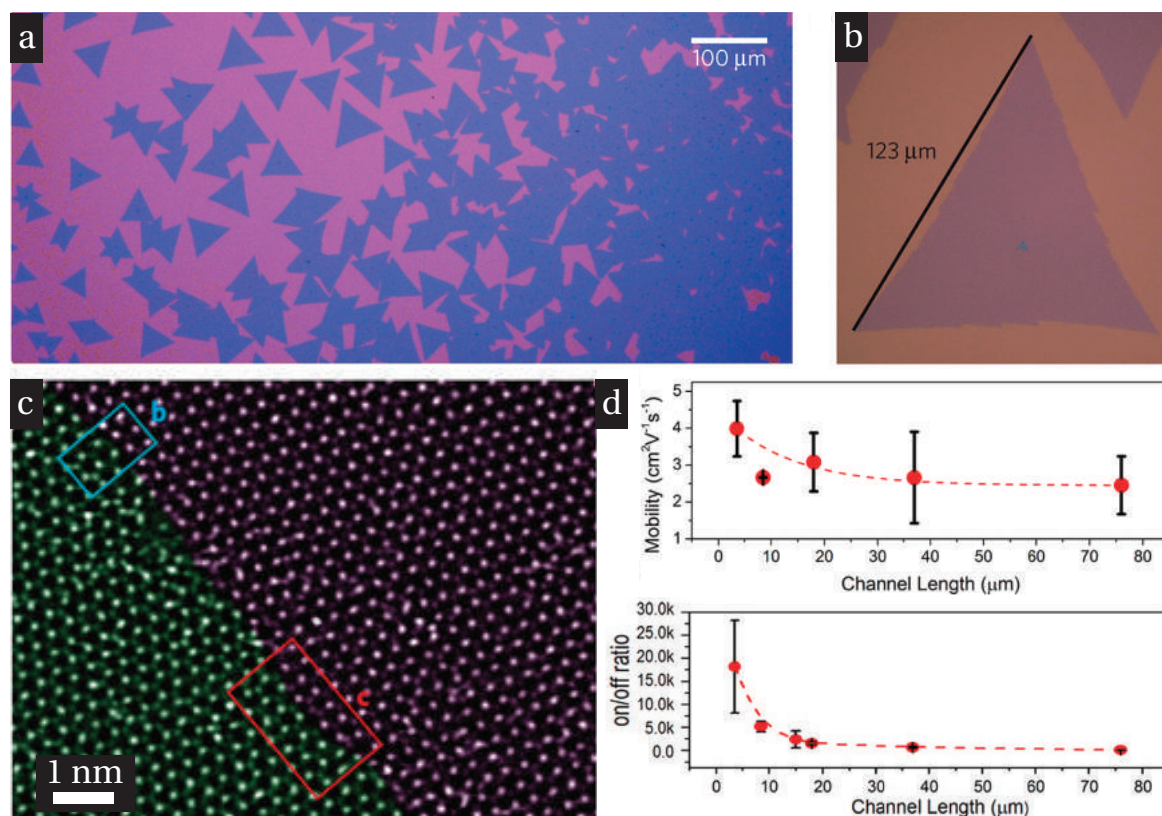


Figure 2.10 – CVD MoS₂ grown on SiO₂ substrates. (a, b) Optical micrographs of as grown flakes. Adapted by permission from Macmillan Publishers Ltd: [Nature Materials] A.M. van der Zande, P.Y. Huang, D.A. Chenet, T.C. Berkelbach, Y. You, G.-H. Lee, T.F. Heinz, D.R. Reichman, D.A. Muller, and J.C. Hone, "Grains and grain boundaries in highly crystalline monolayer molybdenum disulphide", *Nature Materials*, vol. 12, no. 6, pp. 554-561, © (2013). (c) STEM micrograph of grain boundary between two misoriented flakes. Adapted by permission from Macmillan Publishers Ltd: [Nature Materials] S. Najmaei, Z. Liu, W. Zhou, X. Zou, G. Shi, S. Lei, B.I. Yakobson, J.-C. Idrobo, P.M. Ajayan, and J. Lou, "Vapour phase growth and grain boundary structure of molybdenum disulphide atomic layers", *Nature Materials*, vol. 12, no. 8, pp. 754-759, © (2013). (d) Electrical properties of as-grown films as a function of channel length. Adapted with permission from S. Najmaei, M. Amani, M.L. Chin, Z. Liu, A. G. Birdwell, T.P. O'Regan, P.M. Ajayan, M. Dubey, and J. Lou, "Electrical transport properties of polycrystalline monolayer molybdenum disulfide", *ACS Nano*, vol. 8, no. 8, pp. 7930-7937, © (2014) American Chemical Society.

Standard CVD methods, developed in TMDCs growth community, rely on solid phase precursors. This approach is good enough for fast prototyping of devices, however, it lacks the control over precursor fluxes and pressures. A step forward was introduction of metal-organic CVD (MOCVD), which is based on the use of gas phase precursors [76, 77]. In fact, the first MOCVD reports of TMDC synthesis dating back to 1990s [76]. Recently, wafer-scale synthesis of MoS₂ and WS₂ on various substrates with good electrical properties was demonstrated [77].

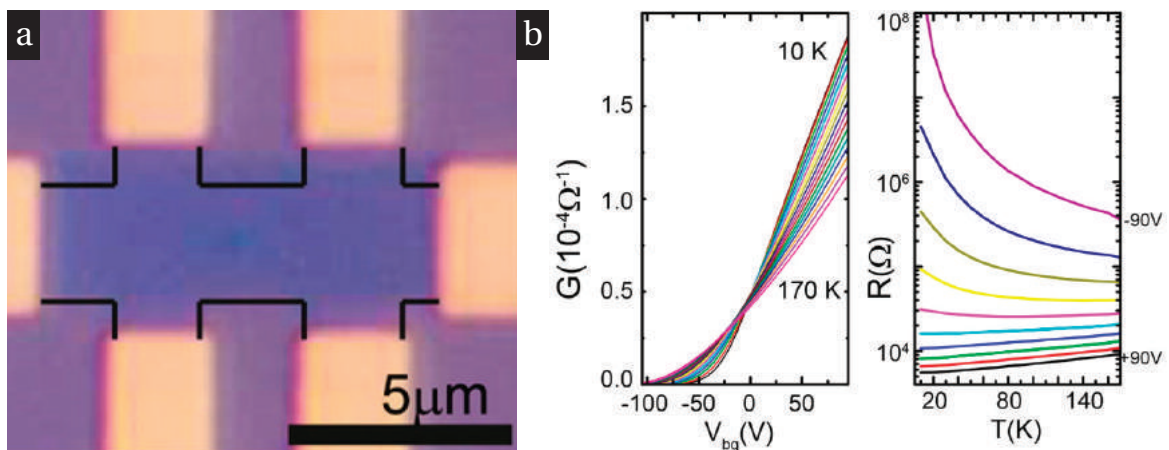


Figure 2.11 – CVD MoS₂ grown on SiO₂ substrates (a) Optical micrograph of monolayer MoS₂ sample in four-probe geometry. (b) Metal-insulator transition in monolayer MoS₂. Adapted with permission from H. Schmidt, S. Wang, L. Chu, M. Toh, R. Kumar, W. Zhao, A. H. Castro Neto, J. Martin, S. Adam, B. Özyilmaz, and G. Eda, "Transport Properties of Monolayer MoS₂ Grown by Chemical Vapor Deposition", *Nano Letters*, vol. 14, no. 4, pp. 1909-1913. © (2014) American Chemical Society.

2.7.4 Heterostructures

CVD technique appears to be useful for growth of different types of in plane and out of plane heterostructures. Growth of atomically sharp interfaces is essential step towards future practical applications. Especially these types of heterostructures are important for realization of p-n junctions and light emitting diodes. The universal approach with use of solid precursors which are introduced sequentially during the growth was employed for growth of in plane heterostructures between monolayers of different TMDCs [78, 79, 80].

2.7.5 Conclusions

In the last five years there has been a strong increase of interest in synthesis of ultrathin two-dimensional semiconductors. First devices have been fabricated employing exfoliated material and up to now clean and high mobility samples have been obtained using mostly exfoliated material. On the other hand, strong demand for highly reproducible and scalable methods led to development of several growth techniques. CVD is now the most widely used method, which allows to get high quality material on large area.

2.8 Conclusion & Outlook

This Chapter provided a general overview of important points related to optical, electrical, structural and electronic properties of 2D semiconductors. This overview is by no means

Chapter 2. Properties and synthesis of TMDCs

full and interested reader can refer to mentioned review articles.

3 Experimental Techniques

3.1 Introduction

Work on this thesis involves three main experimental directions. First is device fabrication, which involves plethora of standard microfabrication techniques. Second is electrical transport measurements, including measurements of material in standard field effect transistor configuration (FET) and electric double layer transistors (EDLT) measurements as a function of temperature and magnetic field. Third, we employed material characterization techniques, mainly scanning transmission electron microscopy (STEM), transmission electron microscopy (TEM), selected area electron diffraction (SAED) and atomic force microscopy (AFM) with focus on surface workfunction measurement (KPFM). We notice that these instrumentation techniques are now a standard for solid state physics research and we will discuss them without going deep into details.

3.2 Device Fabrication Techniques

Many materials, including graphene and TMDCs, exhibit different properties depending on the amount of carriers inside conducting channel. It is thus convenient to use field-effect transistor (FET) geometry to be able to modulate the carrier density inside the channel. Monolayer TMDCs flakes have typical size of 10-20 μm , have arbitrary shape (especially in case of exfoliated material) and are randomly distributed on silicon chips. It is thus convenient to use electron beam lithography to define contacts and etching mask for each particular flake. Depending on the material and desired carrier injection metals with different work function can be evaporated.

To provide the reader with quick overview on one of process flows used for simple devices with the back gate we provide details in the list below and show key steps on Figure 3.1. The reader will find variations depending on device design and particular experiment

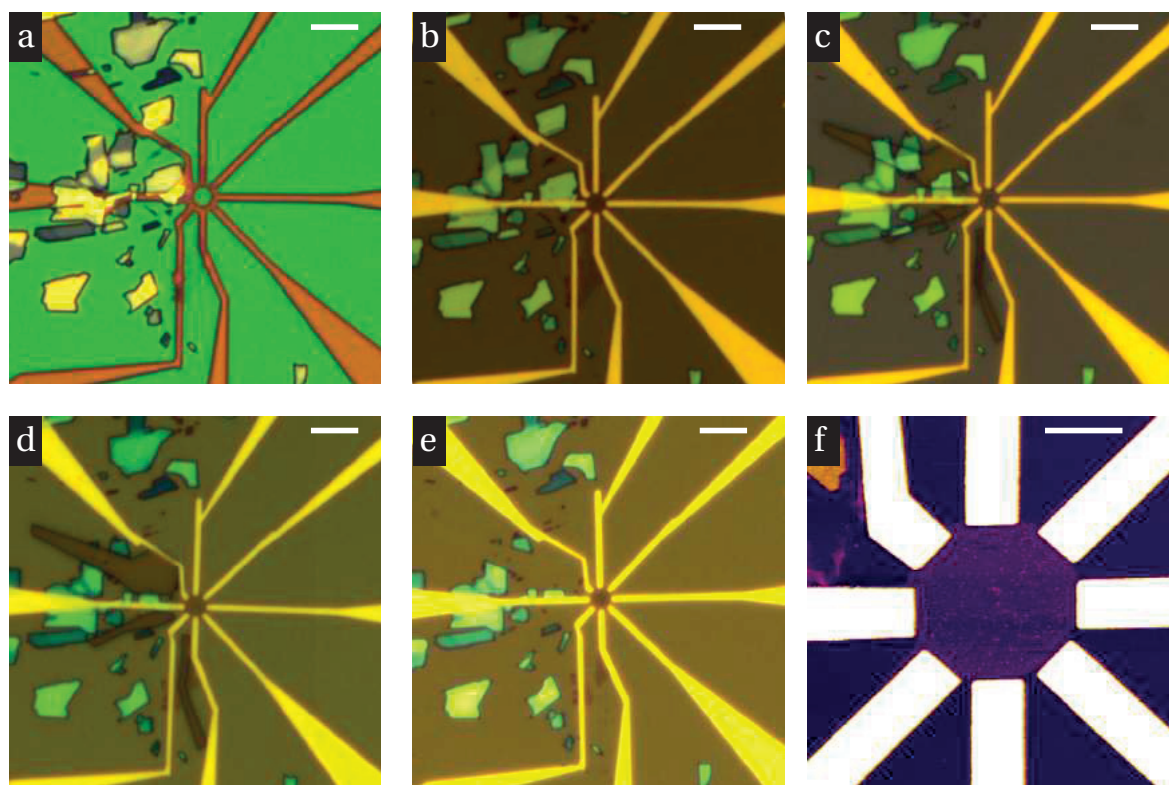


Figure 3.1 – Process flow illustration for fabrication of "directional" devices based on ReS_2 . (a) Optical microscope image of first step of EBL on ReS_2 flake. Scale bar - $5 \mu\text{m}$. (b) Optical microscope image after liftoff. Scale bar - $5 \mu\text{m}$. (c) Optical microscope image of second step of EBL for etching mask patterning on ReS_2 flake. Scale bar - $5 \mu\text{m}$. (d) Optical image after etching in the mixture of SF_2 and O_2 plasma for 30s. Scale bar - $5 \mu\text{m}$. (e) Optical image of the final device after dissolving of resist in acetone. (a-e) Scale bar - $5 \mu\text{m}$. (f) Atomic force microscope image of the same device. Scale bar - $1 \mu\text{m}$.

throughout this thesis. In the list below we describe preparation of sample which has circular shape. It consists of etched ReS_2 flake with 8 contacts, where resistance in different crystal directions can be measured passing current through opposite contact pairs:

1. Exfoliation of TMDCs bulk crystals (in this case ReS_2) on Si/SiO_2 substrates.
2. Identification of flakes on Si/SiO_2 by means of optical microscopy and atomic force microscopy (see Section 5.3 for more details).
3. Spin coating of MMA EL6 resist at 4000 rpm. for 60 sec., bake chip on hotplate for 5 min. at 180°C .
4. Spin coating of PMMA A2 resist at 1500 rpm. for 60 sec., bake chip on hotplate for 5 min. at 180°C .
5. E-beam lithography.

6. Develop in MIBK:IPA 1:3 mixture for 3 min. Rinse with IPA and dry with N₂ gun. Sample after development is shown on Figure 3.1a.
7. Deposition of 50 nm of Pd in *Leybold Optics LAB 600H*.
8. Lift off in Acetone overnight at room temperature.
9. Rinse with Acetone, IPA and dry with N₂ gun. Sample after the lift-off process is shown on Figure 3.1b.
10. Spin coating of PMMA A4 at 4000 rpm. for 60 sec., bake chip on hotplate for 5 min. at 180 °C.
11. E-beam lithography to define regions, which will be further exposed to plasma.
12. Develop in MIBK:IPA 1:3 mixture for 4 min. Rinse with IPA and dry with N₂ gun. Sample after development is shown on Figure 3.1c.
13. Dry etching in *Alcatel 601E* - 30 sec. SF₆ plasma, power 300W, 12 sec. O₂ plasma, power 300W. Our sample after the etching process is shown on Figure 3.1d.
14. Strip the resist in Acetone overnight at room temperature.
15. Rinse with Acetone, IPA and dry with N₂ gun. Final images of the sample are shown on Figure 3.1e, f.

Furthermore, we comment on each fabrication step.

3.2.1 Electron-beam lithography

Electron-beam lithography (EBL) is a powerful tool for exposure of arbitrary shape patterns with high spatial resolution. We employ *Vistec EBPG5000* available in EPFL Center of micronanotechnology (CMi). Briefly, a focused beam of electrons with high energy (100 keV in our case) is used to expose selected regions on the substrate, covered with e-beam sensitive resist. Polymer chains break under electron beam and the exposed area can be further removed by the so-called development process, where chip is exposed to solvents, which selectively dissolve damaged polymer regions. Size of the beam as well as the dose can be pre-selected by user. Pattern can be designed in variety of programs, in our case we used DesignCAD Express 18. For further details of EBL please refer to comprehensive review on the topic in Ref. [81].

Furthermore we comment on the resists and development process. In our process flow we employ methyl methacrylate (MMA) EL6 and polymethylmethacrylate (PMMA) A2

stack for liftoff. It can be seen on Figure 3.1a that contacts seem to merge in the closest parts of our structure. However, this is simply effect of undercut, as soon as bottom layer of MMA EL6 is more sensitive than PMMA A2 to the e-beam dose we use. This makes subsequent lift-off process more easy. No shunts are revealed by later inspection of final structure on Figure 3.1f.

We used mixture of methyl isobutyl ketone (MIBK) and isopropyl alcohol (IPA) with the volume ratio of 1:3 to develop the regions, where polymer chains were broken. For more reproducible results we used constant mixing of MIBK:IPA mixture. This provides smooth developed areas with minimum resist residues.

3.2.2 Metal evaporation

For metal evaporation we used two types of evaporation tools available in CMI. We used automatic evaporator *Leybold Optics LAB 600H* for evaporation of such metals as Ag, Au, Pd, Pt, Cr. Typical base pressure for evaporation in this tool is 1.5×10^{-6} mbar. In case more accurate control over the evaporation rate and vacuum in the system was required, we used *Alcatel EVA600*, where both electron-beam and thermal evaporation by Joule effect were available. This tool allows evaporation with the base pressure of $\sim 2 \times 10^{-7}$ mbar, which allows to have controllable results with sensitive to oxidation metals such as Ti or Co.

3.2.3 Etching

Before etching, we performed a second step of EBL to open the area of the flake, which should be removed by plasma (Figure 3.1c). For etching we use a layer of PMMA A4, spin coated at 4000 rpm., which provides a 200 nm thick film. The thickness of resist determines how much time we can further etch due to resist sensitivity to plasma exposure. We used *Alcatel 601E*, where constant temperature of the substrate was used to achieve reproducible results. Typical gases employed were O_2 for monolayers etching or SF_6 plasma with subsequent short exposure to O_2 plasma for removal of SF_6 residues (in case of multilayers). The sample after etching is shown on Figure 3.1d, where thick flakes shunting our electrodes together with irregular thin pieces were removed. Finally, on Figure 3.1e, f we show the device after removal of PMMA A4 in acetone. Figure 3.1f shows the final circular structure, which is ready for measurements of two-probe resistance of the sample in different directions. Such measurements for ReS_2 samples will be discussed in Section 5.4.1.

3.3 Electrical measurements

Traditional field effect transistors (FET) rely on the modulation of carrier density inside the semiconducting channel. In this section we provide an overview of measurement details, instruments and techniques we used to measure different types of transistors.

3.3.1 Field-effect transistor characterization

Overview of typical four-probe device, used to extract four-terminal resistance, is shown on Figure 3.2. Heavily-doped Si substrate is used as a global back gate for modulation of carrier density inside semiconducting channel. Four-terminal sample of rectangular shape is defined by means of process flow similar to discussed in Section 3.2.

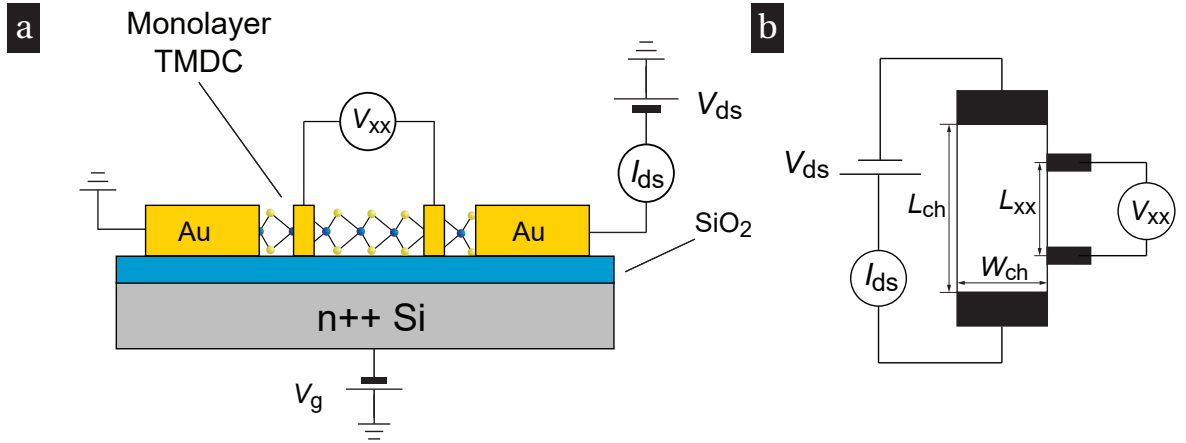


Figure 3.2 – (a) Schematic of field-effect transistor and (b) measurement scheme.

Constant DC voltage V_{ds} is applied between drain and source electrodes with the simultaneous measurement of drain-source current I_{ds} , while side electrodes are used to measure voltage drop V_{xx} across the length between them L_{xx} . In this way sheet conductivity G_{sh} could be extracted:

$$G_{sh} = \frac{I_{ds}}{V_{xx}} \frac{L_{xx}}{W_{ch}}. \quad (3.1)$$

Sheet conductivity is a normalized quantity which allows to compare samples and to extract such quantities as field-effect mobility or Hall-effect mobility. These quantities will be introduced in further chapters.

Drain-source voltage was applied and current was measured by means of Agilent E5270B, Keithley K2400 or Keithley 2450. Similarly, one of these instruments was used to apply gate voltage V_g and to monitor gate leakage current I_g . For voltage measurements, depending

on the resistance of the sample, different voltmeters were used. For low resistance samples, we used Stanford Research Systems SR560 or Keithley 2000 multimeters, for high resistance samples we used electrometers Keithley 6514 with input impedance above 200 T Ω m.

3.3.2 Electric double layer transistors

Electric double layer transistors (EDLT) rely on the use of ionic liquids (IL) or polymer electrolytes (PE) as gating media instead of solid gates. This device will be used in Chapters 5 and 7 of this thesis and in this section we are going to discuss some advantages of EDLT and then provide details on polymer electrolytes used and typical measurements performed in the framework of this thesis.

To illustrate the main features of this technique, we refer to illustration on Figure 3.3 from Ref. [82]. Typically, the sample is patterned in the Hall-bar geometry and furthermore IL or PE is applied on top (Figure 3.3a). Ionic liquids in general work in a way, that ions are mobile inside, while electronic conductivity is minimized. When the external gate voltage is applied, ions migrate depending on their charge (Figure 3.3b). Thus on top of the channel thin layer of high density ions is formed. Typical distance between the ions and channel can be as small as 1-2 nm, thus providing very high capacitance per unit area. One of the type of ions $[\text{DEME}]^+ [\text{BF}_4]^-$ used is shown on Figure 3.3c.

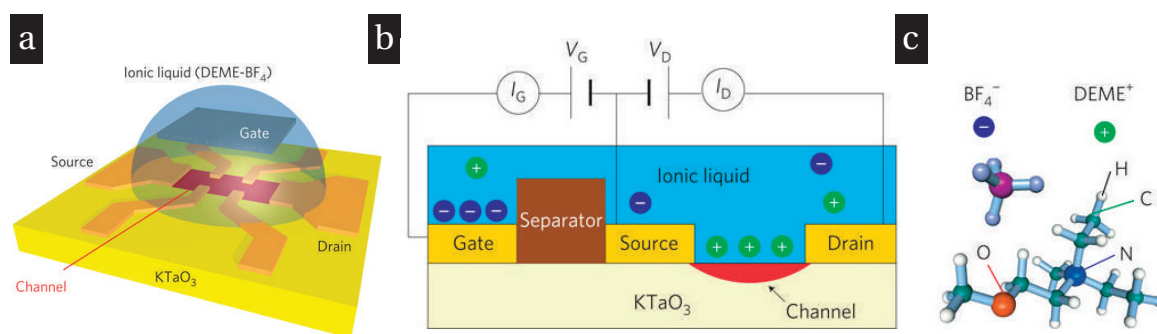


Figure 3.3 – Schematic of EDLT based on KTaO_3 . (a) Illustration of the sample. (b) Cross-section of the device. (c) Ions $[\text{DEME}]^+ [\text{BF}_4]^-$. Adapted by permission from Macmillan Publishers Ltd: [Nature Nanotechnology] K. Ueno, S. Nakamura, H. Shimotani, H. T. Yuan, N. Kimura, T. Nojima, H. Aoki, Y. Iwasa, and M. Kawasaki, "Discovery of superconductivity in KTaO_3 by electrostatic carrier doping", *Nature Nanotechnology*, vol. 6, no. 7, pp. 408-412, © (2011).

Furthermore, we revise several important features of EDLT:

- High carrier densities achieved, up to 10^{15}cm^{-2} for ZnO EDLT [83].
- High electric fields accessible, up to several $\text{V} \cdot \text{nm}^{-1}$ [49].

- Doping is reversible in contrast to chemical or electrochemical doping.
- Low contact resistances reported for intrinsic TMDCs, which is critical for accurate low temperature measurements [58, 60].
- This technique is complementary to scanning tunnelling spectroscopy (STS), where the electrical gap could be extracted without complicated ultra high vacuum (UHV) chambers and low temperatures [25, 84, 85].
- Variations of this technique can be used for example for controllable intercalation of Li^+ ions in layered materials [86].
- The drawback of this decrease of mobility in EDLTs [13, 87] in comparison with "clean" samples. This issue will be discussed in details in Chapter 5.

3.3.3 Polymer electrolytes used in this thesis

In this thesis we did not use ionic liquids, instead of that we used polymer electrolytes. First, we found better mechanical stability of samples and possibility to perform multiple cooldowns with the same sample without any damage with PE. Second, IL were effectively used for gating of bulk SrTiO_3 [87], KTaO_3 [82] or TMDCs [40, 42], while some groups reported variation of doping in TMDCs [42, 43]. The latter was interpreted as local detachment of ionic liquids from the interface. In our case we were able to measure multiple samples with the chosen PE. Typically, 10 cooling cycles without any sample damage could be done with reproducible doping results. Examples will be shown in Chapters 5 and 7.

The recipes we used for PE preparation are listed below:

1. Mixture of [EMIM]-[TFSI] (918 mg) and PS-PMMA-PS (68 mg) prepared in anisole (8874 mg) [88]. The mixture was stirred for 5h at room temperature.
2. 1:8 mixture of LiClO_4 and polyethylene oxide (PEO) in acetonitrile (10% weight) [58].
3. LiClO_4 (302.4 mg) and PEO (1009 mg) dissolved in 15 ml of methanol [86].

3.3.4 Typical measurement procedure for EDLT

The procedure used for typical EDLT sample is described below:

1. Sample preparation is similar to discussed in Section 3.2 with additional large area electrode, isolated from the sample and used to apply polymer electrolyte voltage V_{PE} .

Chapter 3. Experimental techniques

2. Bake sample for 10 min. at 110 °C at hot plate in glove box filled with Ar.
3. Spin coat PE in Ar atmosphere.
4. Wired sample is loaded in vacuum chamber or cryostat, pumped below 10^{-6} mbar, annealed at 330 – 350K. We point on the fact that high vacuum and annealing are crucial for reproducible results.
5. Furthermore, measurements could be performed.

Measurements were performed in several ways. One way is to study conductivity as a function of temperature for fixed doping:

1. Apply V_{PE} at temperature above freezing point of electrolyte, stabilize the current
2. Perform cooldown with fixed speed - we typically used $0.5 - 3K \cdot \text{min}^{-1}$.

Another is to vary the carrier density with solid back gate, which is integrated in our structures:

1. Apply V_{PE} at temperature above freezing point of electrolyte, stabilize the current.
2. Cool down below freezing point of electrolyte.
3. Turn on the back gate, sweep V_{bg} at fixed temperature, decrease the temperature with fixed cooling rate ($0.5 - 3K \cdot \text{min}^{-1}$), repeat.

In this way at fixed value of V_{PE} it is possible to study a range of carrier densities, modulated with V_{bg} .

3.4 Material characterization

In the framework of this thesis we used several material characterization techniques. Transmission electron microscopy (TEM) was used to characterize crystal structure, lattice and defects in 2D semiconductors. Atomic force microscopy (AFM) was employed for characterization of surfaces. Kelvin probe force microscopy (KPFM) was used to map the workfunction of material and thus to reveal electrical inhomogeneities in our material.

3.4.1 Transmission electron microscopy

Transmission electron microscopy is widely used in this thesis for material characterization. We used two main instruments, available in Interdisciplinary Centre for Electron Microscopy (CIME) - *JEOL 2200FS* for transmission electron microscopy (TEM), selected area electron diffraction (SAED) and *Titan Themis* (FEI), which has spherical aberration correction, this instrument was used for high-resolution scanning transmission electron microscopy (STEM) studies.

The schematic, representing 3 main modes of TEM operation is shown on Figure 3.4. High energy parallel beam of electrons passes through thin specimen. Depending on apertures and imaging conditions, different kind of images can be projected on camera. For example, on Figure 3.4a so-called intermediate lens is turned off and selected area aperture is inserted, which results in diffraction pattern (DP) projected on camera. This mode is so-called selected area electron diffraction (SAED) mode, in which elastically scattered electrons form a DP from the area, limited by selected area aperture. Furthermore, other modes can be initiated. For example, one can choose only electrons, which passed without elastic scattering with objective lens aperture and get a so-called Bright-Field (BF) image (Figure 3.4b) or one of diffracted beams, which results in Dark-Field (DF) image, where only certain crystalline direction will be chosen and imaged (Figure 3.4c). The results on BF and SAED imaging of monolayers of MoS₂ will be discussed in Chapter 6.

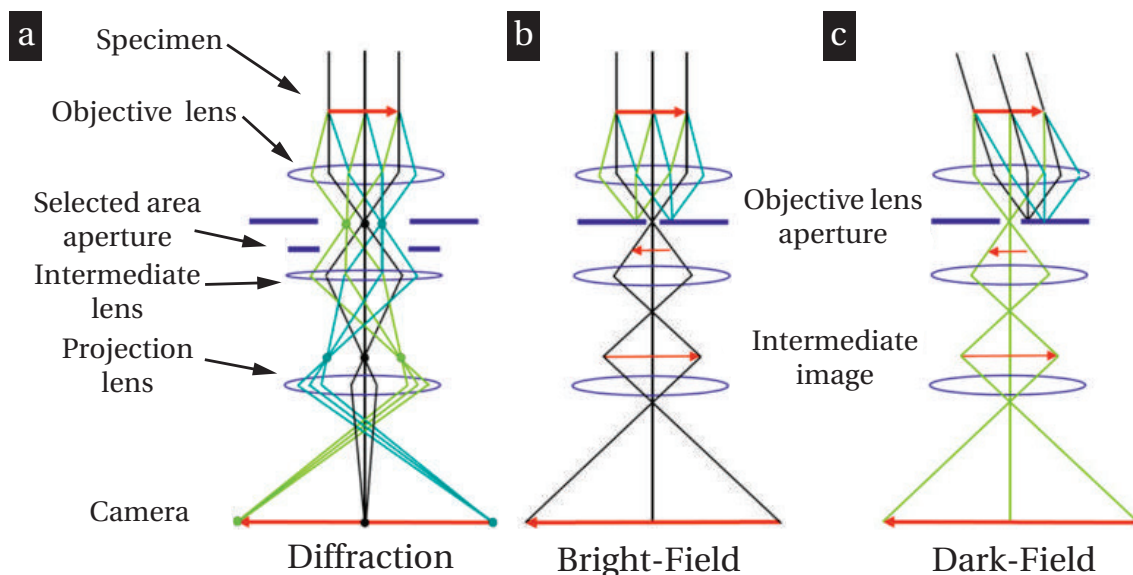


Figure 3.4 – Principle of operation of transmission electron microscope. (a) Diffraction imaging mode. (b) Bright-field imaging. (c) Dark-field imaging. Adapted from Ref. [89].

STEM mode in contrast to TEM mode uses a different approach. Here, a beam of electrons is focused on the specimen and scanned in a manner, typical for scanning

electron microscopes (SEM). For 2D materials, which are prone to beam damage and beam-induced etching, current are normally kept low, while state of the art instruments with spherical aberration correction use low beam energies (60-80 keV), with some reports indicating possibility to image even graphene samples at 30 keV [90].

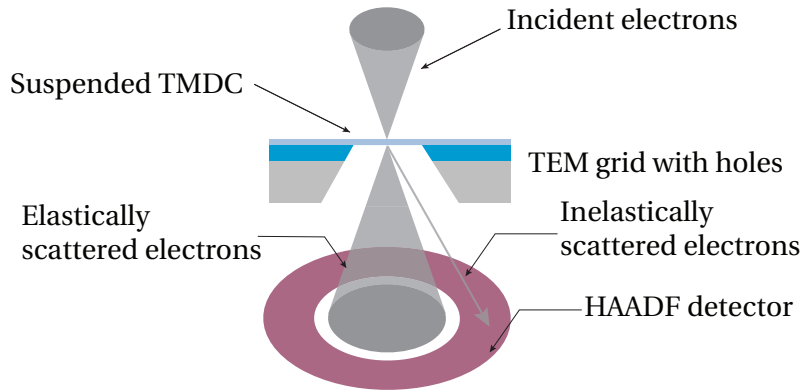


Figure 3.5 – Schematic of electron-sample interaction in HAADF-STEM.

In STEM mode, in contrast to TEM, one could collect inelastically scattered electrons, choosing the angle of collection. *Titan Themis* has different detectors, but in our work we mainly used high-angle annular dark-field imaging (HAADF) detector. The principle of operation is schematically illustrated on Figure 3.5. Incident electron beam can pass through or get elastically scattered on the lattice. However, HAADF detector collects electrons, which get inelastically scattered from the specimen (so-called Rutherford scattering), where the contrast obeys $Z^{1.7}$ relation [91]. This allows for example to distinguish Mo and S columns in 2H MoS₂ monolayer. We refer to Ref. [92] as a detailed overview of both TEM and STEM techniques.

3.4.2 Kelvin probe force microscopy

Kelvin probe force microscopy (KPFM) is the method, which allows to map work function of materials with high spatial resolution. It relies on operation of Atomic force microscope (AFM). In this thesis *Cypher AFM* (Asylum research) was used to perform both AFM and KPFM. We skip revision of AFM, as soon as it is a standard imaging technique for materials science, and concentrate on commenting the KPFM mode.

In KPFM one measures a contact potential difference (V_{CPD}) between a conducting tip inside AFM and a surface under investigation. It can be written in the following way [93]:

$$V_{CPD} = \frac{\phi_t - \phi_s}{-e} \quad (3.2)$$

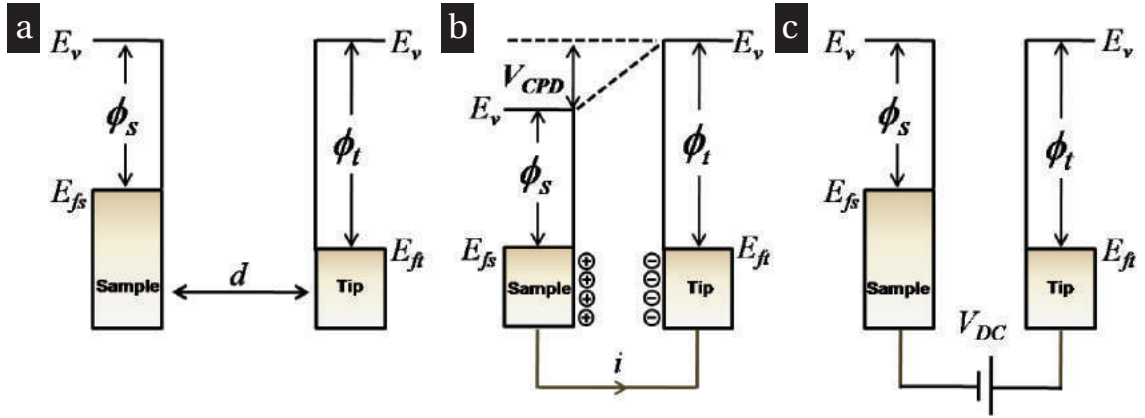


Figure 3.6 – Electronic energy levels of the sample and AFM tip for three cases. (a) Tip and sample are separated by distance d with no electrical contact. (b) Tip and sample are in electrical contact. (c) External bias V_{DC} is applied between tip and sample to nullify the CPD and, therefore, the tip–sample electrical force. E_v is the vacuum energy level. E_{f_s} and E_{f_t} are Fermi energy levels of the sample and tip, respectively. Reprinted from W. Melitz, J. Shen, A.C. Kummel, and S. Lee, "Kelvin probe force microscopy and its application", *Surface Science Reports*, vol. 66, no. 1, pp. 1-27, © (2011), with permission from Elsevier.

Where ϕ_t and ϕ_s correspond to workfunction levels of tip and sample respectively. On Figure 3.6 electronic levels of the sample and conductive AFM tip are discussed. Without electrical contact tip and sample, each having certain work function level, are isolated from each other (Figure 3.6a). When tip and sample are put into electrical contact due to work function mismatch the CPD is created. In KPFM one compensates V_{CPD} by applying external voltage V_{DC} to the tip. Typical KPFM maps represent the spatially resolved surface potential maps.

The measurements are performed in the following way. Alternating signal is applied to the tip V_{AC} , which creates electrostatic force, while V_{DC} is used to minimize this force. The electrostatic force can be written in the following way:

$$F_{es}(z) = -\frac{1}{2}\Delta V^2 \frac{dC(z)}{dz} \quad (3.3)$$

Where ΔV is the difference between V_{CPD} and voltage applied to the tip and $\frac{dC(z)}{dz}$ is the gradient of effective capacitance between the tip and the specimen. We further develop Equation 3.3 taking into account DC and AC components of voltages applied to the tip:

$$F_{es}(z) = -\frac{1}{2} \frac{dC(z)}{dz} [(V_{DC} \pm V_{CPD}) + V_{AC}\sin(\omega t)]^2 \quad (3.4)$$

Chapter 3. Experimental techniques

Equation 3.4 can be further divided on 3 parts:

$$F_{DC}(z) = -\frac{dC(z)}{dz} \left[\frac{1}{2} (V_{DC} \pm V_{CPD})^2 \right] \quad (3.5)$$

$$F_{\omega}(z) = -\frac{dC(z)}{dz} (V_{DC} \pm V_{CPD}) V_{AC} \sin(\omega t) \quad (3.6)$$

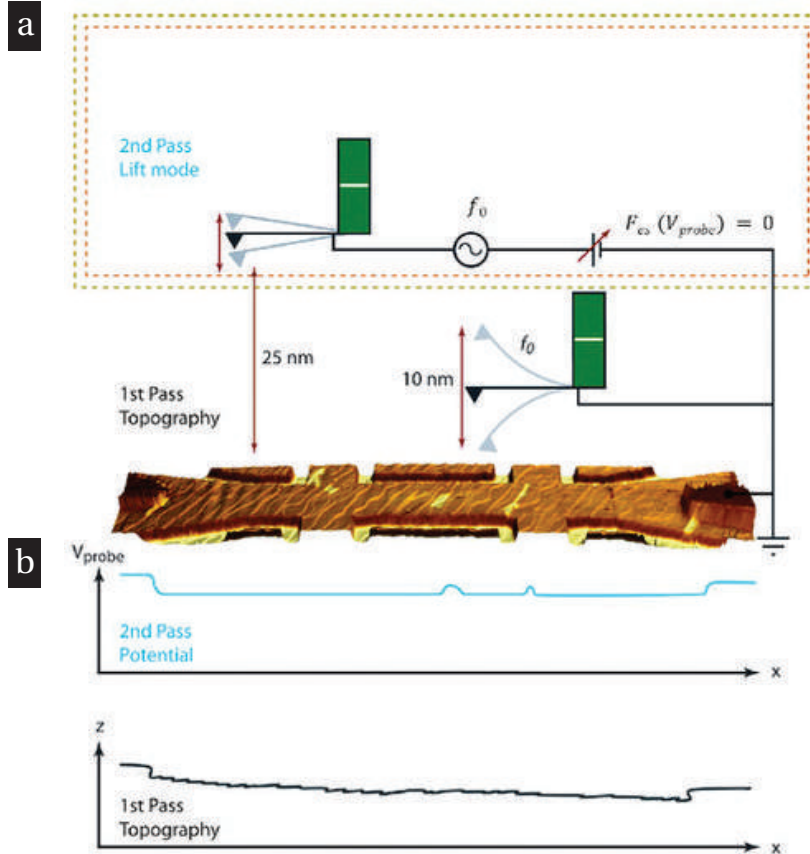


Figure 3.7 – Example of graphene work function imaging. (a) Topography of the graphene Hall bar is superimposed with surface potential maps on a 3D image. (b) Plots show characteristic profiles, i.e. surface potential on top and topography on bottom along the horizontal line in the center of the image (not shown). Adapted from V. Panchal, R. Pearce, R. Yakimova, A. Tzalenchuk, and O. Kazakova, "Standardization of surface potential measurements of graphene domains", *Scientific Reports*, vol. 3, p. 2597, © (2013), Rights Managed by Nature Publishing Group .

$$F_{2\omega}(z) = -\frac{dC(z)}{dz} \frac{1}{4} V_{AC}^2 [\cos(2\omega t) - 1] \quad (3.7)$$

Equation 3.6 is used to measure V_{CPD} . There are several types of KPFM modes. Similar to Ref. [94], in our measurements we performed two subsequent scans of the same line on the

3.4. Material characterization

surface. First run is the standard tapping mode to determine the topography of our sample, during the second run we lifted the tip and performed work function measurement of the surface, zeroing the potential difference V_{CPD} . This is so-called amplitude modulation (AM) mode of measurement. We refer to comprehensive review on the topic in Ref. [93] for further information.

4 Electrical Transport Properties of Single-Layer WS_2

4.1 Introduction

Monolayer MoS_2 was the first to attract significant attention of scientific community partially due to the fact that high quality single crystals of this material are abundant in nature. Other members of TMDCs materials family however appear to be also very promising both for electronics and optics. Monolayer WS_2 has identical crystal structure to MoS_2 and a direct bandgap of at least 2.0 eV [95]. Due to the presence of heavier tungsten atoms in this material spin-orbit coupling is more pronounced [96] than in MoS_2 case and thus valence band spin splitting reaches the value of 400 meV. This in principle should allow easier observation of the valley Hall effect [29, 97] in WS_2 than in MoS_2 . In this chapter we are going to discuss electrical transport properties of monolayer and bilayer WS_2 . This chapter is based on the article published in ACS Nano, 2014, 8 (8), pp 8174–8181, where Dmitry Ovchinnikov was the first author. There is significant overlap between this chapter and the above mentioned paper.

Our initial interest to this material was based on the lack of fundamental knowledge on electrical transport properties of monolayer WS_2 at the time. One of the early theoretical transport studies [98] indicated that among monolayers of TMDCs WS_2 has the lowest effective mass, which leads to improved ON current and mobility according to calculations. In fact recent experimental study [99] of "clean" samples encapsulated in h-BN partially support this hypothesis, where WS_2 samples have higher mobility than MoS_2 . Although mobility depends not only on effective mass, but also on defects [100, 101], dielectric environment [16, 102] and device fabrication procedure [16, 103], it was important to show devices in simple geometry similar to studied at that time monolayer MoS_2 samples [75, 102, 104, 105]. Monolayer MoS_2 lacks p-type conduction, while monolayer WS_2 was reported to have ambipolar carrier injection [85], which was possible using ionic liquid gating. Ambipolar curves for mono- and multilayer WS_2 samples with ionic liquid gating

Chapter 4. Electrical Transport Properties of Single-Layer WS₂

are shown on Figure 4.1. Ionic liquid gating, however, is known to provide low contact resistances even for such intrinsic materials as monolayer WSe₂ [58], [60] and thus performance of devices with solid gate can be remarkably different. For practical applications solid gated devices are preferred, where contact resistance has never been studied for monolayer WS₂. Efficient carrier injection with solid gate, as well as information on temperature dependent transport properties was missing. Although some reports found insulating behaviour of transport in mono- and multilayers of WS₂ [106], band-like transport was not demonstrated. On the other hand one would intuitively expect to have band-like transport and metallic state due to similarities with MoS₂ [75, 102, 104, 105].

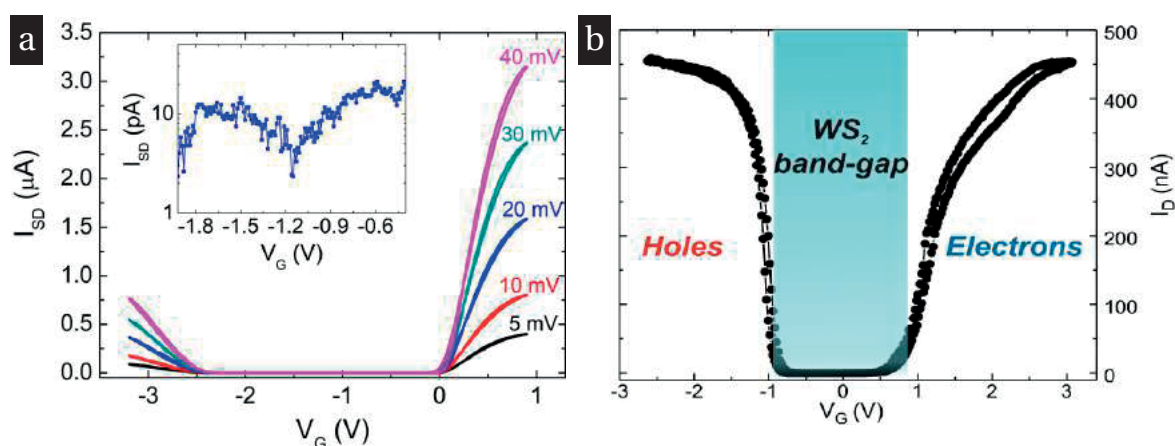


Figure 4.1 – Ionic liquid gating of WS₂. (a) Ambipolar transport in monolayer WS₂ for different V_{ds} . Adapted with permission from S. Jo, N. Ubrig, H. Berger, A.B. Kuzmenko, and A.F. Morpurgo, "Mono- and bilayer WS₂ light-emitting transistors", *Nano Letters*, vol. 14, no. 4, pp. 2019-2025, © (2014) American Chemical Society. (b) Ambipolar transport in multilayer WS₂ with quantitative determination of bandgap. Adapted with permission from D. Braga, I. Gutiérrez Lezama, H. Berger, and A.F. Morpurgo, "Quantitative Determination of the Band Gap of WS₂ with Ambipolar Ionic Liquid-Gated Transistors", *Nano Letters*, vol. 12, no. 10, pp 5218–5223, © (2012) American Chemical Society.

In this chapter we demonstrate simple devices - mono- and bilayer WS₂ FET, which are fabricated on SiO₂ substrates with global back gate underneath. Our devices show n-type behaviour and I_{on}/I_{off} current ratio in the order of 10^6 . These samples have channel exposed to atmosphere and we demonstrate, that by careful annealing we are able to modulate both doping level of the channel and contact resistance. We find that initially our samples are quiet resistive, but long annealing in vacuum can restore band-like transport and relatively low contact resistances. Field-effect mobilities at room temperature even in non-optimized geometry show values, comparable to state of the art monolayer MoS₂ transistors. Furthermore, we turn our attention to temperature-dependent measurements. We observe metal-insulator transition and explore both metallic and insulating states.

4.2 Results: Electrical Transport Properties of Single-Layer WS₂

Fabrication of our field-effect transistors starts with micromechanical cleavage of single-crystals of WS₂ on wafers with n++ Si with thermally grown SiO₂. Single-crystals of WS₂ were grown by chemical vapour transport (CVT) method with Br as a transport agent. Natural WS₂ crystals are normally heavily doped with Mo [106] and thus were not used in the present study. Contrast of resulting flakes was determined on substrates and correlated with the height, extracted by means of AFM imaging. Furthermore, we concentrated on mono- and bilayer flakes of WS₂. The typical AFM image of monolayer WS₂ sample is shown on Figure 4.2a, where the height of the studied flake in the order of 0.7 nm is extracted. Contacts were patterned *via* standard EBL, followed by electron beam evaporation of 90 nm of Au and lift off in acetone. Selected samples were patterned by next step of EBL and RIE plasma etching into Hall bar structures, one example is shown on Figure 4.2b. We have also studied different contact configurations, in particular Ti/Au and Ag/Au stacks. Our investigation of contact resistances and contact linearities revealed, that Au after *in situ* annealing in vacuum provides the lowest contact resistances and linear contact reading in four-probe geometry, as it is shown in Sections 4.2.3 and 4.2.4 .

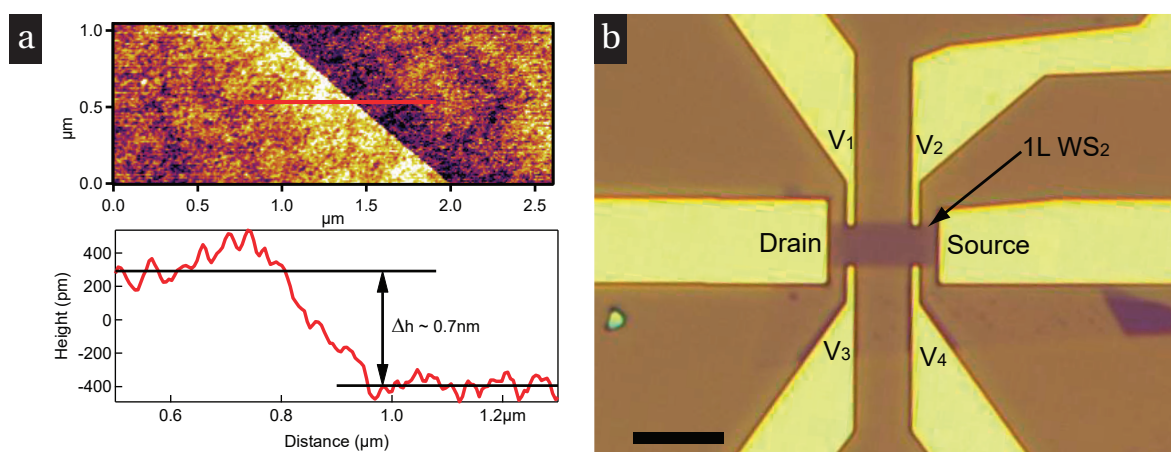


Figure 4.2 – Fabrication of monolayer WS₂ field-effect transistor. (a) AFM image of monolayer WS₂ flake, upper panel - AFM image, lower panel - slice along red line. (b) Optical image of the device patterned in a Hall bar geometry, scale bar - 5 μm. Adapted from Ref. [12], © (2014) American Chemical Society.

We measured both two-contact and four-contact resistance. It appears to be essential in case of WS₂, as soon as contact resistances are still higher than in case of MoS₂.

4.2.1 Device performance in air and in vacuum

We start characterization with doping behaviour of our samples. We characterize a typical bilayer WS₂ device in air, vacuum and after annealing in vacuum. Figure 4.3a summarizes device characteristic in above mentioned regimes of operation. In air the device shows weak p-type behaviour with channel current $I_{ds} = 1$ nA at gate voltage $V_g = -70$ V and bias voltage $V_{ds} = 1$ V. Pumping down the chamber provides access to both branches of conductance, as shown on Figure 4.3a. We measured the sample down to pressure $p = 2.7 \times 10^{-5}$ mbar before annealing. The decrease of pressure leads to consistent improvement of n-type conductivity. However, the effect of annealing for 40 hours at 115°C (blue curve on Figure 4.3a) is very pronounced, ON current increases by almost two orders of magnitude. On Figure 4.3b we plot V_{th} for both types of conduction as a function of chamber pressure and annealing. Further evidence of annealing effect is also visible in $I_{ds}-V_{ds}$ curves, as shown on Figure 4.3c, d at positive $V_g = 60$ V. Before annealing, although the device is sufficiently conductive, $I_{ds}-V_{ds}$ curve has hysteresis and is non-linear (Figure 4.3c). After annealing the hysteresis decreases, curve becomes symmetric, although with some non-linearities near $V_{ds} = 0$ V (Figure 4.3c). The performed annealing apparently impacts not only doping level of the device, but also interface between metal and semiconductor, which leads to improvement of contact resistance and more reproducible measurements. In section 4.2.2 we will show, that these non-linearities do not impact dramatically on measured values of four-probe conductivity and thus mobility.

The dependence of device performance on vacuum conditions and annealing is in agreement with previous reports on MoS₂ devices [75, 104, 105]. In these reports, a similar shift of threshold voltage V_{th} was observed and attributed to the presence of adsorbed H₂O and O₂ from the atmosphere and their removal *via in-situ* annealing while recent theoretical calculations predict [107] that the absorption of H₂, O₂, H₂O on the surface of MoS₂ can result in p-type doping. Our observations confirm that WS₂ devices also show a performance increase following annealing in vacuum. Their performance in atmospheric conditions is however markedly worse than in the case of MoS₂. The consistent n-type doping in our samples is most probably related to doping of synthetic crystals of chalcogenides by transport agents, for example by Br, as has been observed before for bulk crystals [108, 109].

4.2.2 Effect of in situ annealing on device characteristics at room temperature

As it is obvious from previous section, transport in WS₂ devices is extremely sensitive to environment. We now turn to single-layer devices and study the effect of *in situ* annealing

4.2. Results: Electrical Transport Properties of Single-Layer WS₂

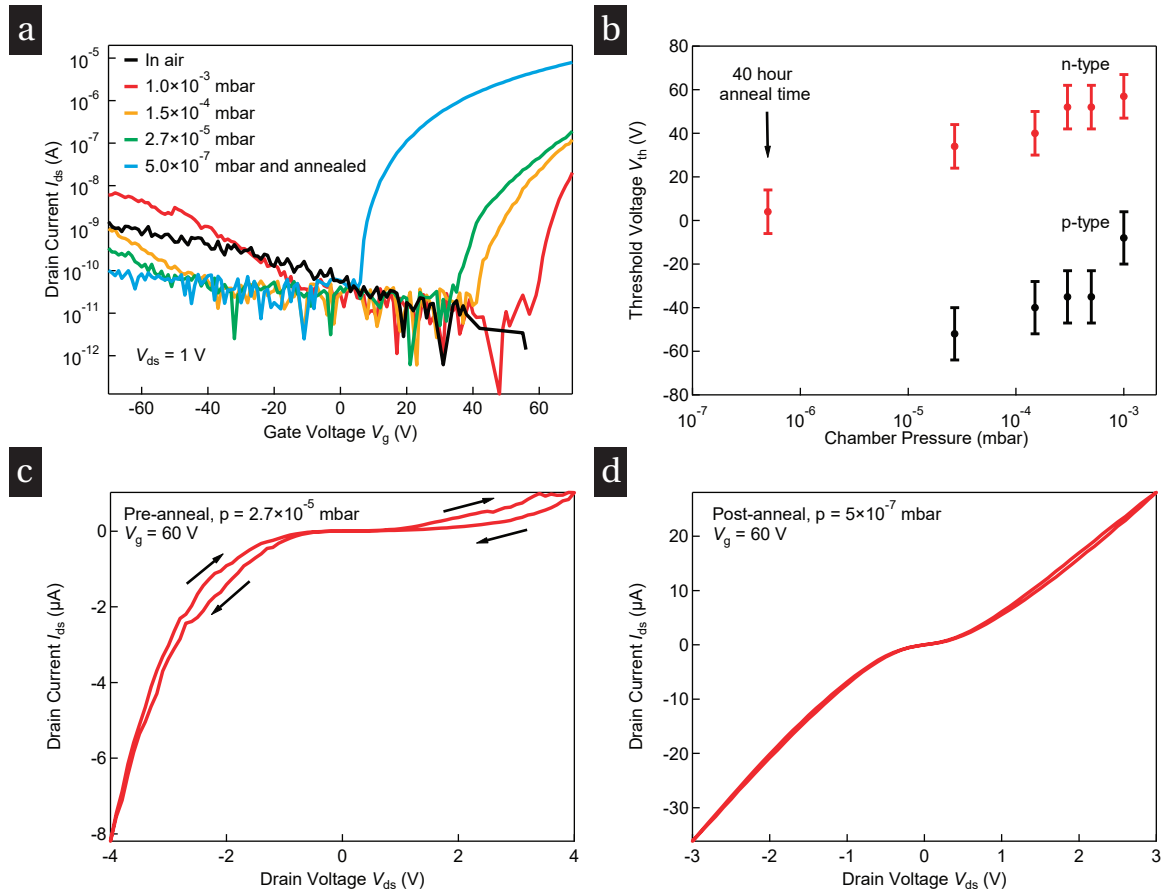


Figure 4.3 – Characterization of double-layer WS₂ transistor in vacuum and the effect of annealing. (a) Current as a function of gate voltage (I_{ds} - V_g) in air, vacuum and after annealing. (b) Threshold voltage V_{th} for p-type and n-type conduction as a function of pressure in the system. (c) The dependence of device current I_{ds} on the bias voltage V_{ds} (I_{ds} - V_{ds}) for a fixed value of gate voltage $V_g = 60$ V before annealing in the vacuum chamber. (d) Same as (c), after annealing for 40 hours at 115 °C. Adapted from Ref. [12], © (2014) American Chemical Society.

on device behaviour.

Figure 4.4 shows the room-temperature characterization of a single-layer WS₂ transistor in vacuum and the effect of annealing. As shown on Figure 4.3, placing the device in vacuum results in a shift of V_{th} towards negative values, revealing the pristine electronic state of the material, in the absence of strong doping by the adsorbates. Further annealing improves the ON-state current and provides further shift of V_{th} . We perform characterization of a chosen device with different annealing times up to 145 hours in vacuum. Figure 4.4a shows the I_{ds} - V_g curves for different annealing times while Figure 4.4b presents the dependence of the sheet conductivity G_{sh} on the back-gate voltage V_g for different annealing times. On Figure 4.4c we show the extracted two-terminal and four-terminal resistance for the fixed gate voltage for the same device. Interestingly, while the four-terminal resis-

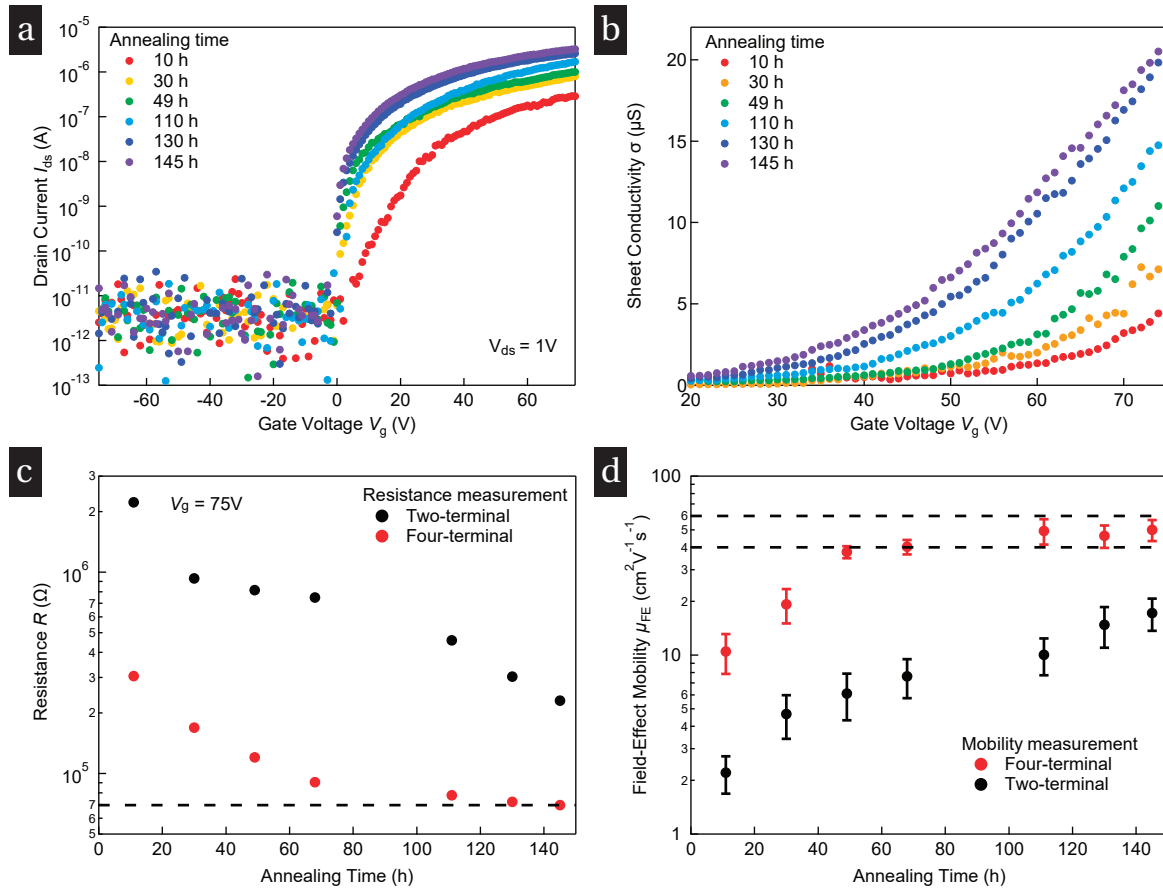


Figure 4.4 – Performance of the single-layer WS₂ transistor in vacuum. (a) Current-voltage I_{ds} - V_{bg} curves for the device recorded at different stages during the annealing process. (b) Sheet conductivity G_{sh} as a function of gate voltage V_g for the same annealing times as in (a). (c) Resistance as a function of annealing time at fixed gate voltage ($V_g = 75V$). Red markers - four-terminal measurements, black markers - two-terminal measurements. Four-terminal resistance reaches a plateau at 70 kOhm indicated by the dashed line after 60 hours of annealing, while the two-terminal resistance continues to decrease during the entire annealing procedure. (d) Field-effect mobility of single-layer WS₂ *vs.* the annealing time. Red markers - four-terminal mobility, black markers - two-terminal mobility. Dashed black lines are given as a guide for the range of extracted mobilities. Adapted from Ref. [12], © (2014) American Chemical Society.

tance reaches saturation after 60-80 hours of annealing, the two-terminal resistance keeps decreasing. From these measurements the four-terminal field effect mobility could be extracted. The following expression is used to calculate the mobility:

$$\mu_{FE} = \frac{\partial G_{sh}}{\partial V_g} \frac{1}{C_{ox}}. \quad (4.1)$$

Where $C_{ox} = 1.3 \times 10^{-8} F \cdot cm^{-2}$ is the geometric back-gate capacitance of 270 nm SiO₂ per

4.2. Results: Electrical Transport Properties of Single-Layer WS₂

unit area, G_{sh} is the sheet conductivity, which is extracted from four-probe measurements

$$G_{\text{sh}} = \frac{I_{\text{ds}}}{V_{\text{xx}}} \frac{L_{\text{xx}}}{W_{\text{ch}}}. \quad (4.2)$$

Where L_{xx} is the distance between the probes and W_{ch} is the channel width. In similar way two-terminal mobility can be extracted. This quantity does not take into account contact resistance, but provides qualitative information on device behaviour:

$$\mu_{2C} = \frac{\partial I_{\text{ds}}}{\partial V_{\text{bg}}} \frac{L_{\text{ch}}}{W_{\text{ch}} C_{\text{ox}} V_{\text{ch}}}. \quad (4.3)$$

Where L_{ch} is the channel length, W_{ch} channel width. We plot on Figure 4.4d two-terminal mobility and four-terminal mobility as a function of annealing time. Same as for resistance, four-terminal mobility saturates, while two-terminal mobility continues improving.

We also plot the extracted four-terminal field-effect mobility after 145 hours as a function of applied V_{g} . The values are extracted by numerically differentiating the conductivity, thus introducing noise in the data. We notice, that although it is possible in principle to extract mobility of charge carriers at any point of G_{sh} vs. V_{g} curve, field-effect mobility extraction requires linear relationship between conductivity and gate voltage. The saturation of mobility vs. V_{g} means, that the Fermi level has reached the conduction band. Furthermore, in Section 4.2.7 we will discuss signature of this transition from temperature dependent measurements. From Figure 4.5, we extract a value for the room-temperature mobility of $\mu_{\text{FE}} = 50 \pm 7 \text{ cm}^2 \cdot \text{V}^{-1} \cdot \text{s}^{-1}$, which is comparable with the ones measured for monolayer MoS₂ in similar configuration at room temperature [75, 104, 105].

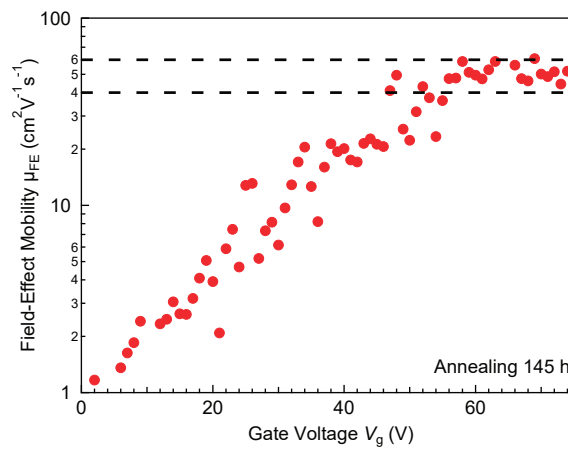


Figure 4.5 – Saturation of four-probe mobility after 145 hours of *in situ* annealing for monolayer WS₂ device. Adapted from Ref. [12], © (2014) American Chemical Society.

4.2.3 Accuracy of electrical measurements

To evaluate the accuracy of these measurements, we show on Figure 4.6 the drain current I_{ds} as a function of the voltage drop between the two voltage probes (V_1 and V_2). The dependence is linear in the entire range of applied bias voltage V_{ds} ($\pm 2V$) for the range of gate voltages V_g where we extract the field-effect mobility ($V_g \sim 60-80 V$). This confirms that the four-terminal conductivity measurements are reliable and they are not influenced by Schottky barriers that could be present at the voltage probes.

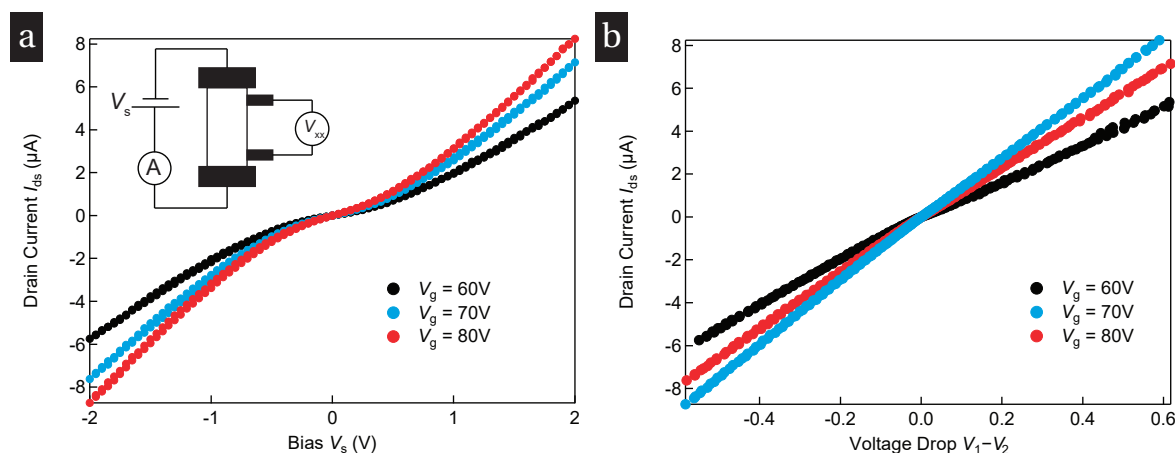


Figure 4.6 – Accuracy of four-terminal measurements at room temperature. (a) I_{ds} - V_{ds} and (b) Current I_{ds} vs. voltage drop V_{xx} between the voltage probes after 145 h of annealing in vacuum. The linear dependence implies the correct measurements of four-terminal mobility. Adapted from Ref. [12], © (2014) American Chemical Society.

4.2.4 Choice of metal contact for monolayer WS₂

We repeated the same annealing procedure for different types of metal contacts. The results are summarized on Figure 4.7. All samples are monolayer WS₂ devices after *in situ* annealing for 20-30 hours. On Figure 4.7a we plot V_{th} dependence on the contact metal used. Au and Ti/Au contacts provided V_{th} close to 0V, while Ag/Au stack gave positive V_{th} . Furthermore, we looked at contact resistances at fixed doping level ($V_g - V_{th} = 70V$). All metals showed quite resistive contacts, but Au provided the lowest contact resistances.

Further advantage of Au contacts appears to be related to symmetry of I_{ds} - V_{ds} curves. On Figure 4.8 the data on I_{ds} - V_{ds} curves for positive V_{bg} is presented after the standard *in situ* annealing procedure. It can be seen that contacts look highly non-linear, which implies asymmetric Schottky barrier formation and difficult to reproduce results for Ti/Au and Ag/Au metal stacks.

4.2. Results: Electrical Transport Properties of Single-Layer WS₂

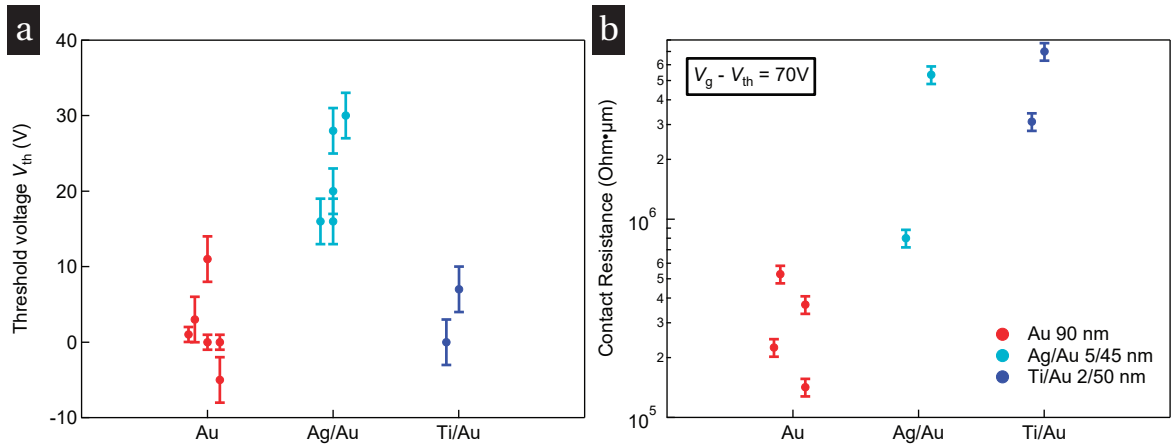


Figure 4.7 – (a) Threshold voltage V_{th} and (b) contact resistance of different metals for injection of carriers in conduction band of monolayer WS₂.

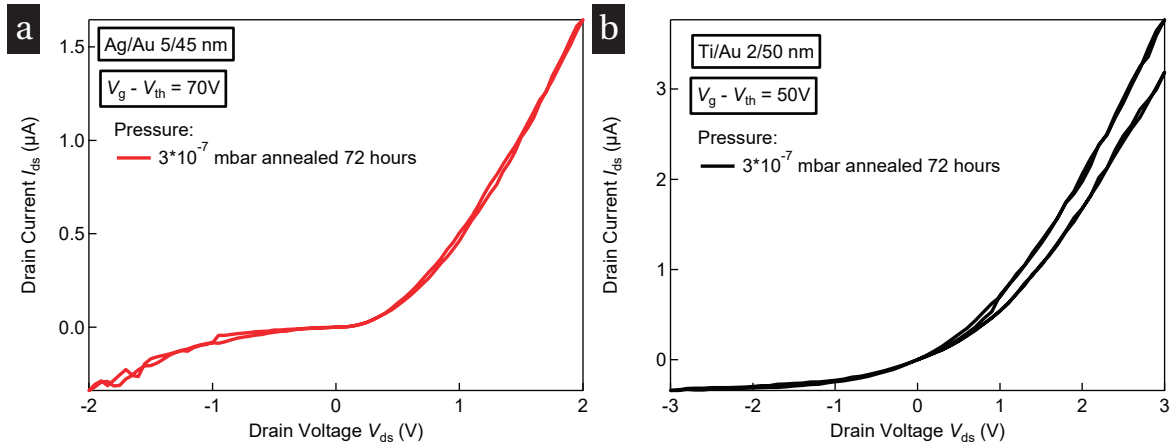


Figure 4.8 – Accuracy of four-terminal measurements at room temperature. (a) I_{ds} - V_{ds} and (b) Current I_{ds} vs. voltage drop V_{xx} between the voltage probes after 145 h of annealing in vacuum. The linear dependence implies the correct measurements of four-terminal mobility.

4.2.5 Performance of FET based on monolayer WS₂

Finally, we estimate the I_{on}/I_{off} ratio for the device with Au contacts after the final step of annealing (145 hours). The ratio $I_{on}/I_{off} \sim 10^6$, *estimated with an applied bias of $V_{ds} = 1$ V* (Figure 4.9), is larger than previously reported values in the case of multilayer WS₂ [110] because of the enhanced electrostatic control achieved in single-layers.

Strictly speaking, this is not the precise way of extraction, as soon as standard CMOS technology requires equal and small values of V_{ds} and V_g applied to determine this quantity. Our result is rather a proof of principle and large V_g are necessary due to non-optimized geometry with the use of a global back gate. For example, a smaller range of V_g with high-k

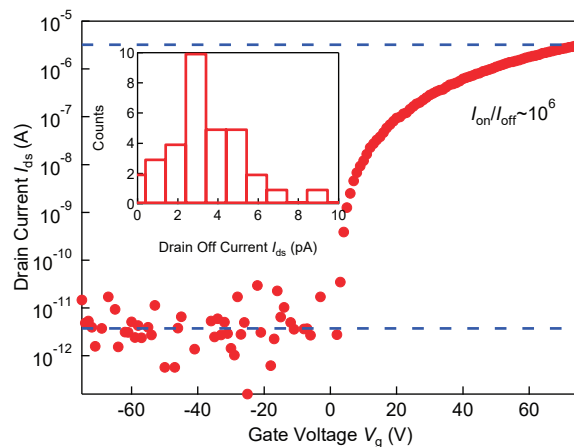


Figure 4.9 – Performance of monolayer WS₂ transistor. $I_{\text{on}}/I_{\text{off}} \sim 10^6$, estimated with an applied bias of $V_{\text{ds}} = 1$ V. Inset - histogram of I_{off} from which average value is estimated. Adapted from Ref. [12], © (2014) American Chemical Society.

dielectric is required for monolayer MoS₂ samples [5]. Further work on optimization of electrostatic control over the channel doping, device dimensions and contact resistances is needed to match production requirements and improve the device performance.

4.2.6 Temperature-dependent electrical transport

After the procedure of annealing and high quality of transport has been achieved, we turn to temperature-dependent transport measurements. The devices were annealed in cryogenic setup until the saturation of four-probe mobility could be reached. Typical monolayer device characteristic is plotted on Figure 4.10a. Here, we observe the transition point, associated with switching between conduction through localized states at the band edge, which have insulating nature to band-like transport, which is metallic. The change in energy with respect to the band edge is shown on Figure 4.10a, inset. Initially, the Fermi level E_{F} is located near the band edge in the localized states tail. Such a tail has been shown to exist by capacitance measurements in MoS₂ [111]. By applying positive gate voltage V_{g} localized states are populated and MIT occurs when the conduction band is reached. Electrons, residing in the band, provide band-like conduction. Right axis of Figure 4.10a presents the values of sheet conductivity in units of e^2/h , where e is the elementary charge and h the Planck constant. The crossover region between insulating and metallic states corresponds to a value of the sheet conductivity slightly lower than e^2/h . This is consistent with values reported in top-gated [102] as well as back-gated [105], [104] monolayer MoS₂ devices.

4.2. Results: Electrical Transport Properties of Single-Layer WS₂

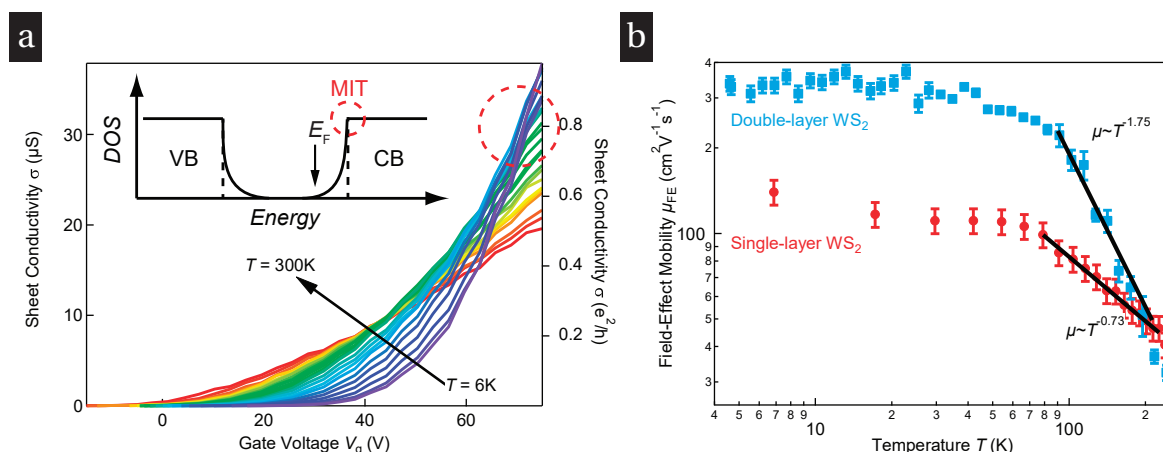


Figure 4.10 – (a) Metal-insulator transition in monolayer WS₂ transistor manifests itself with increase of conductivity with decrease of temperature at high positive V_g . (b) Mobility μ_{FE} as a function of temperature for mono- and bilayer WS₂. Adapted from Ref. [12], © (2014) American Chemical Society.

4.2.7 Metallic state

We studied transport properties in both regimes of conductance - metallic and insulating. We first investigate transport in the metallic state inside the conduction band of WS₂. We plot mobility μ_{FE} vs. temperature T for a mono- and bilayer WS₂ sample on Figure 4.10b for fixed carrier density. Mobility increases for the monolayer sample when the temperature is lowered from 220K to 83K, where it saturates at $120 - 140 \text{ cm}^2 \cdot \text{V}^{-1} \cdot \text{s}^{-1}$. Similarly, for the double-layer WS₂ flake it saturates above $300 \text{ cm}^2 \cdot \text{V}^{-1} \cdot \text{s}^{-1}$ at low temperature. In the region between 220K and 83K mobility follows the power law $\mu_{FE} \propto T^{-\gamma}$.

We compare mono- and bilayer WS₂ samples, studied in this work. It is important to notice, that from the theoretical point of view the combination of factors like phonon-scattering [112, 113], temperature dependent screening [114] and dielectric environment [115] impact the temperature dependence of mobility. First, temperature damping factors γ are different. In case of monolayer $\gamma = 0.73$ was extracted, which is close to encapsulated monolayer MoS₂ samples [102] and in agreement with one work on unencapsulated monolayer MoS₂ samples on SiO₂ samples [104] while in a different work damping factors above 1 are reported for both mono- and bilayer MoS₂ [105]. In case of bilayer WS₂ device, value of $\gamma = 1.75$ was extracted, which is close to the values reported for bulk dichalcogenide crystals [108]. Recent studies on "clean" samples encapsulated in h-BN, showed values around 2 for multilayers of WS₂ [99], which is also well correlated with similar measurements on h-BN/MoS₂/h-BN sandwiches [16]. Although, differences in the values of γ between mono-, bilayer or bulk TMDCs samples have been reported, several considerations should be taken into account. The temperature damping factor apparently depends on the dielectric environment [115]. Furthermore, the damping temperature

coefficient is a carrier-density dependent quantity, as has been shown by Radisavljevic and Kis [102] in case of monolayer MoS₂ samples encapsulated in a high- k dielectric. More detailed studies of doping-dependent damping factor in case of WS₂ are needed to unambiguously conclude on this point.

Second, saturation of mobility happens at the same temperature $T = 83\text{K}$, which indicates similar levels of disorder in both samples, since the low temperature mobility is impurity limited. It can be seen that for instance in the follow up work on h-BN encapsulated WS₂ samples [99], low temperature mobility saturates at lower values of temperatures around 10K. Third, the low temperature mobility for bilayer WS₂ sample is higher, than in monolayer case. This is consistent with other reports, for example on MoS₂ encapsulated in h-BN, where low temperature mobility appears to be systematically higher in multilayers [16]. Intuitively it could be understood, taking into account screening by the bulk of TMDCs, which implies that monolayers are more sensitive to any type of disorder, originating from the substrate or from the fabrication residues.

4.2.8 Insulating state in 1L WS₂

We move on to the discussion of transport on the band edge, where conductivity decreases with decreasing temperature. Transport in this regime was studied in the framework of thermally-activated and variable-range hopping (VRH) models. On Figure 4.11 such analysis is shown for monolayer case. At elevated temperatures, sheet conductivity G could be fitted to the Arrhenius formula:

$$G = G_0 e^{-E_a/k_B T} \quad (4.4)$$

Where G_0 is a constant, E_a is the activation energy, k_B the Boltzmann constant and T is the temperature. On the inset of Figure 4.11a we plot the dependence of G from $1/T$, from which E_a could be extracted. The activation energy is plotted on Figure 4.11a. This quantity represents the thermal activation of charge carriers at the Fermi energy (which is controlled by gate voltage V_g) into the conduction band. As it is shown on Figure 4.11a the activation energy decreases until the conduction band is reached near MIT. Furthermore, the dependence of E_a on the gate voltage provides us the density of states (DOS) $D(E)$ below the conduction band edge. It can be written using the expression:

$$\frac{dE_F}{dV_g} = \frac{C_{\text{ox}}}{C_{\text{ox}} + C_t} \quad (4.5)$$

Where C_{ox} is the back-gate capacitance and $C_t = e^2 D(E)$ the quantum capacitance, from which the DOS $D(E)$ could be extracted. The DOS extracted from Figure 4.11a

4.2. Results: Electrical Transport Properties of Single-Layer WS₂

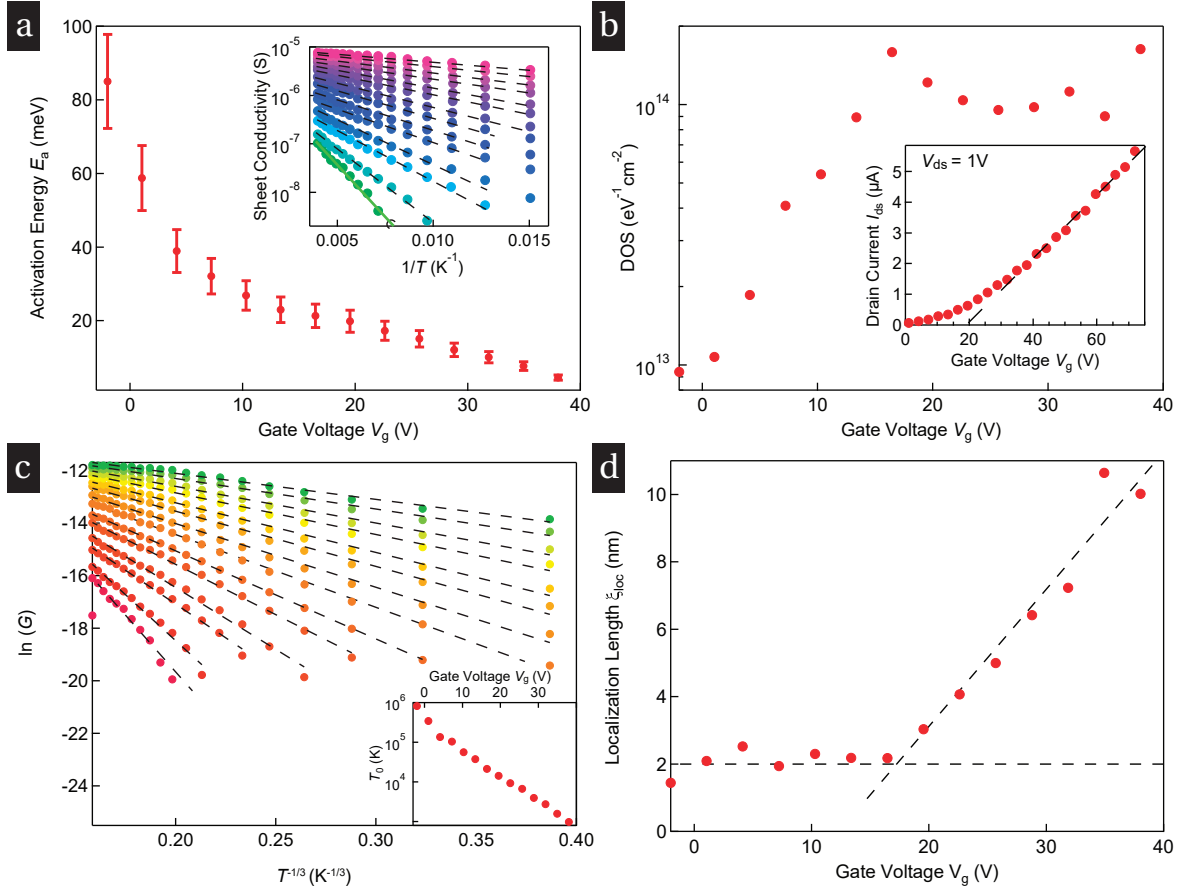


Figure 4.11 – Electrical transport in the insulating regime of single-layer WS₂. (a) Activation energy E_a as a function of gate voltage V_g extracted from the Arrhenius plots of the sheet conductivity (inset) in the high temperature range. (b) Density of states extracted from the activation energy. Inset: I_{ds} - V_g curve for the same device recorded at room temperature with linear extraction of V_{th} (dashed line). (c) Logarithm of sheet conductivity plotted as a function of $T^{-1/3}$ for different gate voltages. The variable range hopping parameter T_0 (shown in inset) can be extracted from the slopes of the line fits. (d) The dependence of localization length on the gate voltage V_g . Dashed lines are guides for the eye. Adapted from Ref. [12], © (2014) American Chemical Society.

is plotted on Figure 4.11b. We notice, that saturation of DOS happens at the value of $D_{2D}^{exp} \approx 2 \times 10^{14} eV^{-1} cm^{-2}$, which is close to theoretical value of DOS inside the conduction band of monolayer WS₂, which could be calculated using the formula:

$$D = g_s \times g_v \times m^* / \pi \hbar^2 \quad (4.6)$$

Where g_v is the valley degeneracy, g_s the spin degeneracy, m^* is electron effective mass, which is according to calculations for monolayer WS₂ is [98] $0.34m_0$. We find $D_{2D}^{theory} \approx 2.85 \times 10^{14} eV^{-1} cm^{-2}$ in a good agreement with our experimentally measured values. At

lower gate voltages, the DOS exhibits an exponential decrease [111] (dashed line in Figure 4.11b). Notice that the drop in the DOS corresponds to the room-temperature threshold voltage measured from the linear extrapolation of the output curve to zero, as shown in the inset of Figure 4.11b. The values of DOS ($10^{13} eV^{-1} cm^{-2}$) measured around $V_{bg} = 0V$ on the other hand are comparable with the ones obtained with the same model for monolayer MoS₂ [111], which is in general attributed to the density of trap states inside the gap.

The lower temperature regime ($T = 20K - 66K$) can be described with the variable range hopping (VRH) model. In this model [116, 117] conductivity $G \sim e^{-(T_0/T)^{-1/3}}$ for the two-dimensional case, if one assumes constant density of states at Fermi level. From the variable range hopping model, the localization length could be extracted [118], following the expression:

$$\xi = \sqrt{\frac{13.8}{k_B D(E) T_0}} \quad (4.7)$$

Where $D(E)$ is the density of states. We plot the fits to the VRH model on Figure 4.11c, while inset of Figure 4.11c shows the dependence of the parameter T_0 on the gate voltage. Using the values of $D(E)$ extracted from the high-temperature regime (Figure 4.11b), together with the values of T_0 extracted from the VRH model (Figure 4.11c) one can obtain the values of localization length ξ dependence on the gate voltage V_{bg} . This dependence is shown on Figure 4.11d. Interestingly, the localization length stays constant inside the bandgap and starts to increase linearly, when the sample enters the conduction band edge. This delocalization process can be intuitively understood as filling of localized trap states and increase of freedom of charge carrier, until it enters the band-like transport.

4.3 Conclusion & Outlook

In this chapter we have discussed back-gated FET based on monolayers of WS₂. Our approach was to make the simplest possible devices, to carefully characterize them and to compare the WS₂ properties with similar MoS₂ characteristics. Our results indeed show, that it is possible to have high-performance devices based on WS₂.

Follow-up work showed, that it is possible to further optimize WS₂ devices. For example, in work [119] high- k substrates instead of standard SiO₂ ones were implemented, which allowed observation of improved room temperature ($83 \text{ cm}^2 \cdot \text{V}^{-1} \cdot \text{s}^{-1}$) and low temperature ($337 \text{ cm}^2 \cdot \text{V}^{-1} \cdot \text{s}^{-1}$) mobility. As soon as electrostatic control over the channel carrier density was improved, the subthreshold swing (SS) values were also remarkably low (440 mV/dec), which is still far from room temperature limit demonstrated for MoS₂ monolayers [5]. The

sensitivity of doping in monolayer WS_2 to the gas environment can be resolved using other dielectrics as encapsulation layers, for example h-BN. In Ref. [120] authors used CVD-grown h-BN to encapsulate monolayer WS_2 . The achieved samples showed further improvement in mobility (in the order of $200 \text{ cm}^2 \cdot \text{V}^{-1} \cdot \text{s}^{-1}$ at room temperature and $500 \text{ cm}^2 \cdot \text{V}^{-1} \cdot \text{s}^{-1}$ at 5K). Progress in polymer-free dry transfer techniques used recently for TMDCs allowed to observe quantum oscillations in multilayers of WS_2 [99] and mobilities around $20\,000 \text{ cm}^2 \cdot \text{V}^{-1} \cdot \text{s}^{-1}$ at low temperature. Similar quality samples based on monolayers of WS_2 have not been achieved so far.

5 Disorder engineering and conductivity dome in ReS_2 with electrolyte gating

5.1 Introduction

In this chapter we are going to discuss fabrication and characterization of electrical double layer transistors (EDLTs) based on mono- and multilayer ReS_2 . EDLT is a type of transistor where polymer electrolytes or ionic liquids are used as the gating medium [40, 43, 83, 87, 121, 122]. They appear to be useful when one aims to reach high carrier densities or electric fields [49]. A number of important findings in the field of 2D semiconductors is related to the use of EDLT, in particular the discovery of superconductivity in multilayers [40, 41, 42] and monolayers [43] of semiconducting TMDCs at high carrier densities. We are going to demonstrate that ReS_2 is an unusual semiconducting system for polymer electrolyte gating. In particular we find strong modulation of conductivity in monolayer ReS_2 and correlate it with disorder strength, originating from the electrolyte. In fact, we use electrolyte-induced disorder as a tool of variation of electrostatic disorder. We believe, that our work is of general importance for the field of 2D materials, since depending on the device design and fabrication methods the amount of disorder in a particular sample can vary a lot. Furthermore, we show an example of an EDLT based on monolayer MoS_2 , where disorder leads to a decrease of mobility at high carrier densities, although this effect is weaker than in ReS_2 . The work discussed in the following section was reported in Nature Communications 7, Article number: 12391 (2016). Dmitry Ovchinnikov was the first author of the above mentioned paper. The reader will find significant overlap between the above mentioned article and the following section. However, some parts, for instance technical details on band structure and transport calculations will be not covered, the interested reader can refer to corresponding sections of Ref. [13]. It is important to point towards contributions of other co-authors, in particular Dr. Fernando Gargiulo from Prof. Oleg Yazyev laboratory at EPFL, who constructed the transport model, which explained the experimental findings.

5.2 Electrostatic disorder

In this section we will first discuss graphene and TMDC samples and the effect of electrostatic disorder as one of the major extrinsic sources of scattering and decrease of mobility for layered materials. Furthermore, we will introduce EDLT as a device where disorder can be manipulated, which allows us to explore device behavior in different regimes.

5.2.1 Disorder in graphene devices

Graphene was the first material in the family of two-dimensional materials to attract serious research efforts [1, 2, 3]. From the first sight, graphene and other two-dimensional materials look very similar to conventional two-dimensional electron gas (2DEG), which could be found for instance in high-mobility electron transistor (HEMT) structures [123]. We stress several important differences. First, 2DEG is completely buried between the semiconducting layers which form it, making it a clean electronic system, screened from any types of external disorder. 2D materials, fabricated on standard SiO₂ substrates are immediately exposed to potential variations and roughness of the substrate [124]. Second, depending on the sample design, the semiconducting channel can be exposed to atmospheric adsorbates (for example in back gate geometry) and atmospheric species can act as scattering centers. Third factor, degrading sample quality, which is important for almost all devices in the field, are the processing residues, for instance polymer resist residues, which appear to be very difficult to remove [125]. We point to the fact, that all abovementioned effects appear to be more detrimental in the case of monolayers, where charge carriers in fact reside very close to the surface of the material and where screening from disorder is barely possible.

The historical development of the graphene research field, starting from the first samples, where quantum hall effect (QHE) was observed [126, 127] to recent detailed transport studies on various types of "clean" samples [14, 15] showed gradual improvement of sample quality. Placing graphene on low density h-BN instead of SiO₂ substrates already improved the quality of investigated samples [128, 129]. The importance of extrinsic sources of disorder was fully revealed, when first residue-free encapsulation of graphene in two-dimensional defect-free dielectric h-BN was demonstrated [14]. Certain techniques of transfer have been developed, which allowed to fully avoid contact between graphene and any polymer and to protect it from atmospheric adsorbates [14, 130]. The example of graphene, encapsulated in conventional way in h-BN [131], is shown on Figure 5.2.1a, where formed hydrocarbon bubbles are shown. Figure 5.2.1b shows high-resolution ADF-STEM micrograph of "clean" graphene sample [14], with no visible residues and perfect interfaces. Figure 5.2.1c, d show the basic transport characterization [14]. In contrast

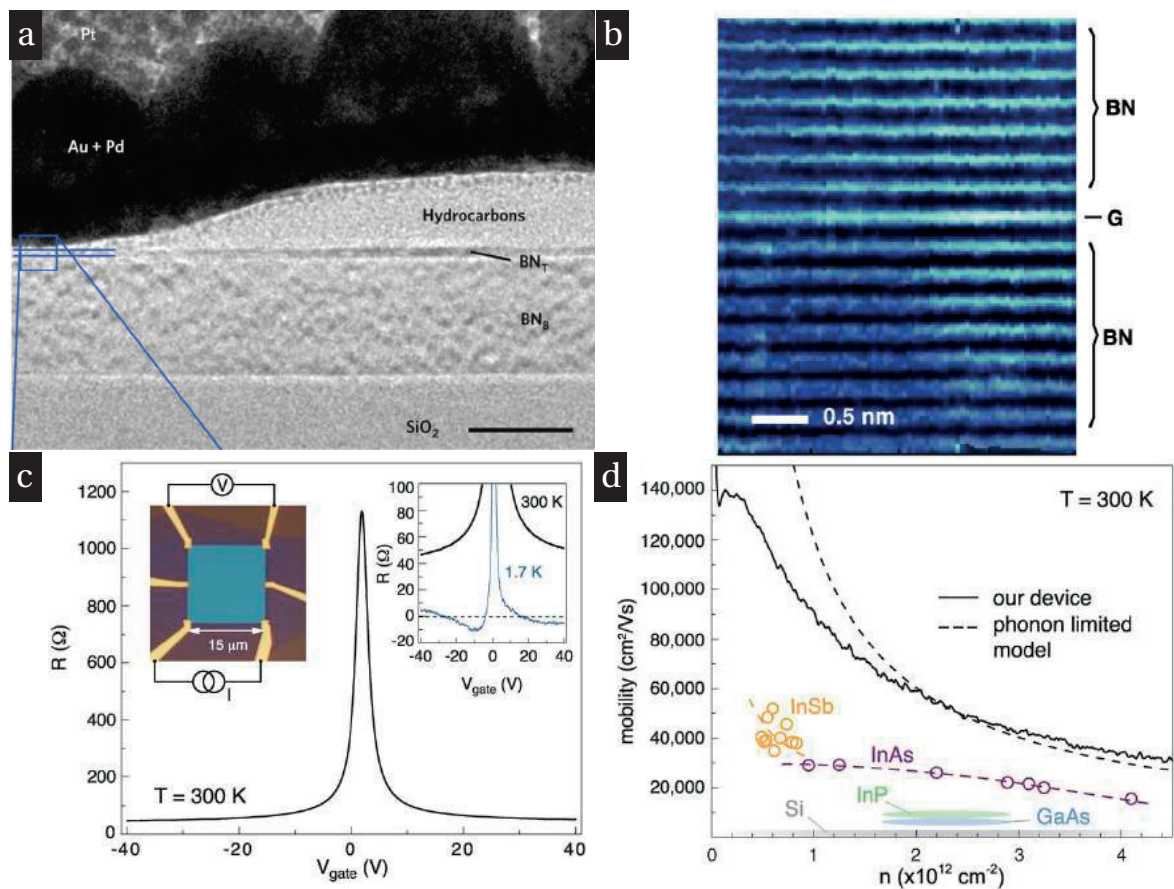


Figure 5.1 – Comparison between graphene samples, produced with different transfer methods. (a) Bright-field TEM micrograph of h-BN/Graphene/h-BN sample, with typical hydrocarbon bubbles, formed at the interface. Scale bar - 25 nm. Adapted by permission from Macmillan Publishers Ltd: [Nature Materials] S.J. Haigh, A. Gholinia, R. Jalil, S. Romani, L. Britnell, D.C. Elias, K.S. Novoselov, L. A. Ponomarenko, A.K. Geim, and R. Gorbachev, "Cross-sectional imaging of individual layers and buried interfaces of graphene-based heterostructures and superlattices", *Nature Materials*, vol. 11, no. 9, pp. 764-767, © (2012). (b) High-resolution cross-section ADF-STEM image of h-BN/G/h-BN device, produced with residue-free transfer method. (c) Electrical characterization of the "clean" h-BN/G/h-BN stack. Left inset - optical micrograph of the sample under investigation in van der Pauw geometry. Right inset - zoom in to R - V_{gate} characteristic at 300K and at 1.7K. Curve at 1.7K shows negative resistance on hole side, indicating ballistic transport on the scale of approximately 15 μm . (d) Comparison of room temperature mobility in graphene and other two-dimensional systems as a function of carrier density. (b)-(d) Adapted with permission from L. Wang, I. Meric, P.Y. Huang, Q. Gao, Y. Gao, H. Tran, T. Taniguchi, K. Watanabe, L.M. Campos, D.A. Muller, J. Guo, P. Kim, J. Hone, K.L. Shepard, C.R. Dean, "One-Dimensional Electrical Contact to a Two-Dimensional Material", *Science*, vol. 342, no. 6158, pp. 614-617, © (2013) The American Association for the Advancement of Science.

to conventional samples on SiO_2 and even not optimized samples on h-BN, the "clean" procedure allows ballistic transport on the scales of 10-20 μm .

5.2.2 Disorder in TMDCs

This approach could be universally employed for other two-dimensional materials, in particular to semiconducting TMDCs. TMDCs differ from graphene in many aspects, including the ranges of mobilities and defect types, but the possibility to remove most of the extrinsic sources of disorder allows us to significantly improve the sample quality [16]. We can quantify the sample quality based on the values of low temperature mobility.

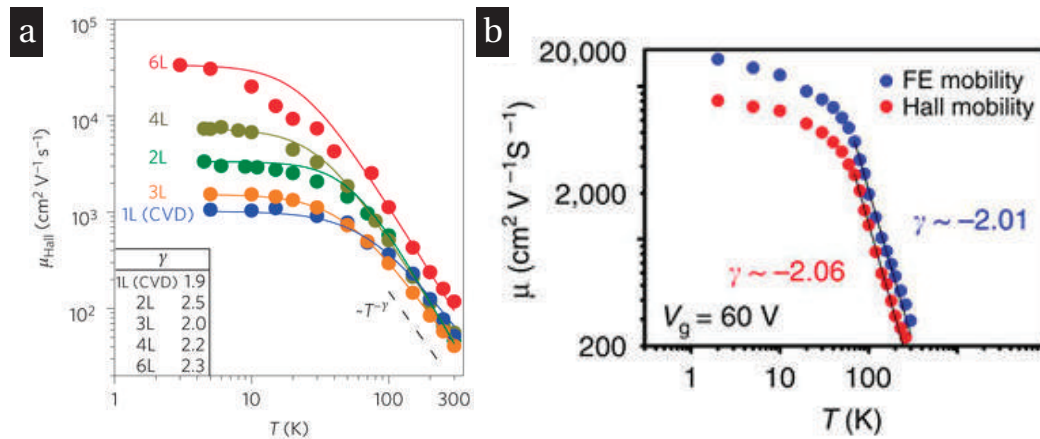


Figure 5.2 – Electrical transport properties of semiconducting TMDCs encapsulated in h-BN. (a) Mobility in h-BN encapsulated MoS₂ samples as a function of temperature and thickness. Adapted by permission from Macmillan Publishers Ltd: [Nature Nanotechnology] X. Cui, G.-H. Lee, Y. D. Kim, G. Arefe, P.Y. Huang, C.-H. Lee, D.A. Chenet, X. Zhang, L. Wang, F. Ye, F. Pizzocchero, B. S. Jessen, K. Watanabe, T. Taniguchi, D.A. Muller, T. Low, P. Kim, and J. Hone, "Multi-terminal transport measurements of MoS₂ using a van der Waals heterostructure device platform", *Nature Nanotechnology*, vol. 10, no. 6, pp. 534-540, © (2015). (b) Mobility in h-BN encapsulated multilayer WS₂ samples as a function of temperature. © (2016), Z. Wu, S. Xu, H. Lu, A. Khamoshi, G.-B. Liu, T. Han, Y. Wu, J. Lin, G. Long, Y. He, Y. Cai, Y. Yao, F. Zhang, and N. Wang, "Even-odd layer-dependent magnetotransport of high-mobility Q-valley electrons in transition metal disulfides", *Nature Communications*, vol. 7, p. 12955, 2016.

The point we would like to emphasize is that so far even in the cleanest samples low temperature transport in monolayers seems to be more sensitive to intrinsic or extrinsic values of disorder. For example, work [16] focuses on encapsulation in h-BN of MoS₂ samples of different thickness, as shown on Figure 5.2.2a. It appears, that monolayers have lowest mobility. Transport in h-BN encapsulated monolayer WSe₂ has been shown to have similar quality with low temperature mobility in the order of $2000 \text{ cm}^2 \cdot \text{V}^{-1} \cdot \text{s}^{-1}$, while multilayers exhibit higher low temperature carrier mobility [132] on the order of $4000 \text{ cm}^2 \cdot \text{V}^{-1} \cdot \text{s}^{-1}$.

We stress that h-BN encapsulation, although being a widespread approach for improvement of transport properties, is not the only one available. The strong side of h-BN use is

the possibility to pick up other 2D materials with this dielectric and avoid any contact with polymer and process flow residues [14]. However, any substrate without dangling bonds, for instance parylene [133], could lead to significant improvement of transport properties and less scattering.

In this Section we showed the importance of different types of extrinsic sources of disorder. We put optimization of material itself and intrinsic scatterers aside for now [101]. It is clear that understanding of disorder and its influence on transport properties is essential for optimization of high-performance devices based on TMDCs and other 2D materials for future applications.

5.2.3 EDLT as a disorder modulating tool

Discussion in the previous sections focused on the samples of different quality and comparison between them. We emphasize, that in each particular approach to sample fabrication technique disorder will be different but will have a fixed value. EDLT samples are known to have lower carrier mobility than "clean" ones. This is the initial sign of electrostatic disorder effect, originating from ionic liquids or polymer electrolytes. This can be seen on examples of such systems as monolayer WSe_2 , where low temperature mobility in EDLT [58] is an order of magnitude lower than in encapsulated samples [103]. Similar tendency is observed for example in black phosphorous samples [134], [135], [136],[137].

The origin of disorder could be qualitatively understood from Figure 5.3, where the cross section of interface between the semiconductor and the ionic media is schematically illustrated. Here, ions of different signs are located at different distances from the semiconducting channel and the in-plane distance between the ions varies as well. This random pattern can be understood if we consider the situation where two types of ions, which can be approximated as spheres, having imbalance in the amount of positive and negative ones, have to be tightly packed on the surface of our material. This rough electrostatic potential appears to be in the close vicinity of the semiconducting channel (typically 10-20 Å) and acts as extrinsic disorder for the carriers, travelling inside the semiconducting channel.

The only limitation for disorder modulation appears to be the fact that disorder strength is changed together with carrier density. Additional solid back gate leads to more flexible situation, where these two quantities could be modulated in an independent manner, changing electrolyte voltage at high temperatures and back gate voltage after freezing of electrolyte, thus exploring different carrier densities at the fixed value of disorder strength. We also notice that monolayers might be more sensitive to the abovementioned effect of disorder. The reason for that is the screening of the electric field in the bulk [49]. As for example shown on Figure 5.4b, in WSe_2 the electric field decays fast in the bulk. Thus

Chapter 5. Disorder engineering and conductivity dome in ReS₂ with electrolyte gating

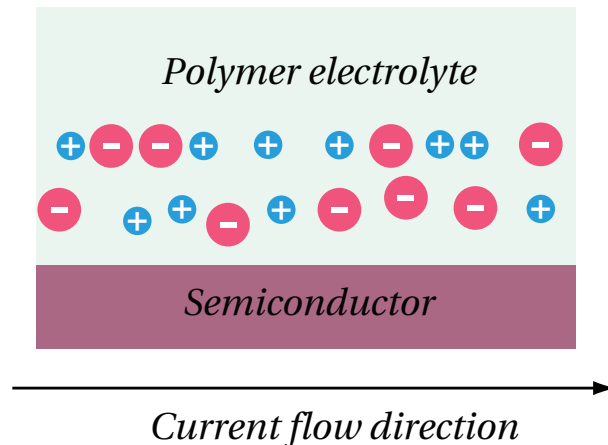


Figure 5.3 – Schematic cross section of interface between electrolyte and semiconducting channel in EDLT.

accumulation is happening in the top 2-3 layers (screening for WSe₂ is in the order of 2-3 nm). In case there is residual doping in the bulk, it will still provide conductivity (Figure 5.4a, sample is still conducting at the region around $V_g = -2V$), while the electrons in the deep layers will be screened from disorder by the upper ones.

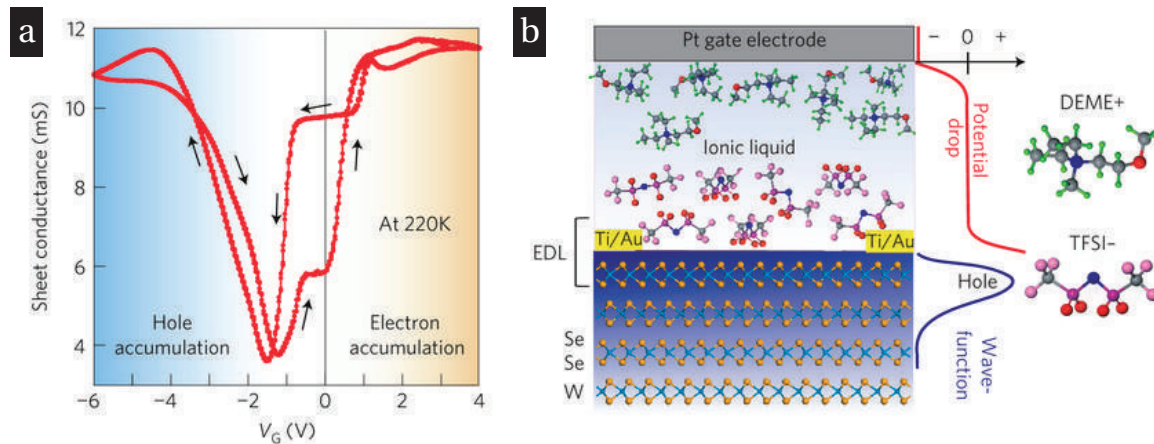


Figure 5.4 – EDLT based on bulk WSe₂. (a) Sheet conductivity as a function of gate voltage. (b) Schematic cross section of the interface between ionic liquid and WSe₂. Adapted by permission from Macmillan Publishers Ltd: [Nature Physics] H. Yuan, M.S. Bahramy, K. Morimoto, S. Wu, K. Nomura, B.-J. Yang, H. Shimotani, R. Suzuki, M. Toh, C. Kloc, X. Xu, R. Arita, N. Nagaosa, and Y. Iwasa, "Zeeman-type spin splitting controlled by an electric field", *Nature Physics*, vol. 9, no. 9, pp. 563-569, © (2013).

Experimentally, the effect of disorder has been observed in the number of works. In the Sections 5.2.1 and 5.2.2 we mentioned, that h-BN encapsulated samples in general have higher mobility due to clean interface, low roughness and good charge homogeneity of the substrates than for instance EDLT based on similar materials. However, we notice, that there are differences in sample fabrication procedures and thus the comparison between

the h-BN samples and EDLT might not be fair enough.

Important work in this aspect focuses on comparison of EDLT based on SrTiO₃ (STO) with different levels of disorder [87]. The experiment has been performed on pure STO samples and on the samples, capped with thin flakes of h-BN (0.5-1.5 nm thick), the schematic of used configuration is shown on Figure 5.5a. h-BN is used as a layer, which screens electrostatic disorder but still allows to achieve high capacitance of ionic liquid. The main result of this work is shown on Figure 5.5b, where low temperature mobilities of different samples are compared. The sample, protected with 0.5 nm thick (presumably monolayer) h-BN showed 10-fold improvement of mobility in comparison with the samples, which have not been protected.

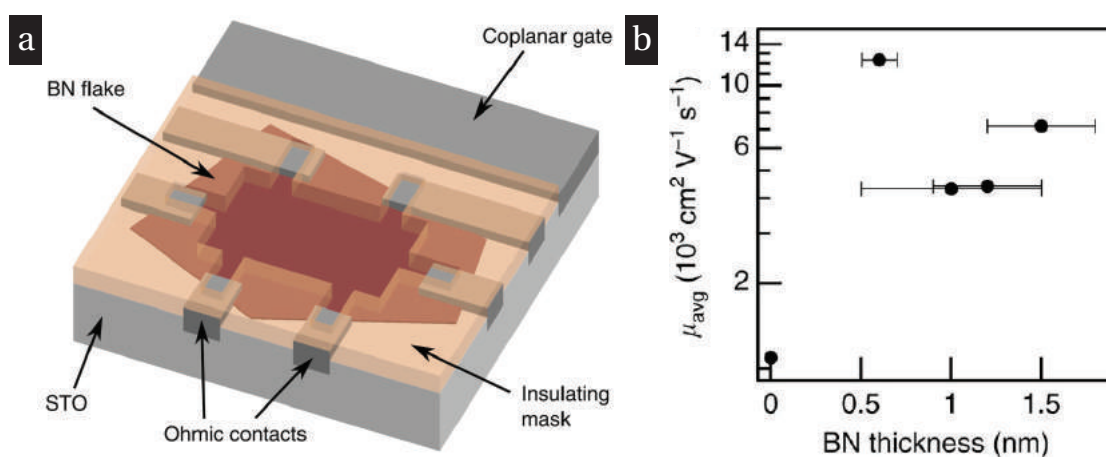


Figure 5.5 – EDLT based on STO and the effect of electrostatic disorder. (a) Schematic illustration of device configuration used. (b) Low temperature mobility as a function of h-BN layer thickness, protecting the channel. Zero thickness corresponds to absence of h-BN capping layer. © (2015) P. Gallagher, M. Lee, T.A. Petach, S.W. Stanwyck, J.R. Williams, K. Watanabe, T. Taniguchi, and D. Goldhaber-Gordon, "A high-mobility electronic system at an electrolyte-gated oxide surface", *Nature Communications*, vol. 6, 2015.

All abovementioned results and considerations point towards the importance of electrostatic disorder for device behavior of ultrathin sheets of 2D materials. Simple example of that is charge inhomogeneity, which leads to pronounced band-tail in MoS₂ samples [111] fabricated in a standard manner. Furthermore in this chapter we aim to create the system based on semiconducting ReS₂, where disorder and carrier density can be modulated semi-independently using two gates.

5.3 Structural and electrical characterization of ReS₂

Single crystals of ReS₂ were grown using the chemical-vapor transport (CVT) method, using Br₂ or ICl₃ as a transport agent in the laboratory of Prof. Ching-Hwa Ho in National

Chapter 5. Disorder engineering and conductivity dome in ReS₂ with electrolyte gating

Taiwan University of Science and Technology by Dr. Dumitru Dumcenco and Prof. Ching-Hwa Ho. Prior to crystal growth, quartz tubes containing the elements (Re, 99.95% pure; S, 99.999%) with Br₂ or ICl₃ were evacuated and sealed. The quartz tube was placed in two zones of a three-zone furnace and the charge pretreated for 24 h at 800°C with the growth zone at 1000°C, preventing the transport of the product. The furnace was then equilibrated to give a constant temperature across the reaction tube, and was programmed over 24 h to give the temperature gradient at which single-crystal growth took place. Best results were obtained with temperature gradients of approximately $\Delta T = 150^\circ\text{C} = 1160^\circ\text{C} - 1010^\circ\text{C}$. ReS₂ formed silver-colored, graphite-like, thin hexagonal platelets up to 2 cm² in area and 100 μm in thickness. Additionally, we used commercially available crystals from HQ Graphene (<http://www.hqgraphene.com/>). We did not find significant differences in doping levels or device characteristics between the two sources.

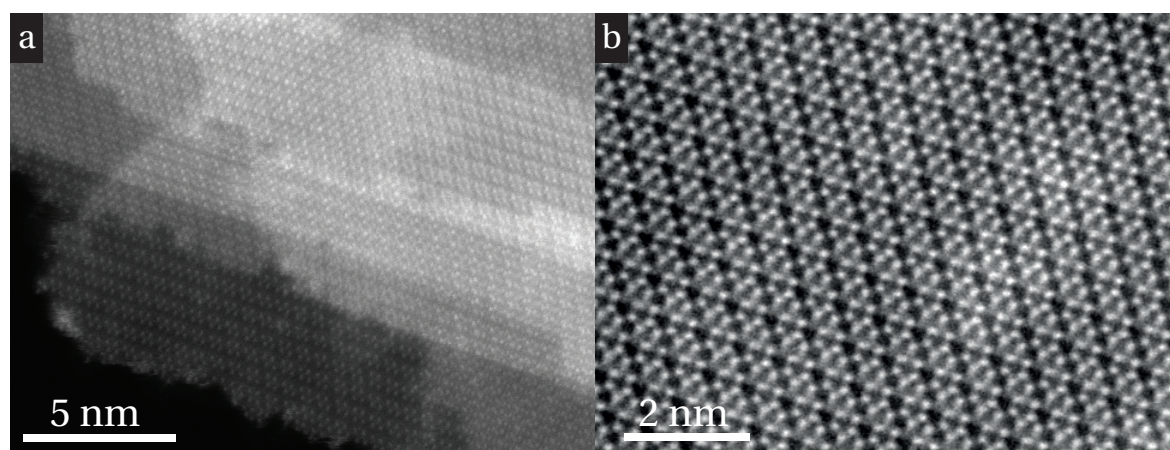


Figure 5.6 – STEM micrograph of multilayer ReS₂. (a) Edge of ReS₂ crystal. (b) Multilayer region of ReS₂ crystal. Adapted from Ref. [13].

Prior to fabrication of EDLT based on ReS₂, we performed structural measurements with Scanning Transmission Electron Microscopy (STEM) and fabricated standard field-effect transistors (FET) on Si/SiO₂ substrates. TEM samples were prepared on SiN grids with holes, wet transfer was employed using Poly(L-lactic acid) (PLLA) polymer [138]. Aberration-corrected scanning transmission electron microscopy (STEM) was performed using a *Titan Themis* 60-300 (FEI) operated with a beam energy of 80 keV. Medium angle annular dark field (MAADF) imaging conditions were applied with a probe convergence semi-angle of 28 mrad and a STEM detector collection semi-angle of ~ 40 -200 mrad. The probe current was kept below 50 pA. We used the sequence of images, acquired with low doses to avoid flake damage, and furthermore aligned and averaged them, using Digital Micrograph or ImageJ. Typical multilayer structure is shown on Figure 5.6. Anisotropy of the crystal, as well as extracted **lattice constants** match well with reports from other groups [26, 139].

5.3. Structural and electrical characterization of ReS₂

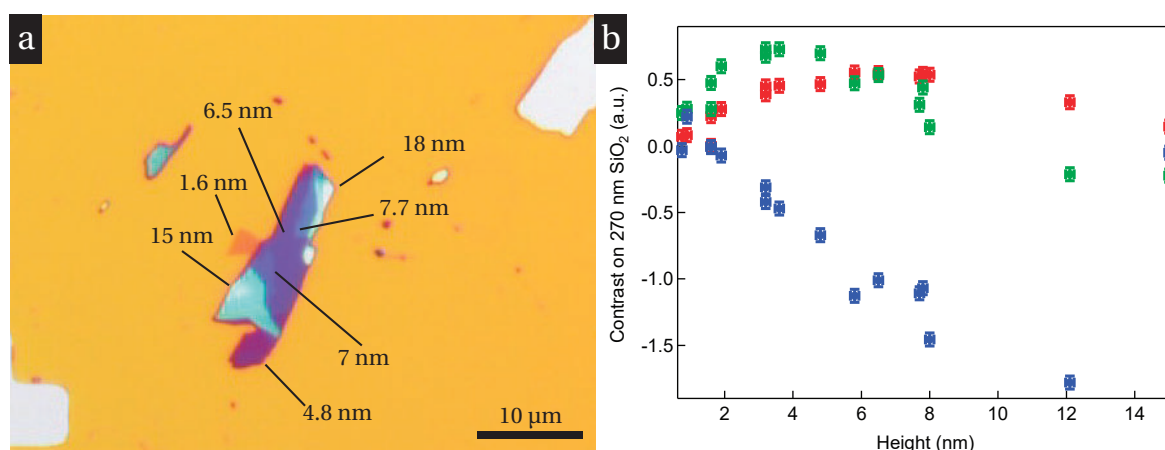


Figure 5.7 – Thickness calibration for ultrathin ReS₂ flakes. (a) Optical micrograph of a typical ReS₂ flake with height variation, thickness is determined by means of AFM imaging. (b) Contrast as a function of flake thickness.

Furthermore, we performed thickness calibration as a function of contrast on 270 nm thick thermally grown SiO₂ substrates. We performed AFM measurements on multiple flakes and plot contrast of each channel as a function of thickness on Figure 5.7b. From this calibration data we can extract thickness in similar way as it has been done for graphene [140] and MoS₂ [141].

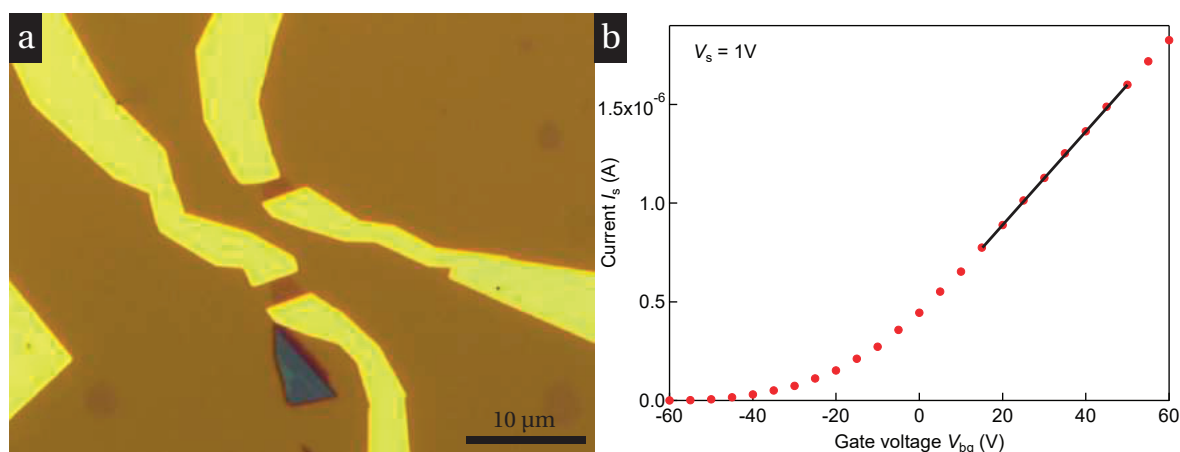


Figure 5.8 – Monolayer ReS₂ FET performance in vacuum. (a) Optical micrograph of the devices under investigation. (b) Current I_{ds} as a function of back gate voltage V_g after 24 hour of annealing in vacuum at 140°C.

From monolayer flakes, exfoliated on SiO₂ substrate we fabricated two-probe devices and characterize them in vacuum using a solid back gate after 24 hour annealing at 140°C. Results are plotted on Figure 5.8b and demonstrate slight n-doping of ReS₂ crystals we have, which is consistent with other reports available in literature [139, 142, 143]. From these measurements two contact field-effect mobility $\mu_{FE} \sim 2 \text{ cm}^2 \cdot \text{V}^{-1} \cdot \text{s}^{-1}$ could be extracted.

Chapter 5. Disorder engineering and conductivity dome in ReS₂ with electrolyte gating

Overall, we found consistent structural and electrical quality of our material with the results of other groups [144].

5.4 Results: disorder engineering and conductivity dome in ReS₂ with electrolyte gating

5.4.1 Monolayer ReS₂ EDLT characterization

After basic structural and electrical characterization of thin ReS₂ we move on to characterization of ReS₂ EDLT. We first focus on monolayer ReS₂ EDLTs. Device schematic is shown on Figure 5.9a, where we employ spin coated ion gel, in this case [EMIM]⁺[TFSI]⁻ in PS-PMMA-PS matrix as gate dielectric[88, 145]. In a different set of devices we used LiClO₄ in PEO polymer matrix [58, 86]. Results were similar and will be discussed later in the text. We also incorporate a solid back gate in our devices, as shown on Figure 5.9a, thus carrier densities and disorder could be modulated independently. We used two-probe and four-probe devices in this study to eliminate the contact resistance effect. Optical image of a typical device is shown on Figure 5.9b.

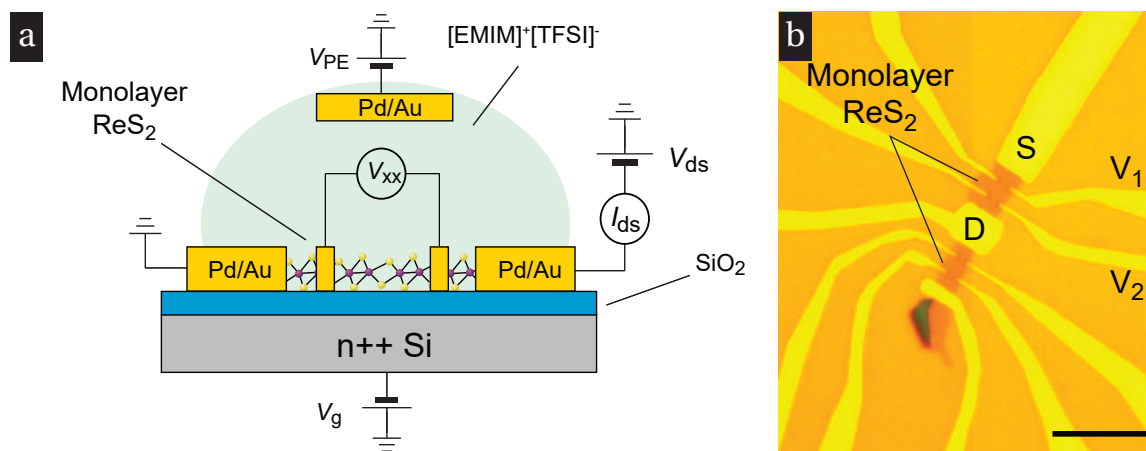


Figure 5.9 – EDLT based on ReS₂. (a) Schematic cross section of the ReS₂ EDLT. (b) Optical micrograph of monolayer ReS₂ sample in the four-contact geometry. Scale bar is 10 μm long. Adapted from Ref. [13].

We start the characterization of our devices with two-contact measurements at room temperature. [EMIM]⁺[TFSI]⁻ in our case has a freezing point around 220-240K. On Figure 5.10a we plot current I_s as a function of polymer electrolyte voltage V_{PE} . Since polymer electrolytes and ionic liquids are slow in comparison with solid dielectrics, we use relatively low sweep speed of V_{PE} ($0.3 \text{ mV} \cdot \text{s}^{-1}$) to let the ions migrate and stabilize. At $V_{PE} = 0\text{V}$ we already observe some current, which increases with the application of positive V_{PE} . However, after reaching a maximum, the current exhibits a sharp decrease and goes below

5.4. Results: disorder engineering and conductivity dome in ReS₂ with electrolyte gating

the resolution of instrument in our setup, effectively pushing the device into the OFF state. Furthermore, when V_{PE} is swept in the opposite direction, current recovers and returns to the initial value (arrows 1-9).

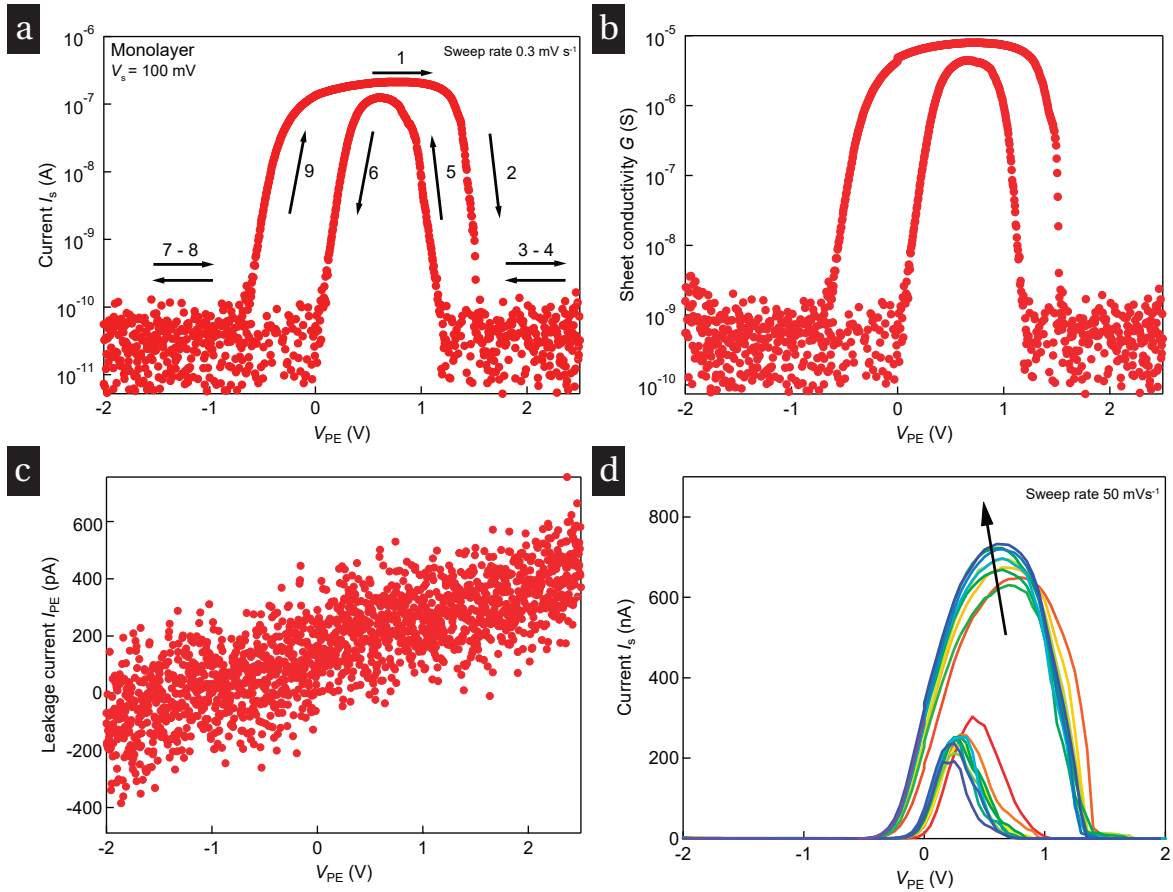


Figure 5.10 – Room temperature monolayer ReS₂ EDLT characterization. (a) Current I_S as a function of polymer electrolyte voltage V_{PE} . (b) Leakage current I_{PE} as a function of V_{PE} for the same measurement. (c) Sheet conductivity G as a function of V_{PE} . (d) Cycling of electrolyte for 10 times in monolayer ReS₂ EDLT, colors from red to blue correspond to cycles from 1 to 10. Adapted from Ref. [13].

Since the observed feature could be explained by unusual increase of contact resistance we performed four-probe measurements on the same sample. Four-probe measurements reveal that sheet conductivity G_{sh} reproduces this behaviour, thus ruling out the possibility of a contact resistance effect, as shown on Figure 5.10b. Care has been taken to monitor device degradation in terms of leakage currents and reproducibility. The leakage current from the same measurement is plotted on Figure 5.10c. Gradual increase with V_{PE} and low values (below 1nA) indicate that no degradation occurred. To observe the evolution of our devices in time and to further confirm the absence of degradation, we swept the electrolyte voltage 10 times with increasing sweep rates, which in principle could more probably lead to degradation. The result is plotted on 5.10d. Again, no significant differences

Chapter 5. Disorder engineering and conductivity dome in ReS₂ with electrolyte gating

were observed, which indicates the absence of apparent measurement artefacts. We also notice that no obvious degradation was observed in device behaviour within months of measurements.

The lattice distortion in ReS₂ leads to anisotropic transport: the material is more conductive along the direction of the Re atomic chains (see STEM micrograph on Figure 5.6). High doping levels could result in lattice distortion and modify electrical conductivity in different directions. To examine this, we looked at the conductivity anisotropy, using "directional" devices with eight electrical contacts rotated by 45° (Figure 5.11a, inset). In this particular device one pair of electrical contacts (1-5) appeared to be almost perfectly aligned with the "easy" axis. These experiments revealed that the ratio between conductivities in the range of carrier densities that allows us to reliably perform such measurements stays within the same sinusoidal dependence and corresponds well to both early results on bulk ReS₂ [146] and recent monolayer [139] measurements. Additionally, we found good agreement between experimentally measured anisotropy and theoretically calculated effective masses, which will be discussed later in the text.

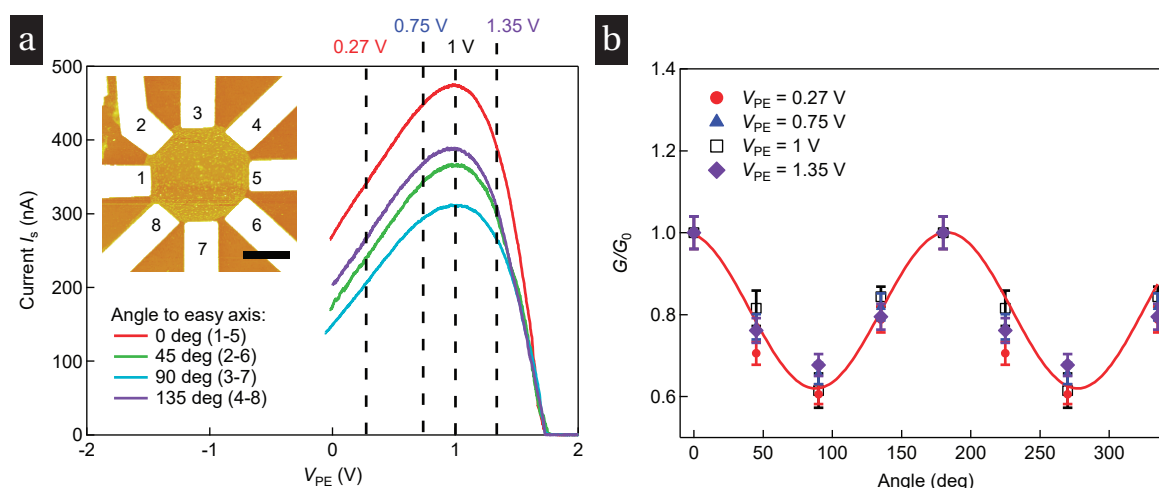


Figure 5.11 – Anisotropy measurements for monolayer ReS₂ at room temperature. (a) Current I_s measured for different pairs of contacts as a function of V_{PE} . Inset - AFM image of the device under investigation, scale bar - 1 μ m. (b) Reduced conductivity G/G_0 at different doping levels, red line: sinusoidal fit. Adapted from Ref. [13].

Most of the work on ReS₂ EDLTs was performed using [EMIM]-[TFSI] in PS-PMMA-PS matrix as the gating media (please, refer to Section 3.3.3 for details of PE preparation). However, exactly the same type of sharp turn-off at high V_{PE} could be observed with a different electrolyte. Experiments using LiClO₄-based polymer electrolyte prepared with two different solvents and concentrations of ions gave essentially the same result, as shown on Figure 5.12. The distinct behaviour of the conductivity with suppression at high carrier densities was observed in all monolayer ReS₂ devices studied (six monolayer ReS₂ EDLTs).

5.4. Results: disorder engineering and conductivity dome in ReS₂ with electrolyte gating

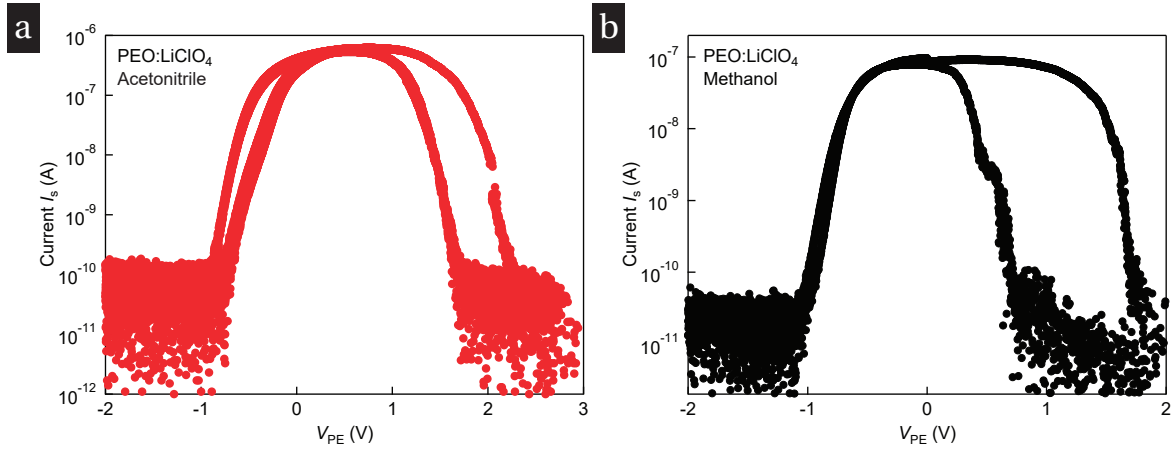


Figure 5.12 – Monolayer ReS₂ EDLTs based on LiClO₄ electrolyte, prepared in (a) acetonitrile, (b) methanol. Adapted from Ref. [13].

5.4.2 Temperature dependent transport in monolayer ReS₂

To reveal the possible influence of polymer electrolyte on the conductivity, we perform consecutive measurements on the same device before and after deposition of the electrolyte, as a function of temperature. In addition to the polymer electrolyte, we use a back-gate stack containing a high- k dielectric to modulate the charge density in our Hall bar devices (optical micrograph of discussed device is shown on Figure 5.9b). The back-gate voltage V_{bg} dependence of the sheet conductivity G extracted from four-probe measurements for different temperatures is shown on Figure 5.13a. On the left panel, the sheet conductivity G prior to the electrolyte deposition is shown. In subsequent panels, G as a function of V_{bg} is recorded after freezing the electrolyte at a given V_{PE} . Without the electrolyte, we observe a metal-insulator transition around $V_{bg} = 5.6V$ and field-effect mobilities of $\mu_{FE} \approx 3 \text{ cm}^2 \cdot \text{V}^{-1} \cdot \text{s}^{-1}$, consistent with other studies of ReS₂ and our previous measurements on SiO₂, which were discussed in Section 5.3. As soon as the electrolyte is deposited and $V_{PE} = 0V$ is applied (second panel), the overall conductivity decreases and the sample displays a purely insulating behavior.

Increasing the V_{PE} further results in a gradual decrease of conductivity (Figure 5.13a, from left to right). To quantify the changes in the insulating behavior, we tracked the conductivity dome as a distinct feature in our experiments. We fit our data in this insulating state with the thermally-activated transport model (see Equation 4.4). For all values of V_{PE} we could achieve a good fit in the range between 70 K and 150 K (Figure 5.13b). Figure 5.13c shows E_a as a function of V_{PE} . We can see that increasing the electrolyte voltage results in a significant increase of the activation energy (Figure 5.13c). This is in contrast to band-like transport and metallic state emerging at high carrier densities in the case of solid-gated devices before electrolyte deposition. The same behavior was observed in

Chapter 5. Disorder engineering and conductivity dome in ReS₂ with electrolyte gating

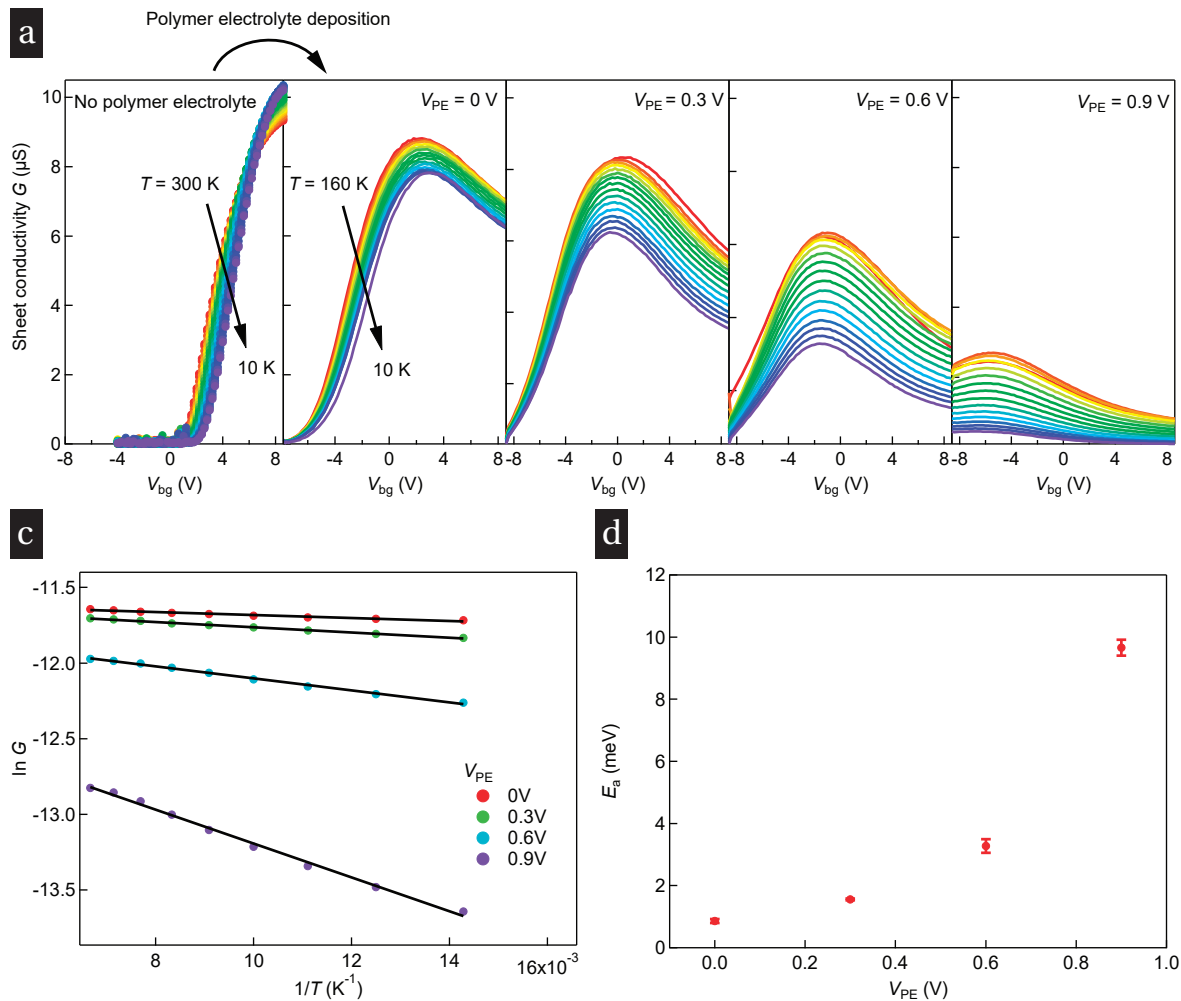


Figure 5.13 – Monolayer ReS₂ with and without the polymer electrolyte. (a) Sheet conductivity G as a function of back-gate voltage V_{bg} prior to PE deposition (left panel) and after PE deposition with different V_{PE} applied. (b) Arrhenius plots for E_a extracted on top of conductivity dome. (c) Activation energy E_a , extracted from the top of the conductivity dome as a function of V_{PE} . Adapted from Ref. [13].

devices fabricated on thicker SiO₂ substrates.

5.4.3 Comparison with multilayers of ReS₂

Furthermore, we analyse the thickness dependence of the observed behavior. We have fabricated samples from flakes of various thickness and performed similar measurements in the EDLT configuration. The results obtained at room temperature are plotted in Figure 5.14a with the sweep from $V_{PE} = 2.5\text{ V}$ to -0.5 V plotted for clarity. There is a clear difference between monolayer devices and thicker ones. First, monolayers are the only ones exhibiting the sharp turn off at high V_{PE} , while multilayers remain largely conductive even

5.4. Results: disorder engineering and conductivity dome in ReS₂ with electrolyte gating

at $V_{PE} = 2.5V$, although showing similar dome-like behavior. Second, the maximum sheet conductivity obtained in multilayers is systematically 4-8 times higher than in monolayers. Among multilayers (thicker than 2 layers) devices are identical despite some small variations of hysteresis and doping.

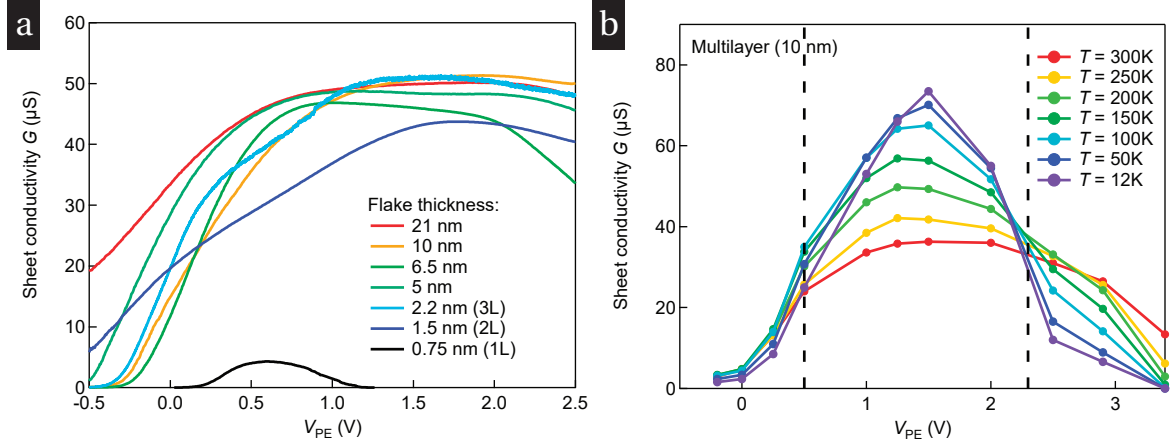


Figure 5.14 – Multilayer ReS₂ EDLT. (a) Sheet conductivity G as a function of V_{PE} for the flakes of different thickness. (b) Sheet conductivity G as a function of V_{PE} for 10 nm thick flake for different temperatures. Black lines correspond to the areas, where insulator to metal and metal to insulator transitions are occurring. Adapted from Ref. [13].

We proceed with temperature-dependent measurements on multilayer ReS₂. We performed multiple cooling cycles at different values of V_{PE} , as shown on Figure 5.14b for a typical 10 nm thick flake. Moving away from the conduction band edge, where the sample shows weakly insulating behavior, transport becomes metallic as a function of temperature, which means that conductivity increases with decreasing temperature. This insulator to metal transition is typical for layered materials [12, 102, 104, 105] and has been previously observed in case of multilayer ReS₂ [147]. Furthermore, conductivity reaches the maximum and starts to increase. More important, the crossover from metallic to insulating state is happening with increasing V_{PE} .

We first analyse the influence of disorder on conductivity in the metallic state. Since our samples have an integrated back gate, disorder strength, which is controlled by V_{PE} and doping, which is controlled by both V_{PE} and V_{bg} could be modulated in semi-independent manner. We employ Hall effect (HE) measurements to extract carrier density and mobility in an independent manner.

Prior to Hall effect (HE) measurements we point to the anisotropy of ReS₂ as a potential source of artefacts in the HE data. As soon as the material is anisotropic, there will be a built-in Hall voltage, associated with the fact that charged carriers prefer movement in the direction with less resistance [148]. Cross-like structures allow us to directly check this and eliminate the possible offsets.

Chapter 5. Disorder engineering and conductivity dome in ReS₂ with electrolyte gating

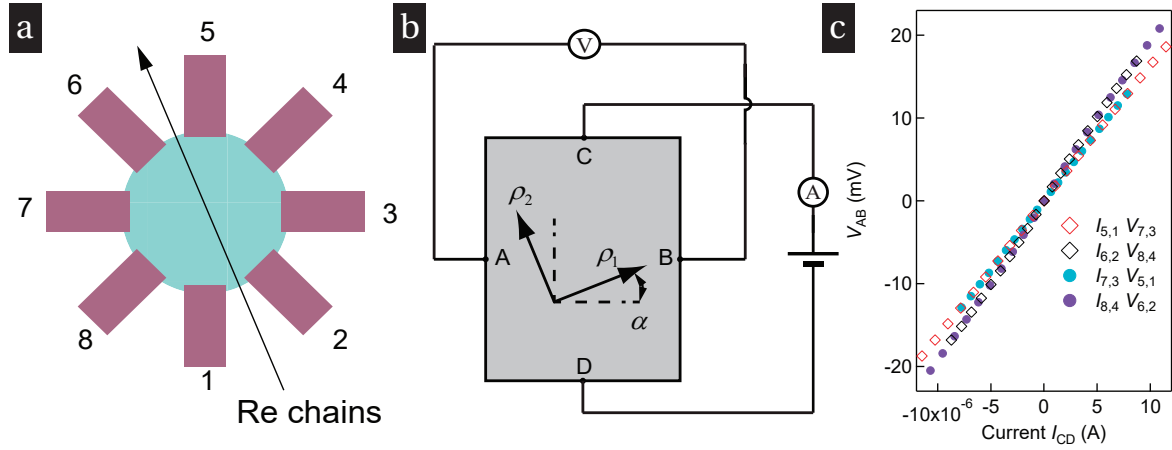


Figure 5.15 – Anisotropy and Hall effect in ReS₂. (a) Schematic of the device used with probes numbers from 1 to 8. Re chain, which corresponds to "easy" axis of the crystal, is determined from experimental data. (b) Schematic illustration of measurement scheme with the direction of easy axis marked. (c) Reciprocal voltages, recorded from all pairs of probes in configuration, shown in (b). Adapted from Ref. [13].

On Figure 5.15a we show the schematic drawing of our sample. In fact we did not know a priori the direction of "easy" axis, but we could determine it from HE offsets at zero magnetic field in different directions. On Figure 5.15b we sketch schematically the measurement scheme for our sample. The transverse voltage $V_{A,B}$ in response to an applied current $I_{C,D}$ is given by [148]:

$$V_{A,B} = \left(-\frac{1}{2}(\rho_1 - \rho_2)\sin 2\alpha + C_H B\right) I_{C,D} \quad (5.1)$$

Where α is the angle between the direction of current flow and one of main crystallographic directions, ρ_1 and ρ_2 are resistivities along each axis, C_H is the Hall coefficient and B is the magnetic field. When measuring the carrier density, the anisotropic contribution manifests itself as an offset voltage at zero magnetic field. At zero magnetic field, Equation 5.1 is π -periodic and reciprocal measurements (swapping the current-carrying and voltage-reading pairs) are equivalent, as can be seen on Figure 5.15c, where lines for filled and empty markers correspond to reciprocal measurements. Having eight electrodes, we have two sets of four electrodes rotated by 45°, which allow us to obtain a system of two independent equations that can be solved to determine $(\rho_1 - \rho_2)$ and 2α :

$$V_{3,7} = \left(-\frac{1}{2}(\rho_1 - \rho_2)\sin 2\alpha + C_H B\right) I_{5,1} \quad (5.2)$$

$$V_{4,8} = \left(-\frac{1}{2}(\rho_1 - \rho_2)\sin 2\alpha + C_H B\right) I_{6,2} \quad (5.3)$$

5.4. Results: disorder engineering and conductivity dome in ReS₂ with electrolyte gating

Having solved 2α we can now assign the direction of the easy axis (here $\alpha \approx 20^\circ$). Finally, we perform van der Pauw (vdP) measurements. It is known [149] that for anisotropic material the solution of the vdP equation gives $\sqrt{\rho_1\rho_2}$. Knowing $\sqrt{\rho_1\rho_2}$ and $(\rho_1-\rho_2)$ we can furthermore calculate the absolute value of resistivities. Moreover, the ratio between resistivities we obtain contains no error due to the contact resistance. We find the ratio of $\rho_1/\rho_2 \approx 0.57$.

We continue with Hall effect measurements on a three-layer device in the cross-like configuration. The measurements were performed in the following way - different values of V_{PE} were applied at room temperature, the current was stabilized and the cooldown was performed. Furthermore, the carrier density could be modulated with solid back gate (270 nm SiO₂) below the freezing point of the electrolyte. We varied the temperature to avoid non-linearities in the probe reading. We performed three cooling cycles - before the conductivity dome ($V_{PE} = 0.9V$), near it ($V_{PE} = 1.6V$) and right after it ($V_{PE} = 2.1V$). The typical Hall effect measurement is shown on Figure 5.16a, where the magnetic field B is changed in the range of 9.9T, while for each magnetic field point $V_{xy}-I_s$ was recorded. These curves appear to be linear. To avoid the impact of small non-linearities on our measurements, we further performed linear fitting and plot the data on Figure 5.16a, with the dependence of Hall resistance R_{xy} on the magnetic field B shown in the inset. On Figure 5.16b we summarize our measurements for 3 different cooling cycles and carrier densities. Variation of V_{bg} allows us to get the intersect between neighboring cooling cycles. From linear fit of n_{2D} from V_{bg} we can extract the capacitance of the solid back gate, which corresponds very well to the geometric capacitance of 270 nm SiO₂, thus ruling out any interplay between the frozen electrolyte and the back gate. On Figure 5.16c we show the carrier density, extracted for each V_{PE} at $V_{bg} = 0V$. From the slope the capacitance of the electrolyte can be extracted, which is on the order of $1.3 \mu F \cdot cm^{-2}$. This value is lower than in other systems with [EMIM]-[TFSI] (above $2 \mu F \cdot cm^{-2}$ for monolayer MoSe₂ [150] and WSe₂ [151] reported with voltammetry measurements), which might be related to work function mismatch between electrolyte and ReS₂ [41], but allows us to access all necessary regimes of operation of our devices. We refer the reader to 7.3.1 for further information regarding the estimated values of capacitance for different systems studied in the framework of this thesis.

The most important output of HE measurements is the direct and independent measurement of μ_{Hall} and n_{2D} for each specific value of V_{PE} and thus disorder strength. On Figure 5.16d we plot Hall mobility for two fixed carrier densities. Red markers correspond to fixed carrier density of $n_{2D} = 1.55 \times 10^{13} cm^{-2}$. At $V_{PE} = 0.9V$ metallic transport is observed with $\mu_{Hall} = 200 cm^2 \cdot V^{-1} \cdot s^{-1}$ at low temperature, while at $V_{PE} = 1.6V$ at the same carrier density mobility decreases almost by an order of magnitude, while the transport becomes weakly insulating. The same happens increasing the carrier density to $n_{2D} = 1.82 \times 10^{13}$

Chapter 5. Disorder engineering and conductivity dome in ReS₂ with electrolyte gating

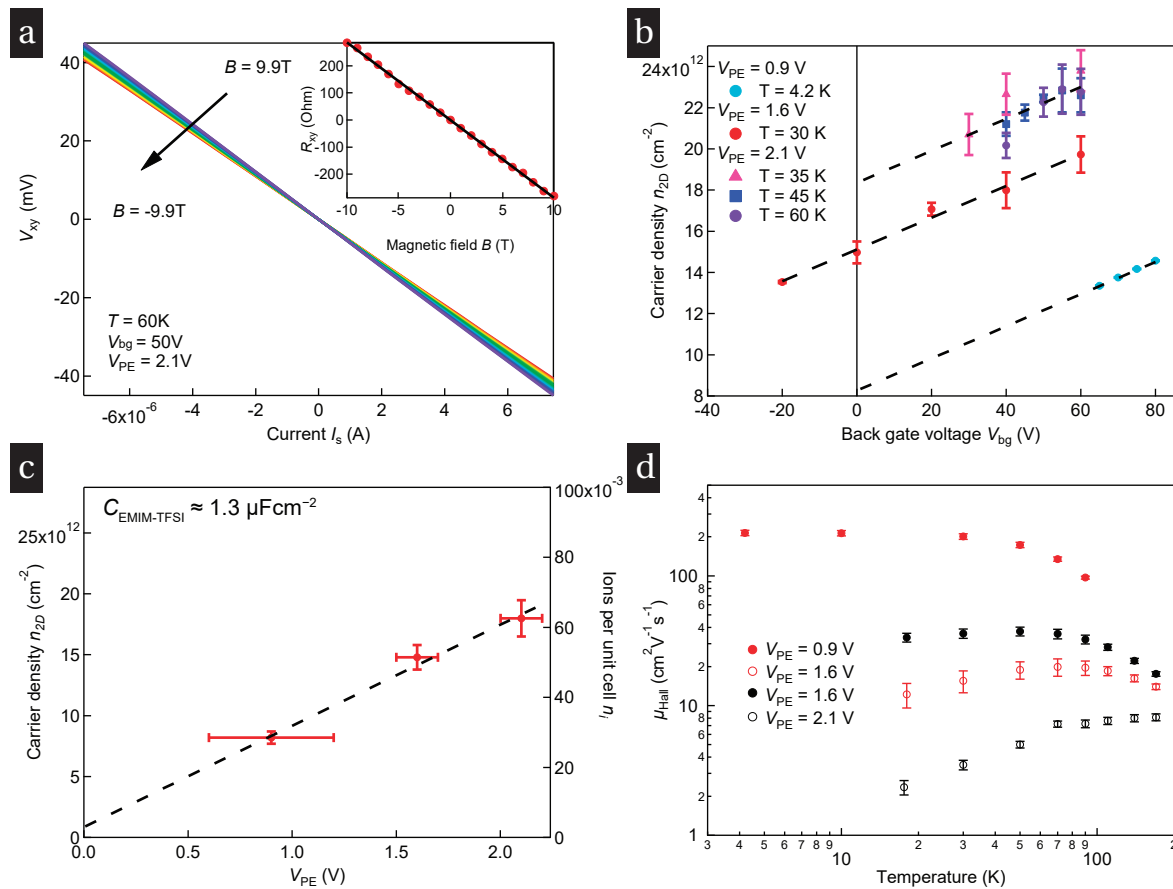


Figure 5.16 – Hall effect measurements in 3L ReS₂. (a) Hall voltage as a function of current and magnetic field. Inset - Hall resistance as a function of magnetic field. (b) Carrier density measured at different values of V_{PE} and back gate voltage V_{bg} . (c) Carrier density n_{2D} at different levels of V_{PE} . (d) Hall mobility for the easy axis of trilayer ReS₂ (2.2 nm thick) as a function of temperature T for different carrier densities and V_{PE} in the metallic state. Red markers correspond to fixed carrier density $n_{2D} = 1.55 \times 10^{13} \text{ cm}^{-2}$, filled - $V_{PE} = 0.9\text{V}$, empty - $V_{PE} = 1.6\text{V}$. Black markers - fixed carrier density $n_{2D} = 1.82 \times 10^{13} \text{ cm}^{-2}$, filled - $V_{PE} = 1.6\text{V}$, empty - $V_{PE} = 2.1\text{V}$. Error bars originate from the uncertainty in carrier density extraction from Hall effect and conductivity measurements. Adapted from Ref. [13].

cm^{-2} . These measurements indicate that by increasing disorder we decrease the mobility in the metallic state with fixed carrier density.

5.4.4 Insulating state at high carrier densities in multilayer ReS₂

The previous section discussed the overall behavior of multilayer ReS₂ at different levels of disorder and carrier density as a function of temperature. Two transitions in temperature dependent transport were observed. First is a standard band edge insulator to metal transition [147], the second one is metal to insulator transition at high doping levels which

5.4. Results: disorder engineering and conductivity dome in ReS₂ with electrolyte gating

we assign as a transition happening due to increasing strength of electrostatic disorder. The first evidence of this comes from Hall effect data in Section 5.4.3, where depletion of mobility with increase of electrolyte voltage is observed. Furthermore in this section we concentrate on the second transition and study the insulating state. We point to the absence of such transition for other semiconducting multilayers of TMDCs at high carrier densities [40, 41, 42, 43], making ReS₂ unique in this respect.

We attempt to understand the exact transport mechanism of conduction in the insulating state at high V_{PE} . To do so, we analyse the reduced activation energy w [152], which could be expressed as:

$$w = -\frac{d\ln R}{d\ln T} \quad (5.4)$$

Where R is resistance and T is temperature. This quantity as a function of temperature can indicate the transport mechanism in the sample. We plot on Figure 5.17a w as a function of $\ln T$ for 10 nm thick flake, discussed in Figure 5.14. We distinguish two types of behavior. In the 96 – 172 K temperature range, the temperature dependence of the resistance can be fitted using the Mott VRH behavior [153] with the slope equal to 1/3 (red dashed line on Figure 5.17 is a linear fit with the slope of 0.36). We calculate theoretical density of states $D_{2D}^{theory} \approx 4.17 \times 10^{14} \text{eV}^{-1} \text{cm}^{-2}$ and localization length $\xi_{loc} \approx 0.35 \div 0.6 \text{nm}$. Localization length would vary from sample to sample and depend on doping, but we measured in general localization length below 1 nm in this range of voltages.

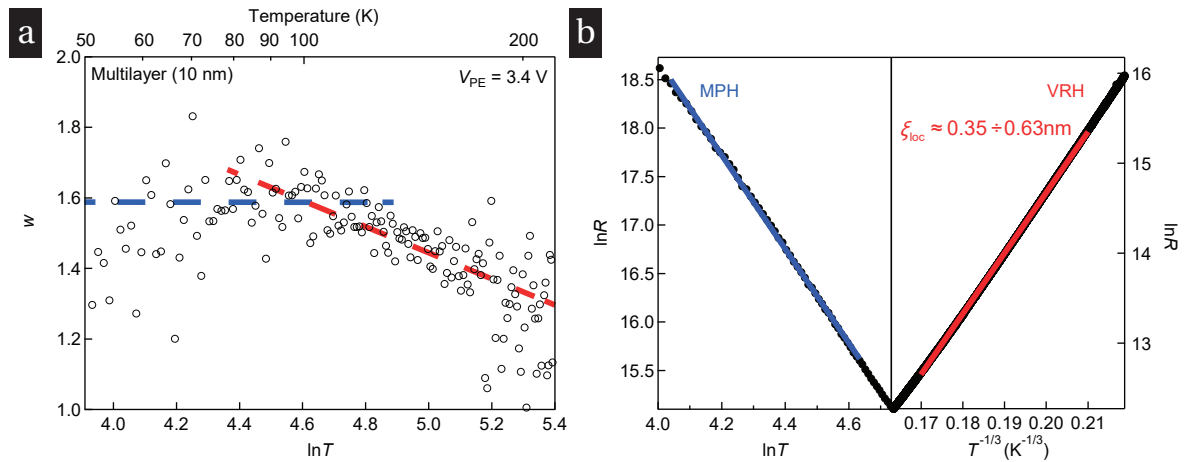


Figure 5.17 – Insulating state at high carrier densities in ReS₂. (a) Reduced activation energy w as a function of $\ln T$. Red and blue dashed lines correspond to variable range hopping (VRH) and multiphonon hopping (MPH) regimes respectively. (b) Fits for MPH (left) and VRH (right) in the corresponding range of temperatures. Adapted from Ref. [13].

Second, on Figure 5.17a at lower temperatures w saturates as a function of $\ln T$. This type of behavior could indicate the so-called multiphonon hopping (MPH) regime. In

Chapter 5. Disorder engineering and conductivity dome in ReS₂ with electrolyte gating

MPH regime resistance has a power law dependence on temperature $R \propto R_0(T/T_0)^p$, where exponent $p = -5$ could be extracted. It corresponds to the number of phonons that an electron exchanges energy with as it hops to its next location [154]. The temperature range for this distinctive plateau is 50 – 96 K. MPH is a typical feature of amorphous and disordered systems at low temperatures [154, 155, 156, 157, 158], but we do not exclude the possibility of such behaviour in multilayer ReS₂ at high n_{2D} . We are also aware of the fact that a clear distinction between two mechanisms might not be always possible due to similarities in the temperature dependence [154]. We notice, that in ref. [159] MPH in rubrene EDLT was observed after a similar mobility peak in the valence band of rubrene, but without a complete conductivity suppression like in monolayer ReS₂.

5.5 Theoretical calculations

Experiments performed on mono- and multilayer flakes of ReS₂ in EDLT configuration revealed strong modulation of conductivity at high carrier density and disorder levels, which could be directly related to electrolyte-induced disorder. To shed more light on unusual behavior of our devices, we performed band structure and transport calculations. Calculations were performed in Prof. Oleg Yazyev laboratory at EPFL by Diego Jose Pasquer and Dr. Fernando Gargiulo.

5.5.1 Band structure of ReS₂

Density Functional Theory calculations of band structure of mono- and multilayers of ReS₂ have been performed. The summary of these calculations is presented on Figure 5.18. Figure 5.18a-c shows the basic information regarding monolayer ReS₂, same is done for bulk on Figure 5.18d-f. The important output of these calculations is a narrow lowest energy conduction band, which is almost isolated from the rest of the density of states, as shown by purple lines on Figure 5.18c. The bandwidth of this narrow conduction band is around $D \approx 0.4\text{eV}$. Similarly, on Figure 5.18f bulk ReS₂ has a narrow lowest energy conduction band.

From diagonalization of the effective mass tensor for the monolayer, we find that m^* reaches the minimum value $m_L^* = 0.48m_e$, where m_e is the electron mass, along a “light” direction that forms an angle $\theta = 9.5^\circ$ with respect to a Re atom chain, whereas along the orthogonal “heavy” direction we find $m_H^* = 0.92m_e$. The calculated anisotropy ratio $m_L^*/m_H^* = 0.53$ is very close to the one measured for conductivity (see Sections 5.4.1 and 5.4.3).

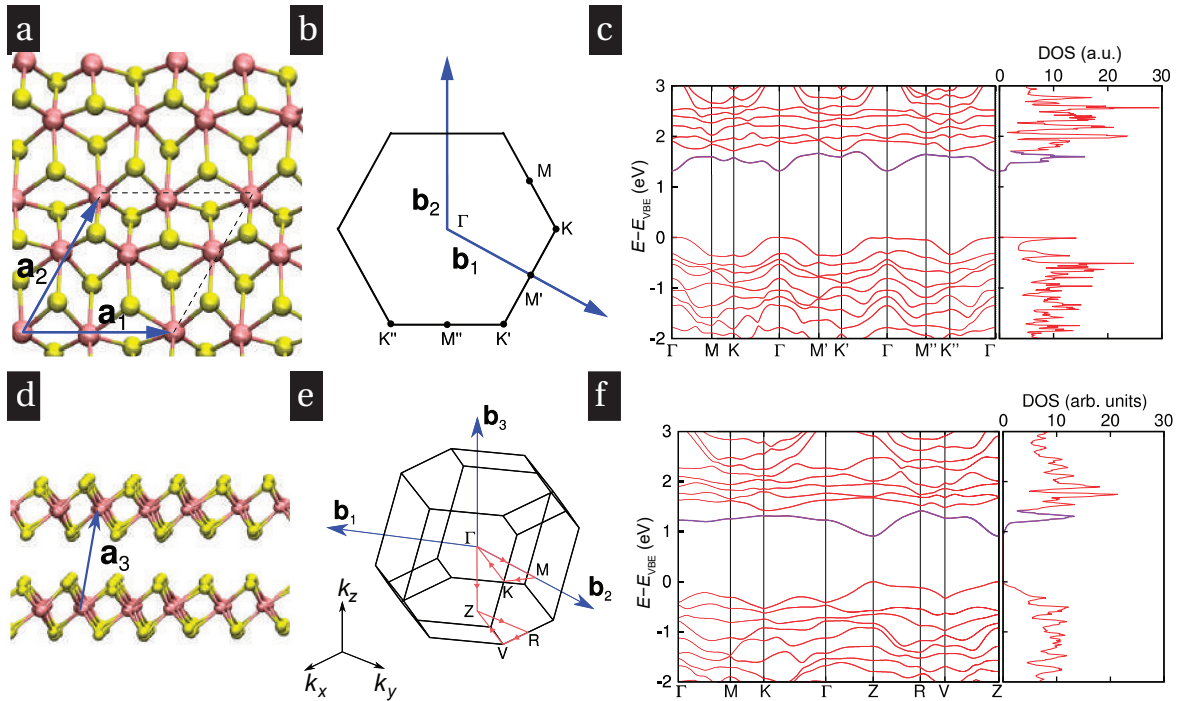


Figure 5.18 – Electronic structure of (a-c) monolayer and (d-f) bulk ReS₂ from *ab initio* calculations. (a) Ball-and-stick representation of monolayer ReS₂. Primitive vectors \mathbf{a}_1 and \mathbf{a}_2 are illustrated. (b) Brillouin zone and primitive vectors \mathbf{b}_1 and \mathbf{b}_2 of reciprocal lattice. (c) Energy bands calculated along high-symmetry directions connecting the vertices defined in (b) and k -integrated density of states (right panel). The lowest energy conductance band as well as its contribution in the DOS are highlighted in purple. (d) Ball-and-stick representation of the atomic layer stacking of bulk ReS₂. Primitive vector \mathbf{a}_3 is illustrated. (e) Brillouin zone, primitive vectors \mathbf{b}_1 , \mathbf{b}_2 , and \mathbf{b}_3 of reciprocal lattice, and k -point path for band structure calculation (red lines). (f) Energy bands calculated along high-symmetry directions connecting the vertices defined in (e) and k -integrated density of states (right panel). The lowest energy conductance band as well as its contribution in the DOS are highlighted in purple. Adapted from Ref. [13].

5.5.2 Alternative explanations for conductivity suppression

Prior to proceeding with transport calculations, we check alternative explanations of conductivity suppression, employing theoretical calculations. In the following we list them:

- Structural phase transition due to doping
- Fermi level reaching the dip in the density of states (DOS) upon doping due to the complete filling of the narrow conduction band
- Band structure modifications induced by the transverse electric field generated by

the electrolyte gate

Possibility of a phase transition due to doping. Doping effect on anisotropy has been already discussed. We did not find any signatures of significant anisotropy modulation in the range of carrier densities we can access. However, we point to the fact of merging curves on the right side of Figure 5.11a, which will be discussed later. To support our experimentally measured anisotropy with theoretical calculations, structural optimization calculations have been performed for different levels of doping, on various supercells of ReS₂. Our calculations did not reveal any phase other than the 1T' phase with 2×2 periodicity that always appears to be the energetically most favorable. Moreover, we verified that doping does not significantly alter the energy bands, except for the position of the Fermi level.

Filling of the narrow conduction band. This explanation is in principle supported by the almost perfect disentanglement of the first conductance band and correspondingly, the presence of a partial suppression in the DOS. Nevertheless, complete filling of the band translates into adding exactly 2 extra electrons per unit cell (including spin degeneracy), whereas the highest charge concentration measured in experiments is about 0.08 electrons per unit cell ($2.3 \times 10^{13} \text{ cm}^{-2}$), thus ruling out this hypothesis.

Electric field influence on the band structure. Band structure calculations within DFT for monolayer ReS₂ including a perpendicular electric field with intensity varying in the $1 - 8 \text{ V} \cdot \text{nm}^{-1}$ range (which covers the range of expected fields at the interface) have been performed. Only minor changes in the low-energy region with respect to the energy bands of the unperturbed system were found. Therefore, we exclude the electric field as a source of the observed conductivity decrease.

5.5.3 Discussion and transport calculations

Further in this section we concentrate on qualitative explanation of our findings. We first come back to the interface between the polymer electrolyte and the ReS₂ channel. Depending on the strength of interaction between ions and charge carriers inside semiconductor, and the effective mass of electrons, a bound state could be formed which prevents transport. As discussed in Section 5.5.1 ReS₂ has a narrow conduction band with a width of 0.4eV and large effective mass $m^* = 0.5 m_e$. This makes ReS₂ very similar to organic semiconductors, for example p-doped rubrene (highest occupied molecular orbital (HOMO) bandwidth $D \approx 0.4 \text{ eV}$, hole effective mass $m_h^* = 0.6 m_e$, ref. [160]). Remarkably, rubrene shows similar conductivity dome [159, 161, 162] with energy activated, VRH and MPH conduction mechanisms at high hole densities [159]. An example of the abovementioned dome in rubrene is shown on Figure 5.19.

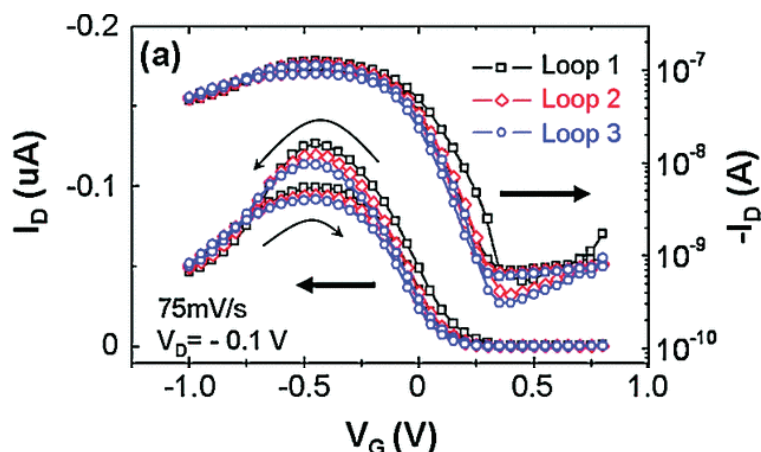


Figure 5.19 – EDLT based on organic semiconductor rubrene. Reprinted with permission from Y. Xia, W. Xie, P.P. Ruden, and C.D. Frisbie, "Carrier localization on surfaces of organic semiconductors gated with electrolytes", *Physical Review Letters*, vol. 105, no. 3, p. 036802, © (2010) by the American Physical Society.

A fully quantum argument based on Anderson localization allows us to qualitatively understand the mechanism of mobility suppression. Ions in electrolyte are randomly distributed and produce random Coulomb potential, which does not coincide with the periodicity of semiconductor lattice. Further in the text we assume, that imbalance between positive and negative ions (at positive V_{PE} applied) creates one electron in conduction band of ReS_2 . One-electron states could be described by the tight-binding model and the electrolyte-induced disorder consists of a random but spatially correlated distribution of on-site energies characterized by a finite width W .

Classical Anderson localization theory predicts, that any disorder strength leads to localization of one-particle states in two-dimensions [163, 164]. However, if one can modulate the disorder strength, as we do in our experiment by increasing the electrolyte voltage V_{PE} , larger amount of disorder W leads to shorter localization length [165, 166]. Electronic transport in the presence of localized spectrum has an insulating nature, the one which is observed in the present study. However, as the Anderson localization is ultimately a consequence of destructive interference of the wave functions, phase breaking mechanisms (e.g. electron-phonon scattering) that take place over a phase conservation length $L_\varphi \leq \xi$ prevent the physical realization of Anderson localization.

An increase of the number of ions at the electrolyte-semiconductor interface translates into the broadening of the overall on-site energy distribution, so that the effective amount of disorder W increases. Therefore, ξ is a decreasing function of V_{PE} . If one assumes that, at fixed temperature, L_φ does not vary considerably with doping, the condition for the onset of the metal-insulator transition is $\xi(V_{PE}^*) \approx L_\varphi$. For increasing gate voltage ($V_{PE} > V_{PE}^*$), charge-carrier mobility $\mu(V_{PE})$ is expected to drop faster than inverse linear law, leading to

Chapter 5. Disorder engineering and conductivity dome in ReS₂ with electrolyte gating

a rapid decay of conductivity $\sigma \propto n\mu$. We stress that the narrowness of the conduction band D is crucial to revealing the wavefunction localization, as the key quantity in Anderson localization is the adimensional disorder strength W/D [165, 167]. In our opinion, this phenomenon is responsible for such a peculiar behavior of monolayer ReS₂ among other 2D TMDCs.

In order to investigate qualitatively the discussed phenomenon, we consider the following model of electronic transport. We describe the lowest conduction band of ReS₂, highlighted in Figure 5.18c, with a tight-binding model on a rectangular lattice, with x and y directions corresponding to the parallel and perpendicular directions relative to the easy axis (along Re chains). Monovalent point charges (e.g. Li⁺) are placed at a distance $\Delta z = 20$ Å from the plane of the rectangular lattice. In order to guarantee the total charge neutrality of the ionic gate-semiconductor interface, the ionic concentration n_{ions} must be equal to the electron concentration n_{2D} .

To demonstrate the potential variations induced by ionic disorder, Monte Carlo simulations of the ionic distributions on top of conductive channel and corresponding induced potential variations were performed. The result is shown on Figure 5.20, where depending on ionic concentration n_{ions} per unit cell of ReS₂, the potential variation can reach up to 0.4V (Figure 5.20d).

Furthermore, the conductivity was calculated. The electrical conductivity has been calculated by means of the Kubo formula [168, 169] assuming a linear response to the applied electric field. Further details could be found in Ref. [13]. The output of the calculations is summarized in Figure 5.21. On Figure 5.21a the calculated DOS is presented, where long tail emerge with the increase of n_{ions} . These tails indicate the presence of localized states induced by electrostatic disorder (Figure 5.21b). Moreover, n_{ions} determines the chemical potential μ of the electrons, which shifts further into the conduction band upon increased doping. The transport behavior as a function of n_{ions} is ultimately determined by the interplay between the increasingly localized states of the spectrum and the position of the chemical potential within the conduction band.

Finally, the electrical conductivity along main directions in ReS₂ was calculated and compared with experimental values. On Figure 5.21c the conductivity dome is visible with full suppression at high values of n_{ions} . We compare the values of n_{ions} , obtained from theory with experimental values, which could be for example extracted from HE measurements, Figure 5.16c. We find a very good agreement between theoretical and experimental values of $n_{\text{ions}}^* = 0.06 \div 0.08$ on top of the conductivity dome. Second, we check the anisotropy of conductivity on top of the dome from theory and find the ratio $\sigma_y/\sigma_x = 0.6$ in agreement with two of our previous measurements - two-contact directional samples (Section 5.4.1) and Hall crosses (Section 5.4.3). Finally, we point to the region on Figure 5.16c above

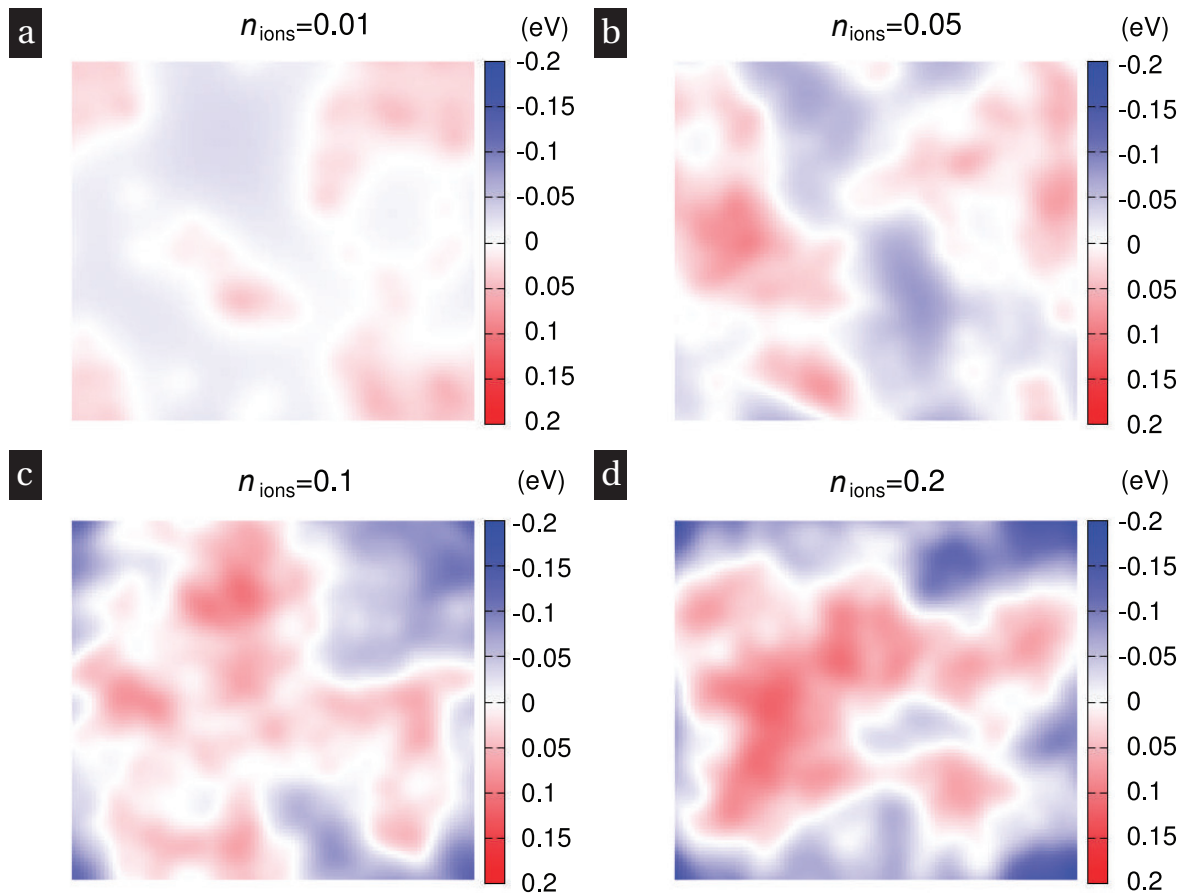


Figure 5.20 – Potential distribution at different ionic concentrations on the surface of ReS_2 . Adapted from Ref. [13].

$n_{\text{ions}} \approx 0.1$ where curves along two different directions become indistinguishable. This isotropic behavior can be seen in our room temperature two-contact measurements on Figure 5.11a. We ascribe this feature to the onset of full localization in the states in the energy region around the chemical potential, i.e. those states responsible for transport. Therefore, localization eliminates any preferential direction for transport.

Finally, we discuss the reason for such distinct difference between mono- and multilayers of ReS_2 . First, classical scaling theory of Anderson localization in $d = 2 + \varepsilon$ ($\varepsilon > 0$) dimensions predicts that extended states do not disappear entirely, but in the energy spectrum they are separated from localized states by so-called mobility edges. Second, the injection of electrons itself into the conduction band of ReS_2 results in a rapid screening of the Coulomb potential in the bulk of the sample, which is less affected by electrostatic disorder, thus preserving the charge-carrier mobility. These arguments point toward a scenario where the multilayer ReS_2 conductivity is less influenced by disorder than in the case of the monolayer. In fact, the topmost layer of ReS_2 in multilayers can act as a layer protecting from disorder in analogy with experiment, described in Ref. [87] on h-BN

Chapter 5. Disorder engineering and conductivity dome in ReS₂ with electrolyte gating

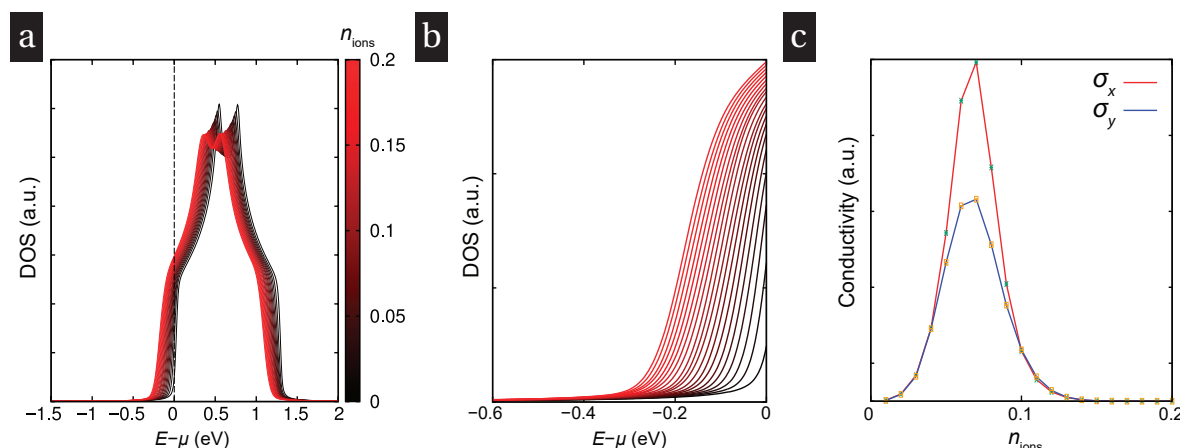


Figure 5.21 – Calculations of electronic transport for monolayer ReS₂. (a) Density of states modification due to addition of ions with the concentration $n_{\text{ions}} = (N_+ - N_-)/N_{\text{cells}}$ on top of conductivity channel calculated using our transport model. Color code corresponds to the amount of ions n_{ions} . (b) Close-up view of the conduction band edge. (c) Conductivities σ_x and σ_y as a function of ionic concentration n_{ions} for directions parallel and perpendicular to the "easy" axis (along Re chains), respectively, calculated using the Kubo formula. Adapted from Ref. [13].

protected STO samples.

5.6 Evidence of disorder effect in different monolayer TMDCs

In this Chapter we have shown that electrostatic disorder leads to modulation of mobility and conductivity in mono- and multilayers of ReS₂.

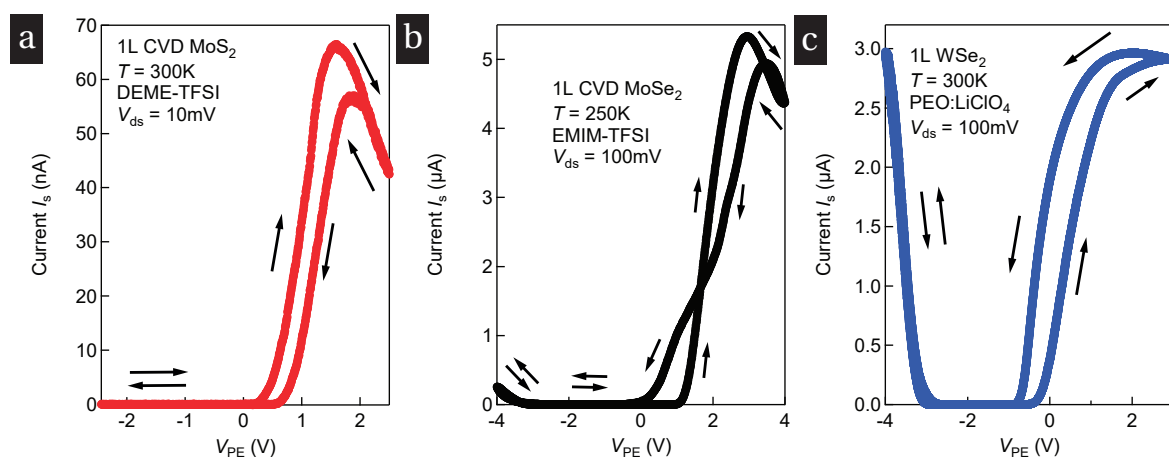


Figure 5.22 – Disorder in an EDLT based on monolayer TMDCs from two-probe measurements. (a) CVD MoS₂. (b) CVD MoSe₂. (c) Exfoliated WSe₂, additional data is reported in Ref. [58].

In this section we are going to discuss evidence of the impact of disorder on conductivity in other TMDCs, in particular in monolayers of MoS₂, MoSe₂ and WSe₂. We first plot characterization of EDLT devices with different types of IL or PE on monolayers of TMDCs. On Figure 5.22 we plot the acquired data for different monolayers. We measured CVD-grown MoS₂ and MoSe₂ and exfoliated monolayer WSe₂ [58]. The dome-like shape in conduction band does not seem to depend on the type of ionic media, source of material and sample preparation method.

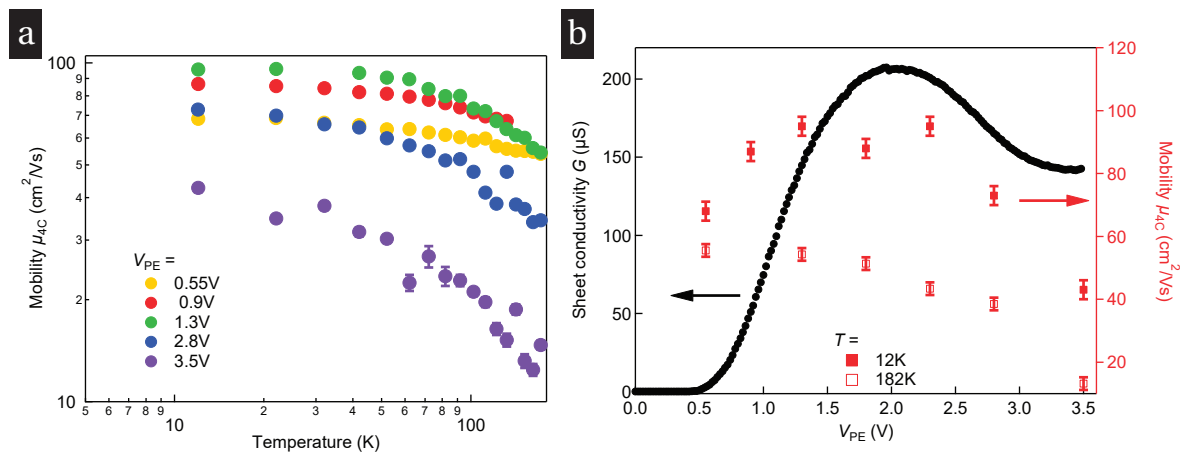


Figure 5.23 – Disorder in EDLT based on monolayer MoS₂. (a) Four-probe field-effect mobility μ_{FE} as a function of temperature, extracted at different values of V_{PE} . (b) Sheet conductivity at 278K (left axis) and mobility at 182K and 12K (right axis).

We also measured the four-probe field-effect mobility for an MoS₂ sample grown by metal-organic CVD (MOCVD) as a function of doping and temperature. The use of CVD material requires transfer from sapphire substrate to Si substrate, covered with SiO₂. Silicon acts as global back gate. The data in the metallic state (after MIT has occurred at the band edge) is presented on Figure 5.23a, where transport as a function of temperature for different V_{PE} is recorded. We plot this data on Figure 5.23b, where dome at 278K, mobility at 182K and 12K are shown. Interestingly, transport at all temperatures is impacted by the amount of disorder present in the system. Definitely, more work is needed to understand the exact difference between ReS₂ and other TMDCs, but qualitatively, the narrowness of the lowest energy conduction band in the case of ReS₂ plays a key role. We also notice, that there is not so much evidence of disorder in the valence band of any TMDCs, which will be discussed briefly in Chapter 7.

5.7 Follow-Up Work

Prior to our work researchers have been aware of disorder effect in EDLT based on different materials [87, 159], but systematic study has not been considered for any two-dimensional

Chapter 5. Disorder engineering and conductivity dome in ReS₂ with electrolyte gating

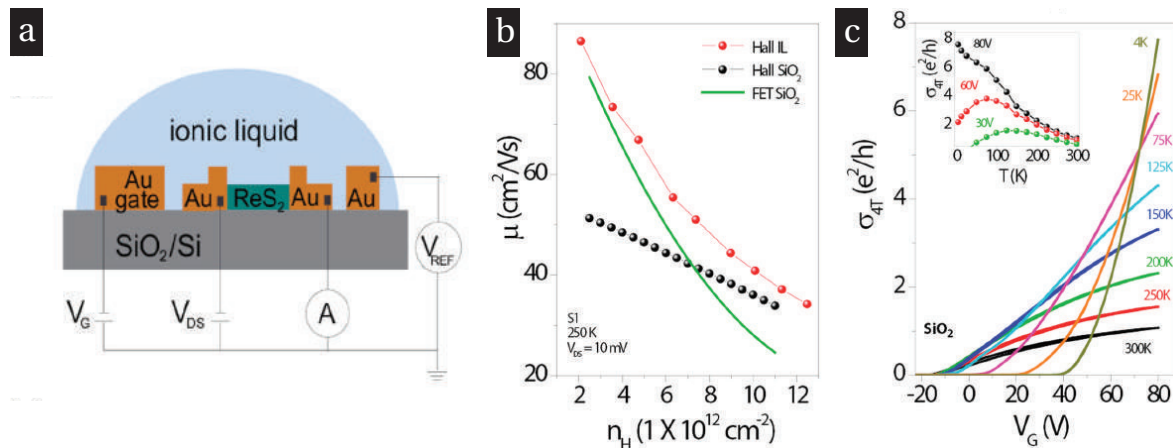


Figure 5.24 – Multilayer ReS₂ and the effect of disorder. (a) Schematic of EDLT based on multilayer ReS₂ with ionic liquid [DEME]-[TFSI] as gating media. (b) Mobilities, measured at 250K, indicating the effect of disorder at high carrier densities. (c) Metal to insulator transition in moderately doped multilayer ReS₂. Adapted from Ref. [25].

material. Disorder appears to be also important in EDLTs based on STO, as has been shown prior to our work [87]. Shortly after the work, based on dual-gated STO samples showed [170], that it is possible to modulate separately carrier density and disorder, similar to what has been done in our work.

Regarding the material itself, the effect of disorder was shortly after observed by a different group, this time with ionic liquid on multilayers of ReS₂ [25]. The discussed device is shown on Figure 5.24. Figure 5.24b shows the effect of electrostatic disorder, where moderate carrier densities and disorder levels already lead to decrease of carrier mobility at 250K.

5.8 Conclusion & Outlook

Our experimental work on ReS₂ shed light on several important points:

- We observed an unusual OFF state at high carrier densities in monolayer ReS₂.
- Electrostatic disorder and its impact on conductivity in ReS₂.
- Possibility to modulate disorder in the same sample *via* a combination of polymer electrolyte gate and back gate and thus mapping disorder and carrier density semi-independently.
- Importance of electrostatic disorder for other monolayer TMDCs.

We notice, that ReS₂ is a much less explored material than for instance MoS₂ and has a number of important differences, in particular linearly polarized excitons residing in this material, which could allow fabrication of polarization sensitive photodetectors [171, 172]. Our study points towards the need for a careful choice of device design and control of disorder levels. For example, "clean" h-BN encapsulated samples of mono- or multilayer ReS₂ have not been demonstrated yet. Very little work has been done in terms of optimization of device design. In particular, there is very limited information on the contact resistances and the choice of metal for injection of n- or p-type carriers in this material.

6 Epitaxial monolayer MoS₂

6.1 Introduction

This chapter is dedicated to engineering of grain boundaries between stitching single crystals of monolayer MoS₂ grown by Chemical vapour deposition (CVD). Previous experimental chapters dealt mainly with exfoliated material and in fact most of the breakthrough work on TMDCs, in particular first optical [18, 19], mechanical [47] studies as well as first high-performance device demonstrations [5, 47, 50, 53, 173] were based on exfoliated monolayers. Recent need for large area scalable methods and reproducible results moved research focus on growth methods. Molecular beam epitaxy (MBE) is a robust technique for existing semiconducting bulk materials but small progress has been done towards high quality large area production of MBE TMDCs. CVD is one of the most popular methods due to relatively low cost and straightforward growth procedure. However, similar to graphene case, films of synthetic MoS₂ have grain boundaries and thickness variations, which might impact electrical [74] and mechanical [8, 174, 175, 176] properties of 2D materials. It might be not favourable for example for applications, where large uniform films with good mechanical stability are required, like in flexible electronics [7]. Our approach was to control the orientation of as grown material employing the commensurate atomically smooth substrate. The presented chapter is based on the paper published in ACS Nano, 2015, 9 (4), pp 4611–4620 and the reader will find significant overlap between the above mentioned article and the following Chapter. This work is a result of collaboration between 3 first authors - Dumitru Dumcenco, Dmitry Ovchinnikov and Kolyo Marinov. Dumitru Dumcenco performed CVD growth, AFM and optical characterization of MoS₂, while Dmitry Ovchinnikov performed TEM measurements, large area device fabrication and characterization. Kolyo Marinov worked on single grain samples. Dmitry Ovchinnikov and Kolyo Marinov performed Kelvin Probe Force Microscopy (KPFM) investigation of grain boundaries. It is also important to mention theoretical collaborators, who contributed to this work, in particular Dr. Predrag Lazic, Dr. Marco Gibertini, Prof. Nicola Marzari.

Without their theoretical work the understanding of epitaxial CVD MoS₂ growth would not be complete. For the theoretical part please refer to Ref. [10].

6.2 Results: Epitaxial CVD MoS₂

Growth of monolayer MoS₂ by CVD is a well established process. In simple case, it requires reaction between two precursors containing Mo and S on the substrate at elevated temperatures. The related literature on CVD growth of TMDCs was discussed in details in Chapter 2. Our approach is to use the same process [72, 73] and to find a substrate, which would allow us to control the orientation of grains on the substrate and thus improve the quality of the overall film. The most suitable for our purpose is single-crystal Al₂O₃ - sapphire. Sapphire is used for example as a growth substrate for light-emitting diodes (LEDs) based on GaN and high-mobility transistors based on III–V semiconductors [177], which opens a path for integration of large area TMDCs into industrial process flows. We point to the fact, that CVD growth of TMDCs has already been performed on sapphire substrates [178, 179], but this is the first time epitaxial growth is achieved thanks to the special substrate preparation procedure, which will be described in the following section.

6.2.1 Substrate preparation and CVD growth

We start with commercially available EPI grade polished c-plane sapphire (University Wafers) which is first diced into 1 cm × 1 cm dies. An AFM image of the as-received substrate with the corresponding height histogram from a 500 nm × 500 nm area is shown on Figure 6.1a, c. The surface is relatively smooth, with the height histogram showing a standard deviation RMS = 154 pm (Figure 6.1c), lower than for typical SiO₂ surfaces (RMS ~ 300pm). The sapphire pieces are loaded in a quartz tube and annealed in a tube furnace in air for 1h at 1000 °C prior to the growth run. Following the annealing procedure, the samples are allowed to cool to room temperature in air before we place them in the CVD growth furnace. An AFM image of the surface after annealing is shown in Figure 6.1b and demonstrates the dramatic change in surface morphology during annealing. The resulting surface shows atomically flat surfaces [180] with atomic steps due to the small miscut induced during the cutting of the sapphire boule. The terrace edges follow the [1 1 $\bar{2}$ 0] direction on average [181]. Based on the height histogram (Figure 6.1d), we extract a step size ~ 2.1Å and a terrace width ~ 70nm. Terraces are atomically smooth, with a surface roughness RMS = 33 pm as determined from histogram in Figure 6.1d. This height variation is smaller than the diameters of oxygen, aluminum or sulphur atoms (122 pm, 242 pm and 205 pm respectively). Such atomically smooth surfaces allow the van der Waals interaction between sapphire and MoS₂ to control the lattice orientation during the CVD

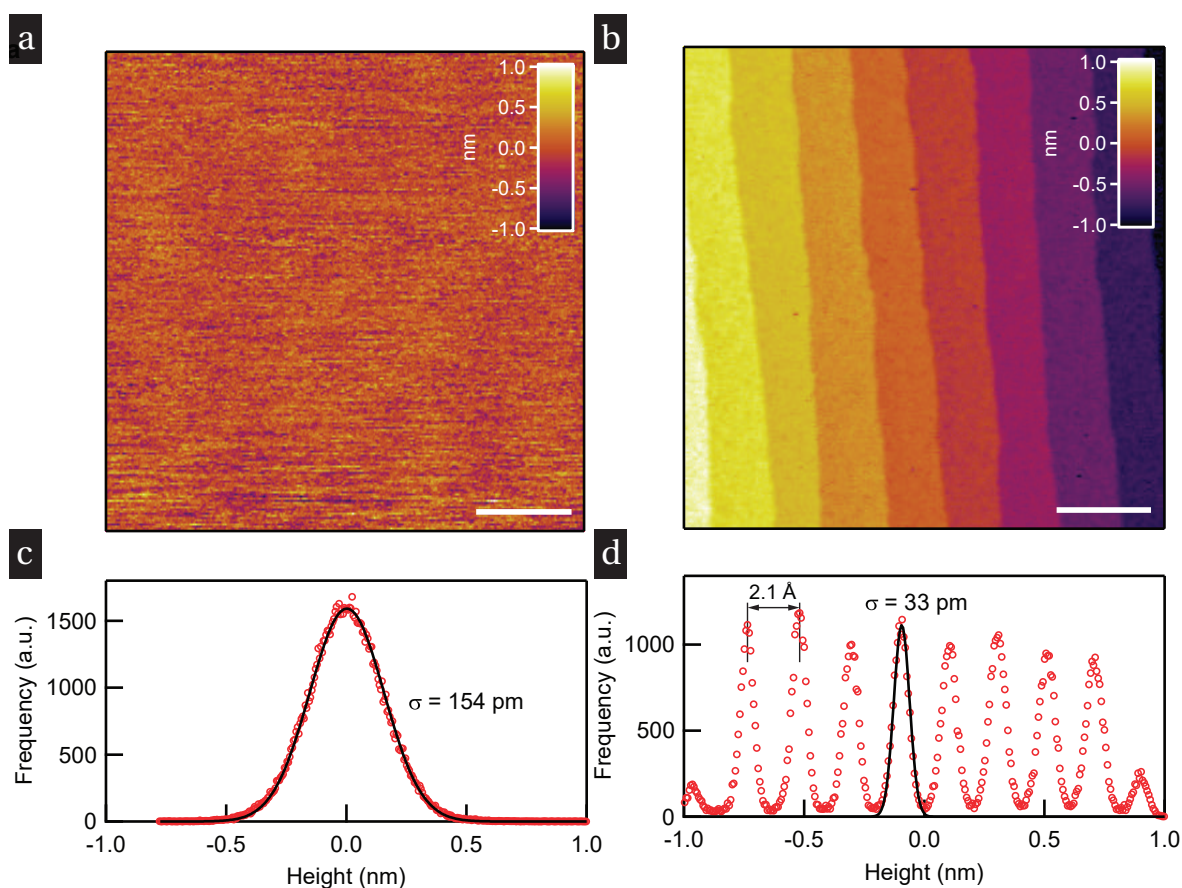


Figure 6.1 – Effect of annealing in air on the morphology of c-plane sapphire. (a) AFM image of the as received sapphire surface. (b) AFM image of annealed sapphire used here as the growth substrate. After annealing in air, the surface shows atomically smooth terraces. Scale bar is 100 nm. (c) Height histogram for AFM image in (a) with a Gaussian fit showing a standard deviation RMS = 154 pm. (d) Height histogram of image in (b) with a Gaussian fit showing a standard deviation RMS = 33 pm and a terrace height ~ 2.1 Å. The color scale in (a) and (b) is the same (2 nm). Adapted from Ref. [10], © (2015) American Chemical Society.

growth of monolayer MoS₂.

Furthermore, growth is performed in the CVD furnace using solid precursors. The schematic of employed setup is presented on Figure 6.2. The growth process is based on the gas-phase reaction between MoO₃ and sulphur evaporated from solid sources [72, 73] using ultrahigh-purity argon as the carrier gas. The boat with MoO₃ is placed in the middle of the hot zone of the furnace below the substrates, which are put above it facing down. Sulphur is put upstream in the colder part of the furnace due to lower melting point. In our configuration atmospheric pressure is used for the growth procedure.

We inspect our substrates after the growth process. The resulting film consists of equi-

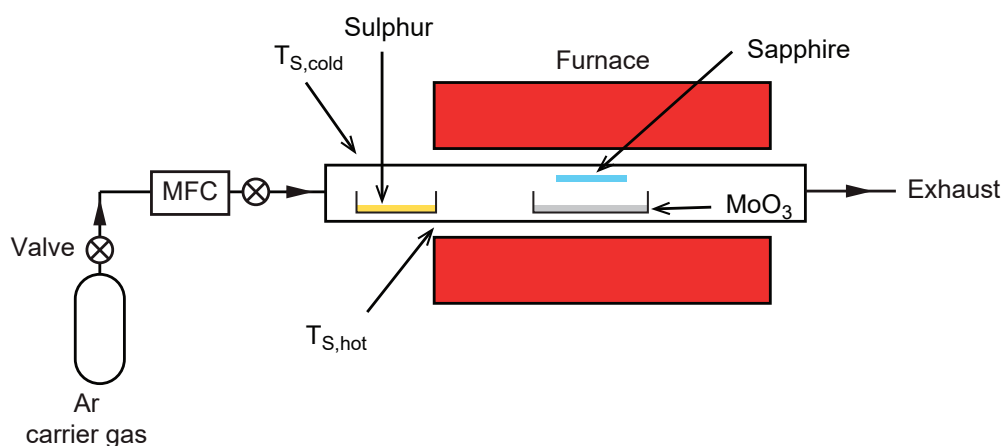


Figure 6.2 – CVD furnace setup. Adapted from Ref. [10], © (2015) American Chemical Society.

lateral single-crystal domains in the shape of triangles that merge into a continuous film with monolayer thickness covering typically the area of 6mm x 1 cm in the middle of the substrate, as shown on Figure 6.3a. We inspect each region in the optical microscope. Figure 6.3b shows the zoom in images of the edge of the film (top), where triangles are merging together and middle of the film, where they form a continuous monolayer. Careful examination of the region with incomplete coverage on Figure 6.3c shows, that most of the triangle edges have a fixed orientation. The majority (91.5% of islands shown on Figure 6.3c) of single-crystal domains are well aligned with the relative orientation of edges that can be expressed as multiples of 60°. This is confirmed by the orientation histogram presented on Figure 6.3f for the same area as on Figure 6.3c, showing that the dominant edge orientations are 0° and ±60°. A small fraction of domains (6% of islands on Figure 6.3c) show edges with a relative angle of ±30°, while the rest (2.5%) show other orientations.

To confirm the monolayer thickness of our material, we performed AFM imaging of as-grown triangles. On Figure 6.3d we show AFM images of the monolayer material on sapphire substrates (steps on sapphire are clearly visible) and extract the height across the black line, which is less than 1 nm and corresponds to monolayer thickness [141]. High-resolution TEM images confirm the crystal structure of hexagonal MoS₂ with no apparent defects as shown on Figure 6.3e with structural model overlaid. Further characterization by optical spectroscopy techniques, for instance Raman spectroscopy and photoluminescence measurements confirmed monolayer thickness and are beyond the discussion of this thesis [10]. We also found a good homogeneity of our films with large area adsorption experiments.

To demonstrate the importance of sapphire surface for our process, we also performed growth on as received substrates without above mentioned annealing step. The result

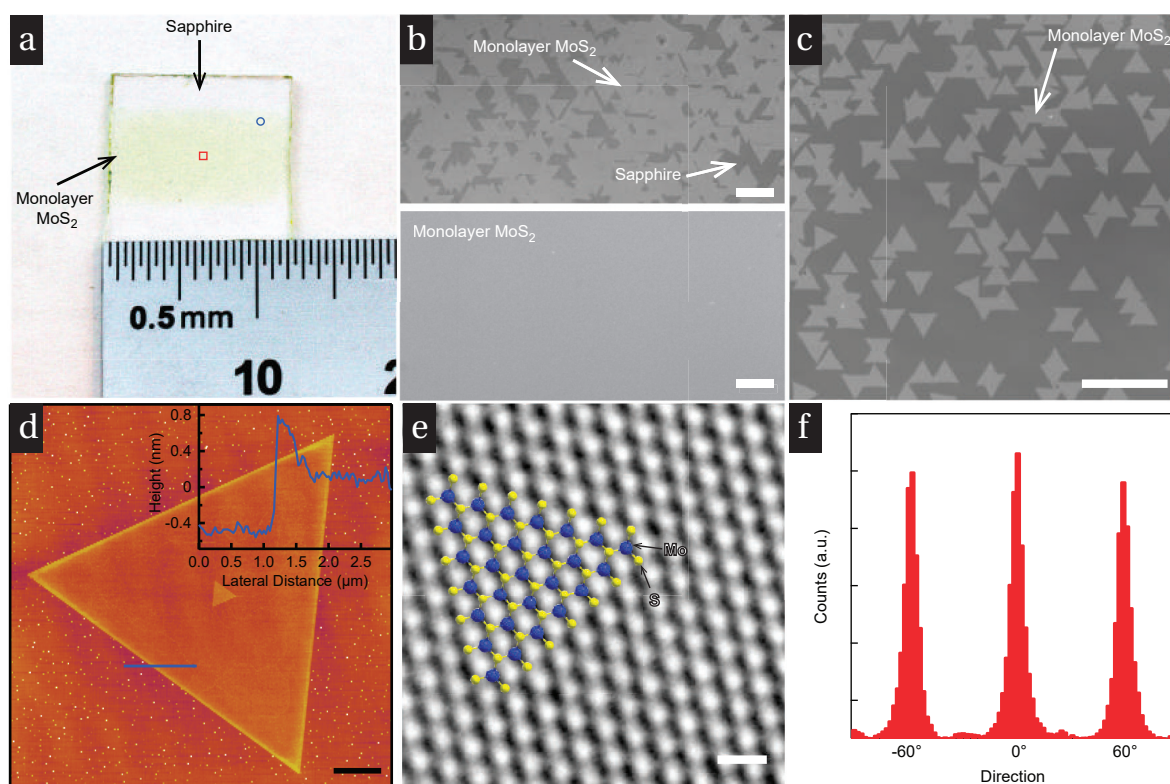


Figure 6.3 – Monolayer MoS₂ growth with controlled lattice orientation. (a) Photograph of cm-scale monolayer MoS₂ grown on sapphire. (b) Optical microscopy images from different regions of the sample showing incomplete coverage close to the edges (upper image, position marked by the circle in (a)) and full coverage close to the center of the growth substrate (lower image, position marked by the rectangle in (a)). Scale bar length is 20 μm on the top image and 10 μm for the bottom image. Original optical images were converted to greyscale and the contrast was enhanced. (c) Optical microscopy image of monolayer MoS₂ grains grown on atomically smooth sapphire. Scale bar length is 50 μm . (d) Atomic force microscope image of a monolayer MoS₂ grain. Scale bar is 2 μm long. Inset: line scan showing the thickness profile along the blue line in the AFM image. (e) High-resolution TEM image of a suspended MoS₂ film showing the crystallinity of the sample. Ball and stick structural model is overlaid. Scale bar is 0.5 nm long. (f) Orientation histogram based on the area shown in part c confirms that the majority of MoS₂ grain edges are oriented along 0 and $\pm 60^\circ$ angles. Adapted from Ref. [10], © (2015) American Chemical Society.

is shown on Figure 6.4a, where triangular grains of MoS₂ with small bilayers or seeds formation are visible. We proceed with analysis of relative grain orientation. On Figure 6.4b the directional analyses is performed, where no specific orientations were found. Another observation is the presence of small particles, presumably seeds, and thickness inhomogeneities of film. We speculate, that extremely small roughness of annealed substrates might promote the lateral rather than vertical growth and thus homogeneous thickness of our material (Figure 6.3b,c) is achieved, which could be understood as easy in plane atom

migration on the smooth surface of sapphire.

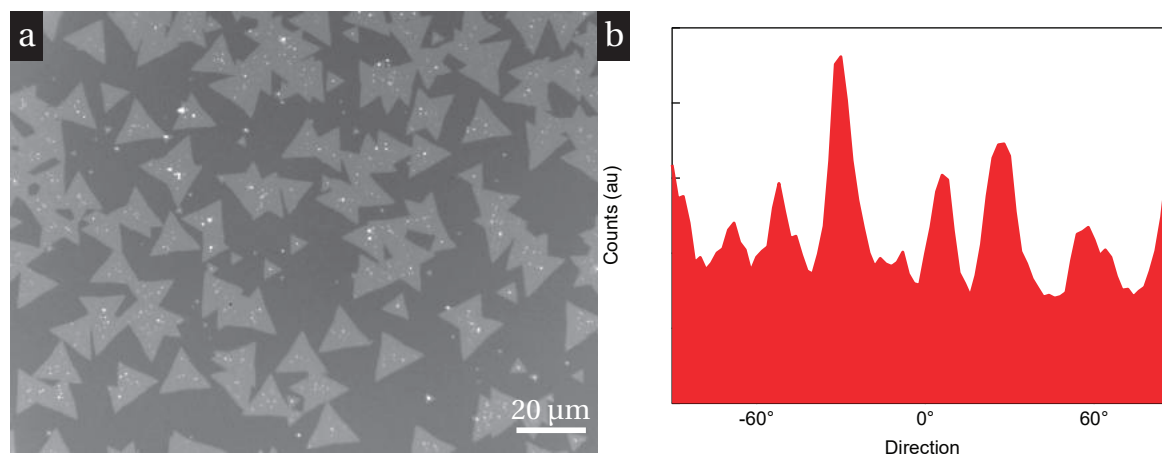


Figure 6.4 – Effect of sapphire surface annealing on the lattice orientation of CVD-grown MoS₂. (a) Optical image of a triangular MoS₂ single crystals grown on sapphire without annealing. (b) Orientation histogram obtained from the optical image in (a). Adapted from Ref. [10], © (2015) American Chemical Society.

6.2.2 Structural characterization

Optical images of our material indicate, that there is alignment between the edges of triangles in case the surface has low roughness. However, it was important to further investigate our material and establish relationship between crystalline lattice and triangle edge. To do so we analyze the large-scale crystal structure and their relative orientation using bright-field Transmission Electron Microscopy (TEM) imaging and selected-area electron diffraction (SAED). CVD MoS₂ was transferred from sapphire using the wet KOH transfer method. Briefly, samples were first spin coated at 1500 rpm with PMMA A2, resulting in a 100nm thick polymer film. These were detached in a 30% KOH solution, washed several times in deionized (DI) water and transferred onto TEM grids. TEM grids were annealed in the flow of Ar and H₂ for 8 hours at 400 °C in order to remove the polymer film. For low-resolution imaging and diffraction studies, 10 nm thick Si₃N₄ windows were used (<http://www.temwindows.com/>) while for high resolution TEM (HR-TEM) we used PELCO Holey Silicon Nitride Support Film with 2.5 μm holes in a 200 nm thick Si₃N₄ support. Transmission electron microscopy was performed using *JEOL 2200FS* operated in the 120 - 200 keV energy range.

First, we determine relationship between triangle edge and crystal lattice, which would allow us furthermore to use optical images as a reference. It can be done in the following way. The asymmetry of the Mo and S sublattices allows us to determine the orientation of the MoS₂ lattice with respect to the island edges. We pick up two triangles with a 60 degree relative rotation of edges. Furthermore, we inspect SAED from each of them. Since

an MoS₂ monolayer consists of two sublattices of Mo and S rotated by 60 degrees with respect to each other, this results in an asymmetry of diffraction pattern (DP) spots [182]. This asymmetry disappears in case of bilayer [182]. On Figure 6.5 such analysis is shown. From DP spot intensities of each of the two triangles we can extract the orientation of lattice with respect to the edges, as sketched on Figure 6.5a. All inspected triangles showed reproducible edge to lattice orientation. This result differs from the one obtained on SiO₂ substrates, where edge-lattice orientation was not fixed [72].

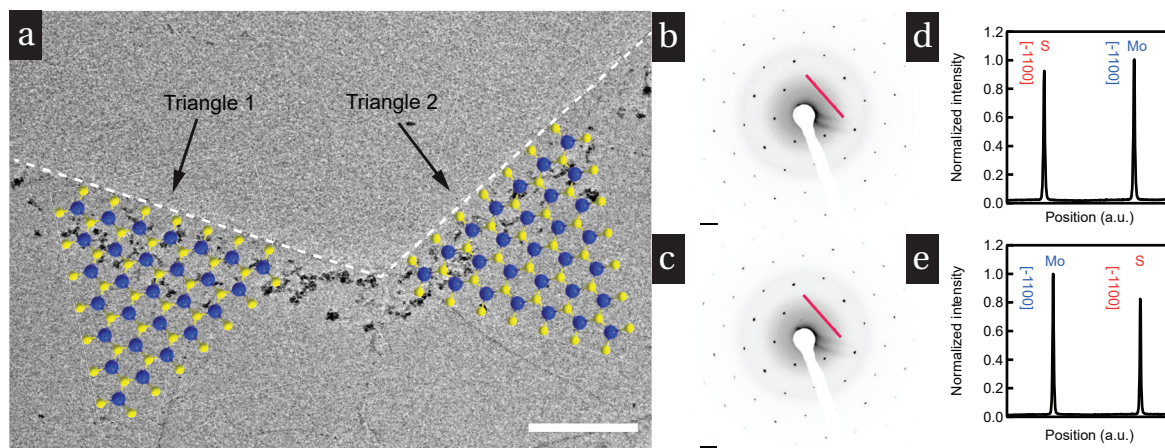


Figure 6.5 – SAED study of crystalline orientations of CVD MoS₂. (a) TEM micrograph of two merging triangles of CVD MoS₂ rotated by 180°. The overlaid structural model is for illustration only. Scale bar - 0.5 μm . (b) SAED diffraction pattern acquired on Triangle 1. Scale bar 2 nm^{-1} . (c) Same as b but for Triangle 2. Scale bar - 2 nm^{-1} . (d) Diffraction spot intensity plotted along the red line in b for Triangle 1. (e) Diffraction spot intensity plotted along the red line in c for Triangle 2. Adapted from Ref. [10], © (2015) American Chemical Society.

After we found the relationship between the edges and lattice of MoS₂, we turn our attention to alignment. Figure 6.6 shows a low-magnification image of group of aligned MoS₂ triangular islands. We closely examine a small region involving two neighboring islands by positioning the select-area aperture at the red circle containing two islands with their edges forming a 60° angle and acquiring the diffraction pattern shown in the inset of Figure 6.6a. Even though this diffraction pattern has been acquired from both triangles, we can only observe one set of diffraction spots with six-fold symmetry, showing the precise alignment of lattices in both of the islands, as shown on inset of Figure 6.6a. Figure 6.6b shows another example of a less frequent situation with two islands merging under a 90° angle. In this case, we can clearly distinguish two sets of $[\bar{1}100]$ diffraction spots, rotated by 30° (inset of Figure 6.6b).

The acquired experimental data points towards the fixed relationship between orientation of sapphire and MoS₂, which is obvious from statistically consistent optical images from multiple samples and connection between lattice and triangles orientation, which

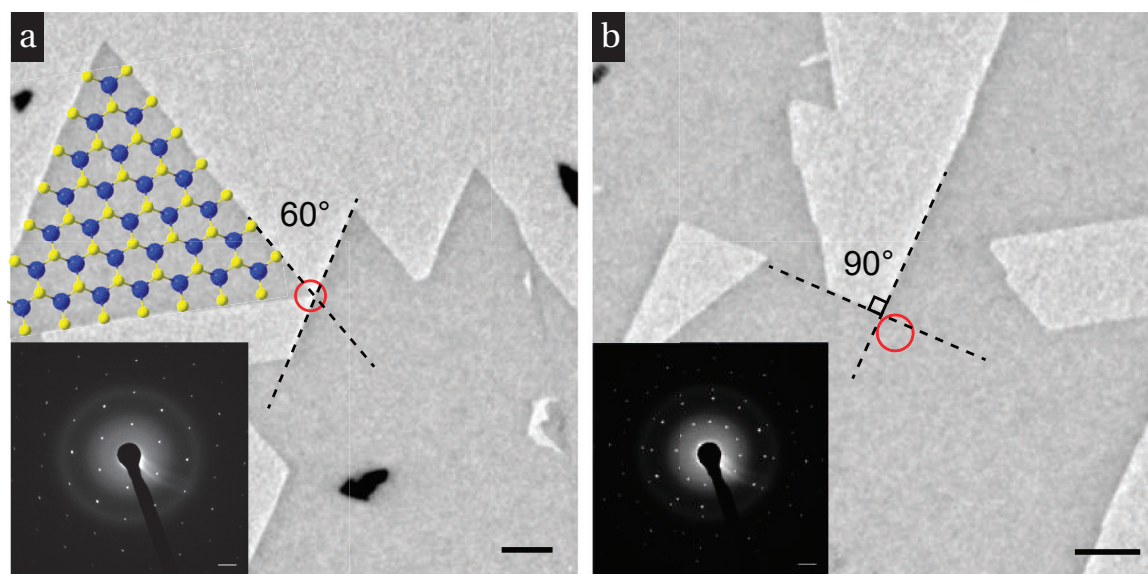


Figure 6.6 – Diffraction patterns from different island orientations. (a) Low-magnification TEM image of several neighboring MoS₂ islands. The diffraction pattern acquired from the area denoted with the red circle is shown in the inset and corresponds to the most common arrangement between neighboring islands. Only one set of diffraction spots can be detected from such islands, indicating that their crystalline lattices are aligned. The MoS₂ structure drawing indicates the lattice orientation within the single-crystal island and is not to scale. (b) Low-magnification TEM image and the corresponding diffraction patterns from two merging islands with their edges forming a 90° degree angle. Two sets of diffraction spots, rotated by 30° can be observed, indicating a 30° lattice misorientation angle. Adapted from Ref. [10], © (2015) American Chemical Society.

was obtained from TEM and SAED analyses. Furthermore, our collaborators performed theoretical calculations, which demonstrated that (i) interaction between MoS₂ and sapphire has almost exclusively vdW nature; (ii) it is possible to reproduce closely our experimental results of selected orientation by means of a simple model based on pairwise interaction between the closest atoms [10].

6.2.3 Electrical properties of large area MoS₂ films

After thorough characterization with variety of techniques and confirmation of our results with theoretical analysis [10], we start to explore the main goal of our study - whether we were able to preserve high electrical quality of the large-area material. We will leave single-grain characterization aside, details could be found in Ref. [10].

Central part of our sapphire chip is covered with a continuous monolayer MoS₂ film. Large-area films were transferred from sapphire to degenerately doped Si with thermally grown 270 nm SiO₂ on top using an optimized wet transfer technique. Briefly, the PMMA

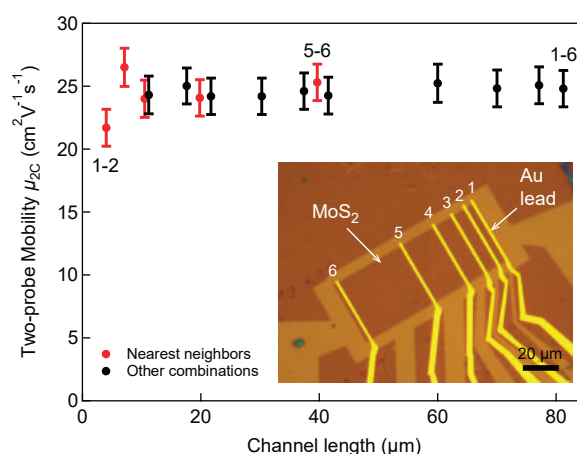


Figure 6.7 – Electrical properties of large-area devices. Field effect mobility as a function of channel length. Values are extracted from two-contact measurements performed on the device based on the continuous film shown in the inset with Au leads labeled 1-6. Red symbols correspond to values obtained using two nearest neighbor electrodes as source and drain terminals with the longest segment between electrodes 5-6 having a length of 39.7 μm . Black symbols denote values extracted by using other combinations of electrodes with the longest segment between terminals 1 and 6 with a length of 81.2 μm). Adapted from Ref. [10], © (2015) American Chemical Society.

A2 resist is used for transfer, but we skip the baking step not to induce any additional stress into the films. Si was used as global back gate. The measurements presented here were performed on the section of the large area film, which was contacted by multiple electrodes and etched into rectangular shape. The sample image is shown on Figure 6.7, inset. Our measurements were performed in vacuum below 10^{-6} mbar, after 50 hours of *in situ* annealing at 140 °C. This type of annealing, similar to WS₂, discussed in Chapter 4 [12] or other reports on MoS₂ [75, 104, 105], allows to restore the intrinsic properties of the material and to get rid of extrinsic sources of doping. The sample is a section of a continuous film with the length $L = 81.2 \mu\text{m}$ and width $W = 36.6 \mu\text{m}$, where two-contact field-effect mobility was measured for each pair of electrodes in one set of measurements. We can use two distinct configurations of leads: nearest neighbors, in which two neighboring leads are used as source and drain electrodes and other combinations allowing us to probe the full length of the device ($\approx 80 \mu\text{m}$) where the region between the source electrodes can contain multiple leads that are disconnected during the measurements. Such leads could be considered to represent invasive contacts and introduce additional scattering because of a local change in the chemical potential induced by the presence of a metal with a different work function than that of the semiconducting channel. This implies that mobilities obtained using such lead combinations could in fact be underestimated. Summary of our measurements is presented on Figure 6.7, where two-probe mobility stays constant over the length of 80 μm . The grain size in the sample under investigation is

roughly 10 μm, thus our channel contains multiple stitching between grains.

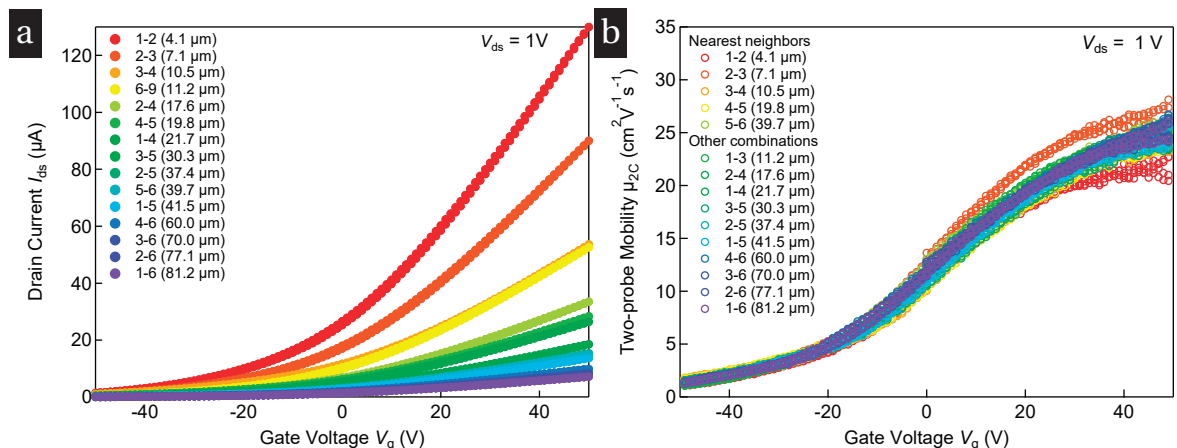


Figure 6.8 – Electrical properties of large-area monolayer MoS₂. (a) Drain current I_{ds} as a function of gate voltage recorded for different combinations of electrodes. (b) Two-contact field effect mobility extracted from the transconductance obtained by differentiating the curves in (a). Adapted from Ref. [10], © (2015) American Chemical Society.

The further details of these measurements are shown on Figure 6.8, where field-effect curves and dependence of mobility μ_{2C} on the gate voltage V_g is shown. Mobility curves from different pairs of electrodes are undistinguishable within the experimental error (Figure 6.8b). Mobility saturates at high V_g around the value of 25 cm² · V⁻¹ · s⁻¹, which is consistent with most studies on CVD MoS₂ material at room temperature [75]. Saturation of mobility itself is indicative of the band-like regime of operation with linear I_{ds} - V_g relationship.

6.2.4 Kelvin Probe Force Microscopy

In this section we use complementary a approach to judge on the electrical quality of grain boundaries. We use Kelvin Probe Force Microscopy (KPFM) [183] to resolve the local distribution of electrical potential on our films. KPFM technique is normally used to resolve workfunction variation on the surface of semiconductors and was successfully employed in case of graphene [94, 184] and MoS₂ [185]. In our case we use a slightly different approach - we employ the biased transistor in the ON state and image homogeneity of potential and thus resistance drop over the channel. For the KPFM measurement a Cypher atomic force microscopy system was utilized allowing the simultaneous measurement of topography and Kelvin voltage with spatial resolution of about 20 nm and a potential resolution of few millivolts. We used silicon KPFM probes (Asylum Research, 240TM) with nominal radius of 30 nm, which were covered with a conductive Ti/Pt (5/20 nm) layer and had a resonance frequency of 70 kHz. An AC modulation voltage V_{AC} of 3 V was applied to the probe for the Kelvin probe measurements.

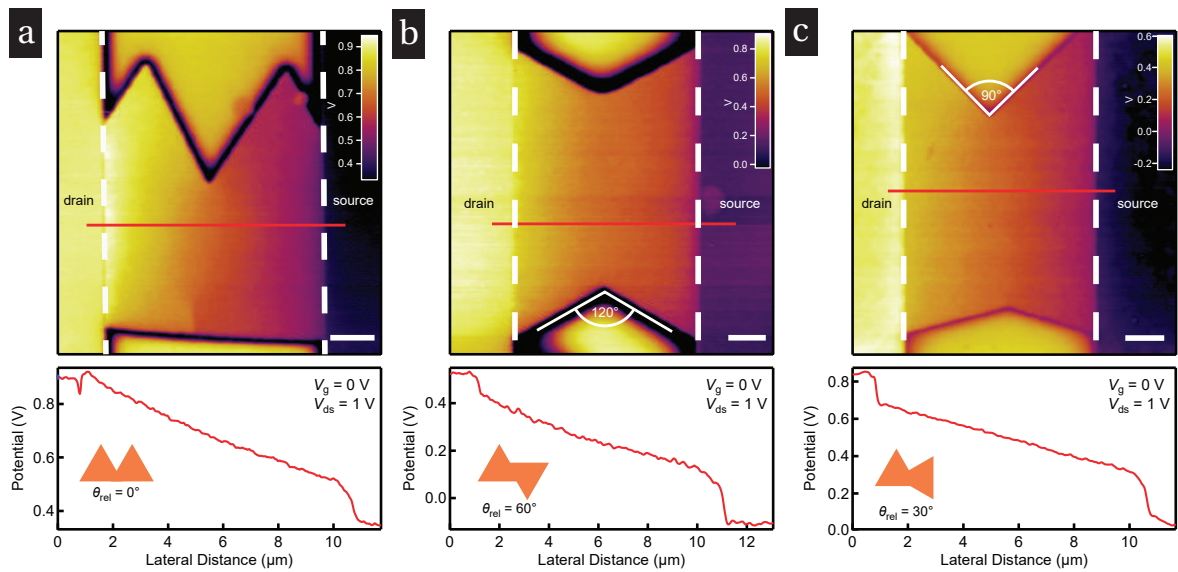


Figure 6.9 – Local potential map (upper panel) and line scan across the red line (lower panel) showing the potential drop over the conductive channel of a biased field-effect transistor based on two merged MoS₂ with (a) 0° misorientation, no grain boundary is expected, (b) 60° misorientation, (c) 30° misorientation. The smooth potential drop indicates the absence of abrupt changes of potential that would indicate the presence of an electrically resistive grain boundary. Insets in line scan plots indicate relative orientations of MoS₂ single crystals. Scale bars are $2\ \mu\text{m}$ long. Adapted from Ref. [10], © (2015) American Chemical Society.

The potential distribution across the channel allows us to judge on the local resistance variation of our material. In case of growth on SiO₂ substrates, Najmaei *et al.* [74] found that stitching between grains causes two-probe mobility degradation, which is not the case for large area devices in the present study. However, the local information was still not revealed by the measurements on large area devices, discussed in Section 6.2.3.

On Figure 6.9 we show the potential distribution for three main cases of mutual orientation of triangles. We used local bottom gates with thin layer of high-k dielectric ($30\ \text{nm}\ \text{HfO}_2$) to achieve sufficiently high doping without necessity to apply high voltages on the gate, while having direct access to the surface of our material. Even at $V_g = 0\text{ V}$ our transistors were already in the ON state. Top panels of Figure 6.9 show spatial distribution of electrical potential with $V_{ds} = 1\text{ V}$ applied, while bottom panels show slices of electrical potential across the red lines on top panels. For all three cases we did not find any visible sign of grain boundary impact on channel potential distribution.

6.3 Conclusion & Outlook

In this section we discussed engineering of grain boundaries in synthetically grown monolayer MoS₂. We chose atomically smooth substrate and were able to demonstrate preferential orientation in as grown films. Our effort was focused on engineering of linear defects between two stitching grains. This allows to synthesize large area film with homogeneous quality. The summary of this Chapter is as follows:

- We achieved epitaxial millilitre-scale MoS₂ by means of careful choice and treatment of growth substrate.
- Structural characterization revealed well-ordered homogeneous monolayer films.
- We characterized electrical quality of our films by means of large-area transport measurements and KPFM. Both techniques confirmed that our grain boundaries have no impact on electrical transport.

We point on the fact, that transparent and commercially available sapphire substrates together with the high quality of our films and unique optical properties of TMDCs open a way for fabrication of optoelectronic devices. Examples of possible devices include photodetectors [53], solar cells [54], p-n junctions with the possibility of control of chirality of emitted light [55, 186]. Recently we realized electro-optical modulators [56], where absorption of light could be controlled *via* gate voltage modulation.

In the follow up work we further explored the quality of our material and built different types of devices. High quality of our material was further confirmed by imaging of band structure [187] and magneto-optical experiments [188]. We were able to demonstrate power generation based on large area CVD MoS₂ [189] and an electroabsorption modulator (EAM) based on transparent MoS₂ transistor [56]. We also used H₂S as sulphur source and demonstrated similar quality CVD MoS₂ [11]. We will further discuss quality of material and devices based on CVD-grown TMDCs in Chapter 7.

7 High-quality synthetic 2D transition metal dichalcogenide semiconductors

7.1 Introduction

In Chapter 6 we discussed CVD-grown MoS_2 and focused on engineering of grain boundaries between the grains. However, it is important to further optimize the growth processes and to explore the growth of other TMDCs materials. In this Chapter we are going to discuss results on CVD growth of TMDCs and their structural and electrical properties. The inclination of this Chapter is mostly characterization of material rather than growth. This chapter is partially based on articles published in 2D Materials, Volume 2, Number 4 (2015) Ref. [11], as well as on Proceedings of the European Solid-State Device Research Conference (2016). Readers will find significant overlap between the following Chapter and mentioned publications. Dmitry Ovchinnikov was the second author in both articles, where he contributed to material characterization by TEM, device fabrication and transport measurements. Other data includes unpublished results by Dmitry Ovchinnikov and Dumitru Dumcenco on ambipolar insulator to metal transition in CVD-grown monolayer MoSe_2 and WSe_2 . All CVD growth and AFM measurements was performed by Dumitru Dumcenco.

7.2 Results: monolayer MoS_2 grown with H_2S as sulfur source

In this section we substitute solid sulfur by H_2S in a gas phase in a very similar process and explore the properties of resulting material. MoS_2 growth using H_2S as a gas-phase sulfur precursor results in highly-oriented vertically-aligned multilayers (not shown) or horizontally-aligned monolayer domains in the shape of well-defined equilateral triangles. We fine tune the parameters of growth and further discuss only horizontal monolayer domains in this section. Further details regarding the growth could be found in Ref. [11]. The overview of resulting sapphire chip is shown on Figure 7.1a with the edges covered by

Chapter 7. High-quality synthetic 2D transition metal dichalcogenide semiconductors

triangles (Figure 7.1b, top panel) which merge into a continuous film in the middle of the chip (Figure 7.1b, lower panel). AFM image of monolayer MoS₂ flakes is shown on Figure 7.1c, where monolayer thickness could be determined from height profile.

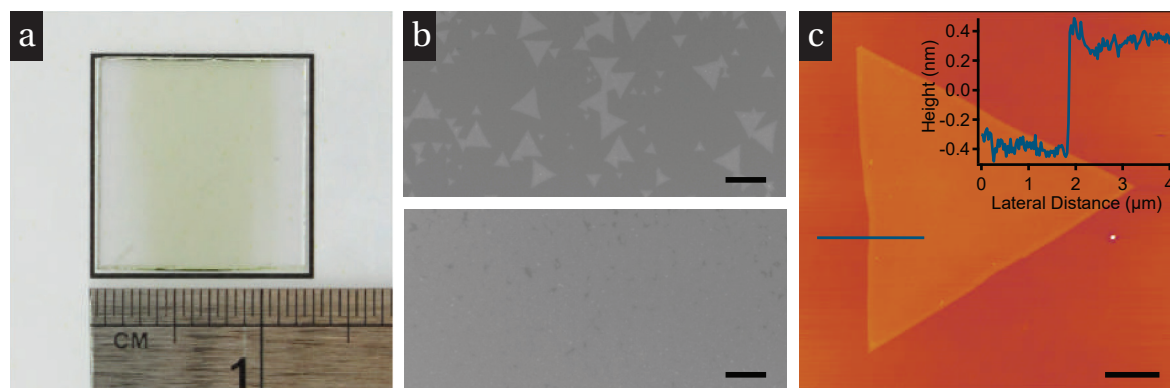


Figure 7.1 – Monolayer MoS₂ grown with 15:5 sccm of H₂S/H₂ introduced at 600°C. (a) Photograph of a cm-scale monolayer MoS₂ grown on sapphire substrate. (b) Optical microscopy images from different regions of the sample showing incomplete coverage close to the edges and an almost complete coverage close to the center of the growth substrate. Scale bar length is 10 μm. Original optical images were converted to greyscale. (c) AFM image showing a monolayer MoS₂ island. Scale bar length is 2 μm. Inset: The thickness profile along the blue line in the AFM image. Adapted from Ref. [11]. © (2015) IOP Publishing Ltd.

7.2.1 Structural characterization by STEM

To reveal the atomic structure of the material, we have performed a study of continuous MoS₂ film using aberration-corrected STEM *Titan Themis*, available in CIME, EPFL. In order to prevent damage during initial imaging of suspended single-layers, in Figure 7.2a fast acquisition of several (10-15) frames with 0.5s per frame has been used. The size of the recorded images was 512 × 512 pixels, which resulted in approximately 24 μs per pixel dwell time with 0.134 Å pixel size. We used beam currents below 50 pA, which resulted in relatively low doses of $3.5 \cdot 10^4 e \cdot \text{Å}^{-2}$ per frame for sub-sequential recording of each frame [190]. Finally, drift-correction and averaging of intensities with Digital Micrograph were used.

Figure 7.2a presents the lattice of MoS₂, imaged in this way and with a negligible beam-induced damage. Here, brighter spots correspond to Mo atoms and darker spots to stacks of two sulfur atoms. In general, contrast in STEM mode under these conditions of monolayer imaging is considered to obey the $Z^{1.7}$ contrast relation [91], which in the absence of contamination allows distinguishing between atoms with different Z number or between columns with different occupancy. Extracted from Fourier-transformed STEM images and used to draw the overlaid structural model, the lattice constant of $\sim 3.18 \text{Å}$ is in good

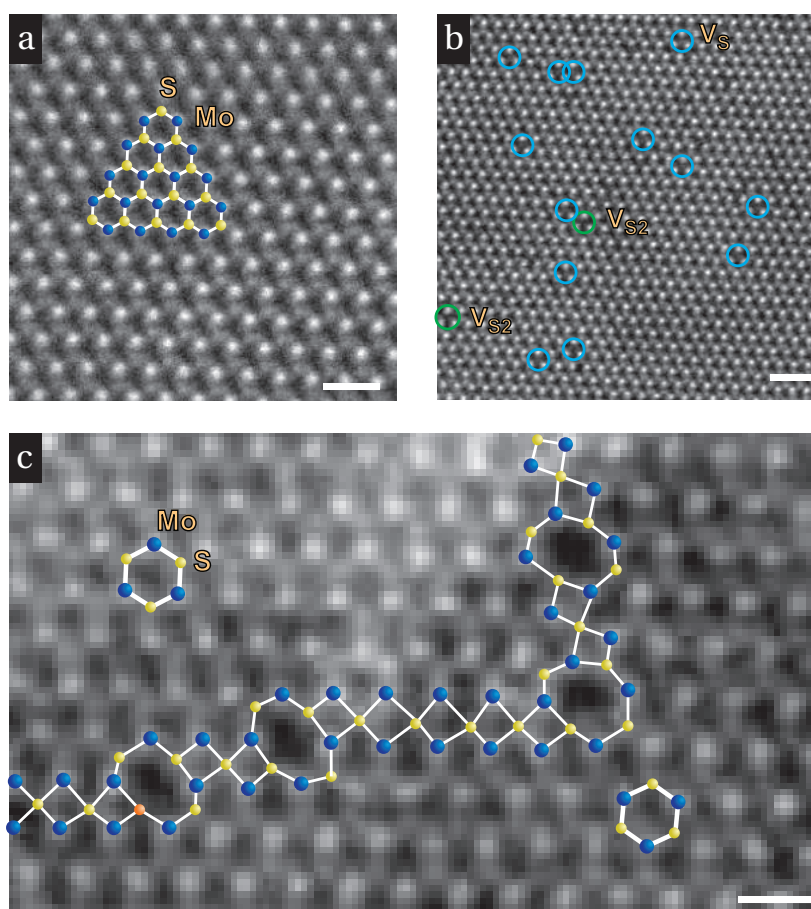


Figure 7.2 – Monolayer MoS₂ characterization with STEM. (a) STEM image of single-layer MoS₂ lattice with structural model overlaid. Scale bar 500 pm. (b) STEM image of a region, rich with sulfur vacancies, some of them are marked with circles. Blue: vacancies with one sulfur atom missing (V_S), green – vacancies with two sulfur atoms missing (V_{S2}). Scale bar 1 nm. (c) Overview of a grain boundary between two grains with a misorientation rotation angle close to 60°. Blue lines follow the grain boundary. Scale bar 2 nm. (d) Grain boundary between two grains with a misorientation rotation angle close to 60°. Proposed atomic model is overlaid, blue - Mo atom, yellow - 2xS atoms, orange - 1xS atom. Scale bar 500 pm. Adapted from Ref. [11]. © (2015) IOP Publishing Ltd.

agreement with the literature values [182]. In the single frame lower magnification images where the dose is even lower (total dose $1.25 \cdot 10^5 e \cdot \text{\AA}^{-2}$) one can see regions with point defects. As illustrated on Figure 7.2b, we can observe sulfur vacancies with one S atom absent (V_S), while occasionally we also observe vacancies with two missing S atoms (V_{S2}), circled in green. While we cannot completely rule out that these vacancies were introduced during imaging due to beam damage, they could well be inherent to the as-grown material. Indeed, we note that similar point defects were previously observed in CVD MoS₂ [191]. Next we studied the atomic structure of grain boundaries formed by two grains with their relative orientation close to 60°. As shown on Figure 7.2c, the grain boundary follows a

Chapter 7. High-quality synthetic 2D transition metal dichalcogenide semiconductors

zigzag direction, and is formed mainly by 4- and 8-fold rings.

A mirror twin boundary, which equally corresponds to a 60 degree relative orientation, has previously been observed to show 20 degree misorientation zigzag boundary faceting, with a periodic 8-4-4 ring motif along the facets [72]. In our case, although the zigzag misorientation angles are different, 8-fold rings connected by two 4-fold rings are also observed, as shown on Figure 7.2c. In addition, a chain of five 4-fold rings that connect two differently oriented 8-4-4-8 series of rings was observed. Such a difference is most probably related to the relative translational lattice shift and the small deviation from a perfect 60° orientation between the two grains. Moreover, it has been shown that grain boundaries can consist of distinct 4-fold ring chains forming one-dimensional metallic wires [191]. However, the proposed structure of long 4-fold ring chains would require perfect angle matching and epitaxial growth of MoS₂ on sapphire [10], which was not observed in this case.

7.2.2 Transport properties at room temperature

In this section we characterize our material building two-contact FET and measuring transport properties at room temperature. CVD-grown single domains of MoS₂ were transferred using PMMA A2 as a support film and etching in 30% KOH onto degenerately doped Si substrate covered with 270 nm thick SiO₂. The PMMA film was dissolved in acetone and residues removed by annealing in Ar atmosphere at 350 °C for 5 h. Electron beam lithography was used to define contact regions and 90 nm Au was used as the contact metal. PMMA A4 was used as the etching mask during oxygen plasma etching for some of the devices. The devices were then annealed at 200 °C in Ar atmosphere to eliminate resist residues and reduce contact resistance [5]. Further characterization was performed in vacuum at a base pressure of 10⁻⁶ mbar after annealing at 140 °C for 24 h.

We present the characteristics of a typical device after annealing on Figure 7.3. This device was etched into a rectangular shape. I_s - V_g characteristic is shown on Figure 7.3a, with $V_s = 1$ V applied. The field-effect mobility, extracted from two-contact measurements is presented on Figure 7.3b. The two-probe mobility, which does not take into account the effect of contact resistance, presents the lower estimate of intrinsic properties of the material. Values of mobility $\mu_{2C} = 20$ cm²·V⁻¹·s⁻¹ are in good agreement with recent reports on CVD MoS₂, grown from solid precursors on SiO₂ [75] and sapphire [10] substrates, which indicates a similar quality of the material. We estimate an I_{on}/I_{off} ratio around 10⁶ of this transistor at $V_s = 5$ V from the blue curve on Figure 7.3c. Finally, we inspect the quality of injection, performing I_s - V_s sweeps with the fixed gate voltages, shown on Figure 7.3d. The injection from Au electrodes is almost linear with no apparent hysteresis.

7.2. Results: monolayer MoS₂ grown with H₂S as sulfur source

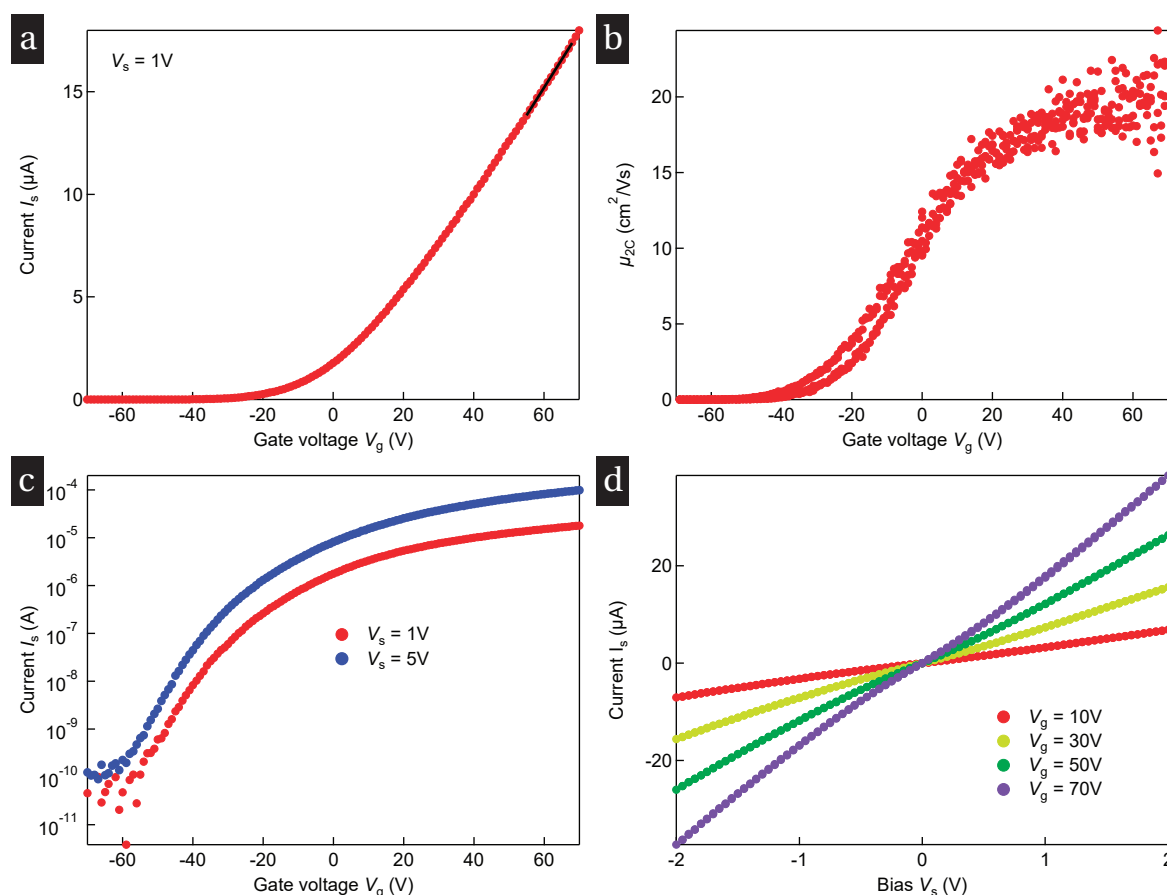


Figure 7.3 – Field-effect transistors characterization based on CVD MoS₂. (a) I_s - V_g characteristic of a typical field-effect transistor device. (b) Two-probe field effect mobility, extracted from (a). (c) Inset: I_s - V_g characteristic in the logarithmic scale. (d) I_s - V_s characteristics of the device at different gate voltages. Adapted from Ref. [11]. © (2015) IOP Publishing Ltd.

7.2.3 Conclusions

In this section we showed, that it is possible to perform growth of monolayer CVD MoS₂ with the combination of solid (MoO₃) and gas-phase (H₂S) precursor. By fine tuning of growth parameters we were able to achieve control over the direction of growth [11]. Furthermore, we characterized horizontally-grown single crystal domains of monolayer MoS₂ and showed structural and electrical quality similar to the exfoliated material as well as other reports on CVD MoS₂ [10, 72, 73, 75]. The observed doping levels are most probably related to sulfur vacancies and other clusters of defects, as observed in our material by STEM. One of the advantages in comparison with recent reports on MOCVD [77] is the fast growth process. The possibility of vertical growth opens a way to a variety of electrochemical applications, where reactivity of edges is required [192].

7.3 Results: Band-like transport and ambipolar insulator to metal transition in CVD grown WSe₂ and MoSe₂

In this section we are going to show for the first time the ambipolar band-like transport in single device based on monolayer Mo(W)Se₂. Difference between MoS₂ and Mo(W)Se₂ is the fact that p-type conduction is rarely observed in monolayer MoS₂. The reason for that is believed to be high trap density near the valence band edge [193]. There are several reports, indicating the possibility of p-type conduction in MoS₂ either with substitutional doping [194, 195] or by ionic liquid gating [193] but the information regarding conductivity in this regime is very limited, especially in the case of monolayers. Thus there is a number of open questions regarding possibility of observation of band-like transport in monolayer MoS₂ on the hole side. In this part of the thesis we employ scalable CVD-grown material to show devices, based on WSe₂ and MoSe₂, which exhibit both p- and n-type conduction. We observe ambipolar insulator to metal transition in our samples based on monolayers. This opens a way to fabrication of ambipolar transistors as well as light-emitting diodes. The importance of band-like transport can be understood, if we consider to employ broken inversion symmetry and spin-valley physics in future applications [9]. As soon as TMDCs in general exhibit band-tail, which originates from intrinsic or extrinsic sources of disorder, it is beneficial to use particles precisely from the CB or VB, which means that band-like transport should be achieved.

7.3.1 Electrolyte capacitance optimization

Prior to measurements, we choose the optimal regime of operation for [EMIM][TFSI]. In general, lowering the temperature of electrolyte increases the electrochemical window and capacitance. For instance, in Ref. [83] the authors found higher charge density accumulation in EDLT based on ZnO and wider range of voltages which could be applied at lower temperatures. We employ thin films of [EMIM][TFSI], which provide excellent mechanical stability, reproducible results and moderate capacitance. To estimate the capacitance of our polymer electrolyte, we performed measurements similar to Ref. [196], where shift of V_{th} of a back gate can be used to measure the capacitance of the electrolyte.

The example of such measurements for monolayer WSe₂ is shown on Figure 7.4, where sheet conductivity at different V_{PE} is measured for changing V_{bg} applied through Si/SiO₂. The resulting capacitance of [EMIM]-[TFSI] is $3.3 \mu\text{F} \cdot \text{cm}^{-2}$ at $T = 273\text{K}$. Similar measurements in CB of monolayer MoS₂ at 278K showed the capacitance of $3.2 \mu\text{F} \cdot \text{cm}^{-2}$. To put it in line with our previous data, we also performed measurements at room temperature. For example, for monolayer MoSe₂ the value of $1.6 \mu\text{F} \cdot \text{cm}^{-2}$ at $T = 300\text{K}$ in good agreement with the data on ReS₂. This capacitance measurements demonstrate the increase of

7.3. Results: Band-like transport and ambipolar insulator to metal transition in CVD grown WSe₂ and MoSe₂

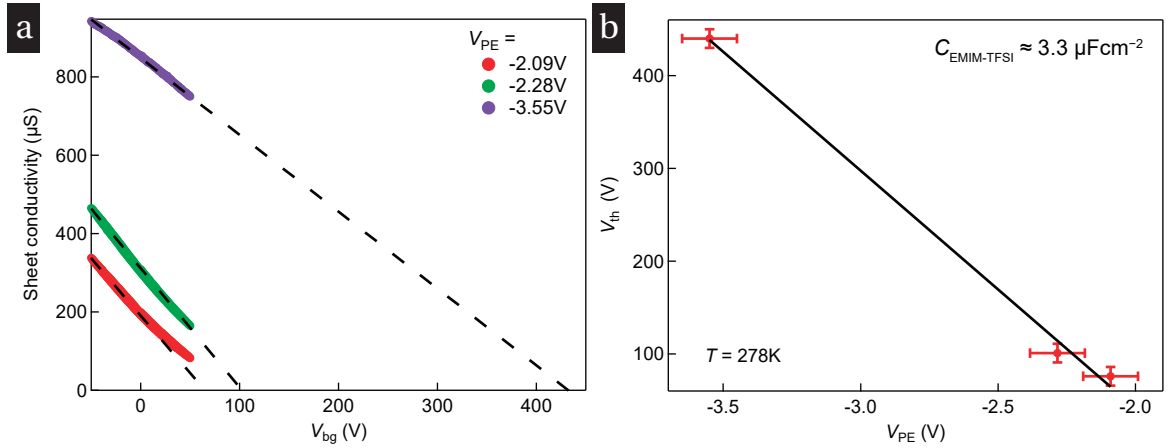


Figure 7.4 – Capacitance extraction for [EMIM]-[TFSI] on monolayer WSe₂ at 278K. (a) Sheet conductivity as a function of back gate voltage V_{bg} at different values of V_{PE} . (b) Threshold voltage, determined from (a) as a function of V_{PE} applied.

capacitance of [EMIM][TFSI] at lower temperatures.

7.3.2 Ambipolar insulator to metal transition in CVD grown WSe₂

For this section we used monolayer CVD-grown WSe₂ transferred on 20 nm Al₂O₃, the etched Hall-bar structure is shown on Figure 7.5a. We do not discuss the growth details here, but our samples were characterized by a variety of techniques and appear to be single-crystal domains of MoSe₂ and WSe₂ with the flake size of 20-120 μm, the growth results will be reported elsewhere. We mainly performed measurements applying V_{PE} at 278K, although our devices worked well at room temperature. On Figure 7.5b an overview of EDLT characterization is shown. We notice almost no hysteresis on p-side and more pronounced hysteresis on n-side of our EDLT V_{PE} sweep. Furthermore, we freeze electrolyte and perform temperature-dependent electrical conductivity measurements. Our back gate consists of 20 nm Al₂O₃ oxide with dielectric constant of 8.9 measured in test structures. We performed a series of cooldowns. Cooldown for p-side MIT is shown on Figure 7.5c, where crossover from insulator to metal in temperature is observed. Similar transition is observed on the n-side with positive V_{PE} applied.

We notice that the transition from insulator to metal on p-side has a much higher conductivity point than usually observed in monolayer MoS₂ or WS₂. The value of transition point on p-side corresponds to 240 μS or $6e^2/h$. In our previous work on monolayer WSe₂ we extrapolated, but did not observe this transition to the value or around $7e^2/h$ [58], which is in good agreement with the discussed experiment. The reason for this particular difference with conduction band MIT is not clear, but might imply participation of multiple valleys in conduction. The fact that only hole conductivity in +K and -K valleys (see

Chapter 7. High-quality synthetic 2D transition metal dichalcogenide semiconductors

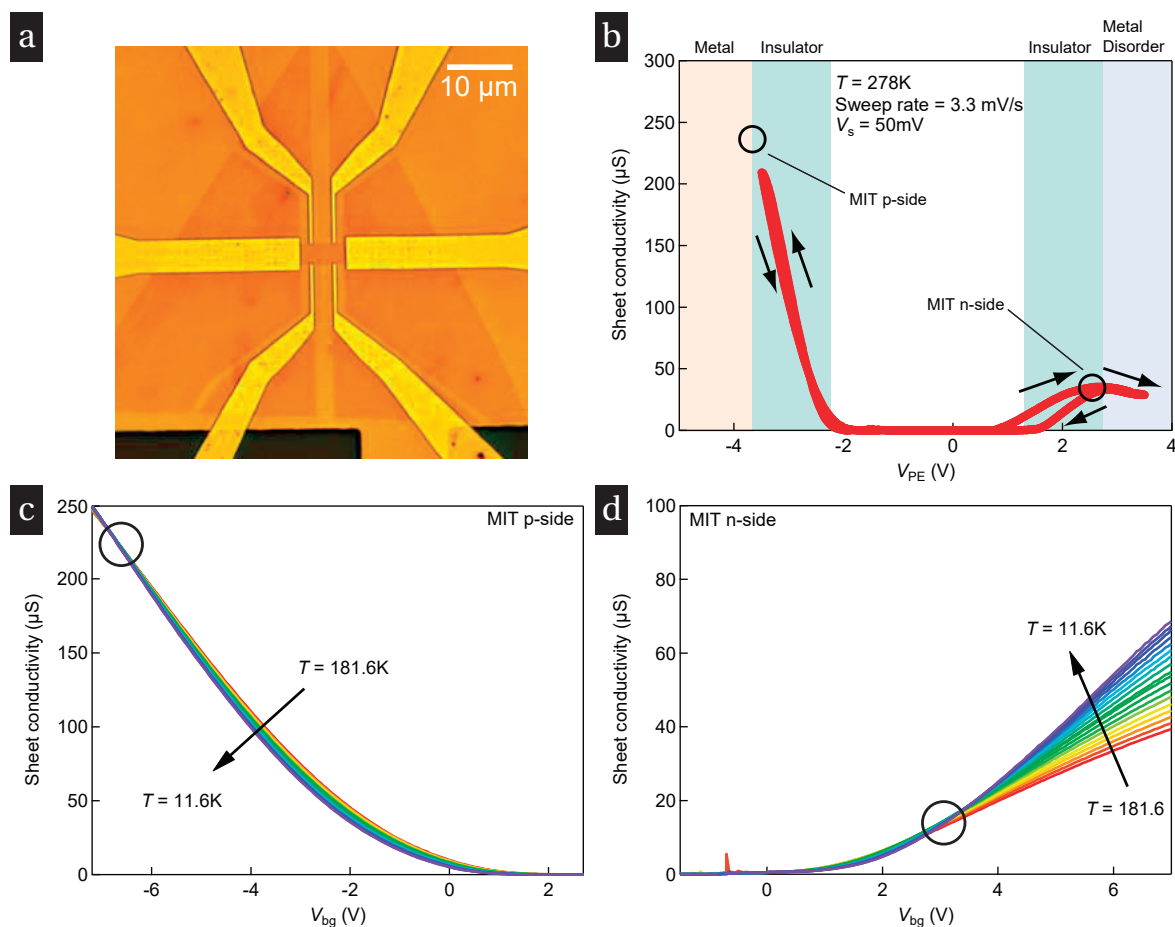


Figure 7.5 – Ambipolar insulator to metal transition in monolayer WSe₂. (a) Optical image of monolayer CVD WSe₂ device in Hall-bar geometry. (b) EDLT characterization at 278K with regions of interest marked by color code. (c) MIT on p-side after freezing of electrolyte. (d) MIT on n-side after freezing of electrolyte.

Section 2.3.2 on band structure of monolayer TMDCs) was found in recent experiments on high-mobility samples does not contradict this hypothesis [103], since those samples were studied at lower carrier densities (below 10^{13} cm^{-2}), while the trap tail is expected to have lower extension due to the sample preparation procedure (encapsulation in h-BN).

We extract four-contact field-effect mobility μ_{FE} from the data on Figure 7.5c, d and plot it on Figure 7.6. Low temperature mobility on the p-side is almost temperature independent, stays around the value of $130 \text{ cm}^2 \cdot \text{V}^{-1} \cdot \text{s}^{-1}$ at low temperature (red markers on Figure 7.6a) and increases with increasing doping (Figure 7.6a from black markers to red markers), while n-type mobility is lower, is temperature dependent and is on the order of $40 \text{ cm}^2 \cdot \text{V}^{-1} \cdot \text{s}^{-1}$. To put these measurements in line with our estimation of electrolyte capacitance, we estimate mobility at 278K from curves shown on Figure 7.5b and find values of $\mu_{\text{FE}}^h = 60 \text{ cm}^2 \cdot \text{V}^{-1} \cdot \text{s}^{-1}$ and $\mu_{\text{FE}}^e = 10 \text{ cm}^2 \cdot \text{V}^{-1} \cdot \text{s}^{-1}$ in good agreement with the data, shown on Figure 7.6.

7.3. Results: Band-like transport and ambipolar insulator to metal transition in CVD grown WSe₂ and MoSe₂

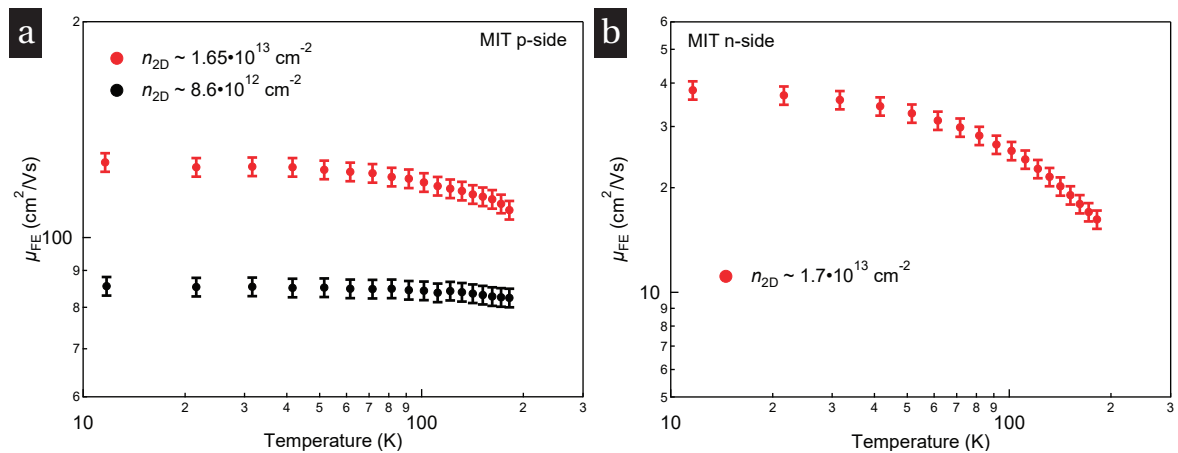


Figure 7.6 – Temperature dependence of field effect mobility in monolayer WSe₂. (a) Hole side. (b) Electron side.

7.3.3 Ambipolar insulator to metal transition in CVD grown MoSe₂

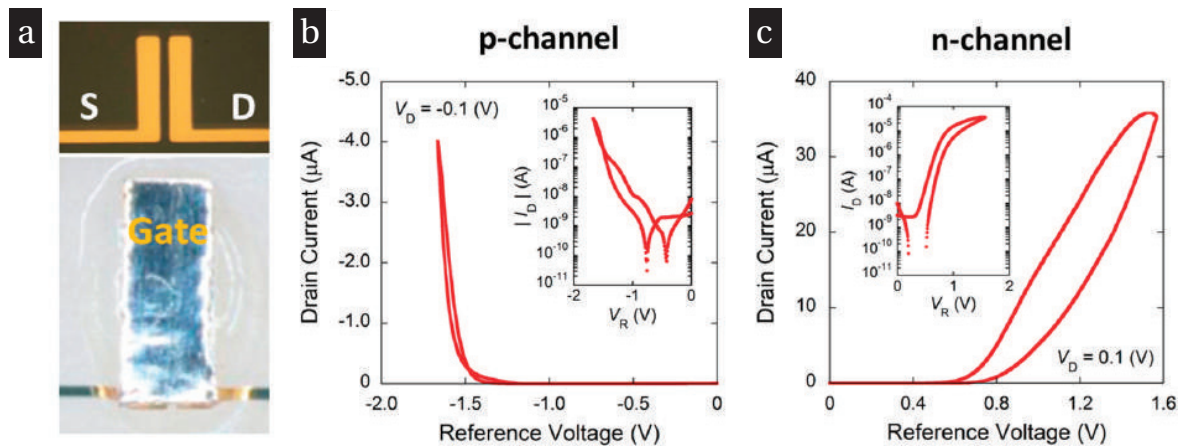


Figure 7.7 – EDLT based on monolayer MoSe₂. (a) Optical image of the device before (top panel) and after (bottom panel) ion gel deposition. (b) p-side conduction, drain current as a function of reference voltage. Inset - same plot in log scale. (c) n-side conduction, drain current as a function of reference voltage. Inset - same plot in log scale. Adapted with permission from Y.-H. Chang, W. Zhang, Y. Zhu, Y. Han, J. Pu, J.-K. Chang, W.-T. Hsu, J.-K. Huang, C.-L. Hsu, M.-H. Chiu, T. Takenobu, H. Li, C.-I. Wu, W.-H. Chang, A.T.S. Wee, and L.-J. Li, "Monolayer MoSe₂ Grown by Chemical Vapor Deposition for Fast Photodetection", *ACS Nano*, vol. 8, no. 8, pp. 8582-8590, © (2014) American Chemical Society.

For monolayer MoSe₂ the current state of the art samples mostly exhibit n-type conductivity [197]. There are reports, where both branches of conductance were observed [150] on macroscopic monolayer samples. It can be seen from Figure 7.7, that conductivity on p-side is lower than on n-side with no apparent saturation (Figure 7.7b), the authors also report lower mobility on p-side than on n-side.

Chapter 7. High-quality synthetic 2D transition metal dichalcogenide semiconductors

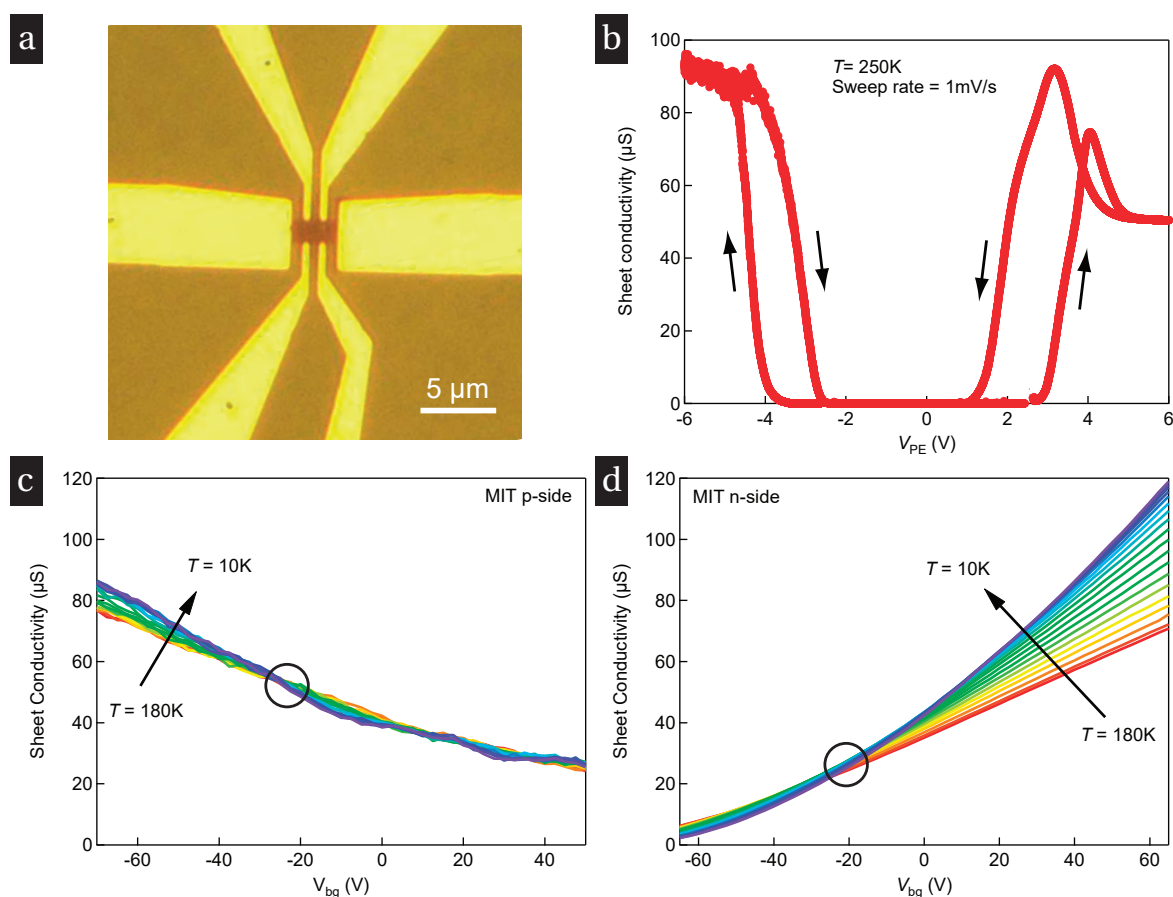


Figure 7.8 – Ambipolar insulator to metal transition in monolayer MoSe₂. (a) Optical image of monolayer CVD MoSe₂ device in the Hall-bar geometry. (b) EDLT characterization at 250K with. (c) MIT on p-side after freezing of electrolyte. (d) MIT on n-side after freezing of electrolyte.

We performed similar type of measurements as in case of monolayer WSe₂ (see Section 7.3.2), choosing a lower temperature and wider V_{PE} range for MoSe₂, because reaching valence band was more difficult in the case of this material. Again, for both sides we were able to achieve band-like transport and transition from insulator to metal. Our sample is based on a monolayer MoSe₂ transferred onto a Si/SiO₂ substrate. We measured two devices, which provided consistent results. One of the samples is shown on Figure 7.8a. On Figure 7.8b overview of the measurement results is shown. Although we chose a lower temperature and a higher voltage range, we were able to perform multiple cooling cycles with no degradation observed. Hysteresis is present on both electron and hole side with saturation on hole sides and a typical dome-like shape on the electron side.

We freeze the electrolyte on electron and holes side near the band edge and perform mobility measurements with the back gate. We again observe insulator to metal transition with increasing doping on both sides (Figure 7.8c, d). In this case, mobility on electron

7.3. Results: Band-like transport and ambipolar insulator to metal transition in CVD grown WSe₂ and MoSe₂

side is higher (Figure 7.9). The transition can also be seen looking for example at mobility values as a function of back gate voltage V_{bg} (Figure 7.9b). On the hole side, we observe conductivity fluctuations, which might indicate increased disorder on the valence band edge, similar to observed in early reports on WS₂ [106]. The hole mobility is almost temperature independent and stays on the level around $60 \text{ cm}^2 \cdot \text{V}^{-1} \cdot \text{s}^{-1}$.

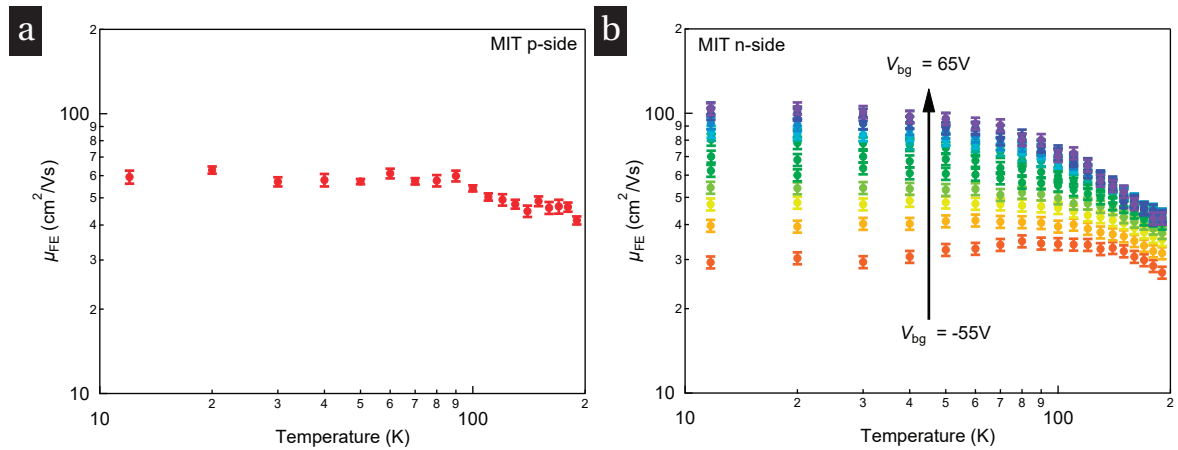


Figure 7.9 – Temperature dependence of field effect mobility in monolayer MoSe₂. (a) Hole side. (b) Electron side.

7.3.4 Contact resistance in MoSe₂

Monolayer MoSe₂ in CVD form is a much less studied material than for example CVD MoS₂. We checked contact resistances in our MoSe₂ EDLT to estimate the quality of carrier injection. It is important especially at low temperatures, where contact resistances can impact mobility measurements [60].

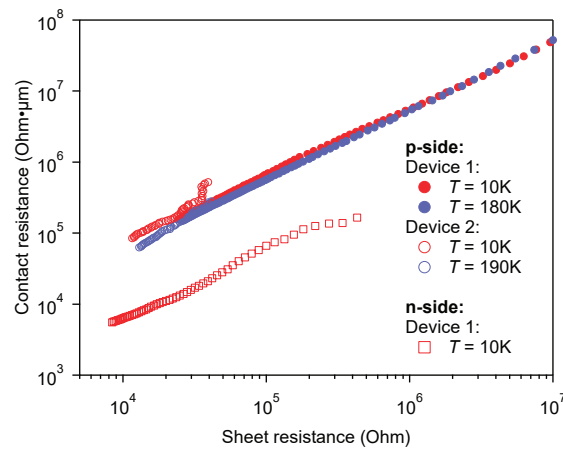


Figure 7.10 – Contact resistance as a function of sheet resistance for n- and p-type conductivity in CVD-grown monolayer MoSe₂.

Chapter 7. High-quality synthetic 2D transition metal dichalcogenide semiconductors

We find contact resistances for n-side to be systematically lower than for the p-side, reaching values of $R_c^e = 5\text{k}\Omega \cdot \mu\text{m}$ for 10 k Ω sheet resistance, superior to what has been reported in monolayer WSe₂ at low temperatures [58]. For hole injection, however, contact resistances are higher. For the same sheet resistance value (10 k Ω), we observe a low temperature contact resistance of $R_c^h = 85\text{k}\Omega \cdot \mu\text{m}$. Such asymmetry in R_c might indicate Fermi level pinning (FLP) at the conduction band edge of MoSe₂.

MoS₂ is known to have the Fermi level pinned at the conduction band edge [60, 198, 199, 200, 201]. Some calculations suggest that selenide-based TMDCs should have more freedom in Fermi-level modulation due to higher formation energy of vacancies, which might be responsible for Fermi-level pinning [202]. Recent advances in aberration-corrected microscopy revealed [203, 204, 205] the presence of grain boundaries and defects in synthetic MoSe₂. We do not expect grain boundary formation in our triangular MoSe₂ monolayer domains. Thickness variation was not revealed by spectroscopy techniques neither. It is thus reasonable to propose vacancies as the reason for n-type doping of our samples and FLP near conduction band edge. Careful correlation between transport and structural properties of this material is the subject of future work.

7.3.5 Disorder in MoSe₂ EDLT

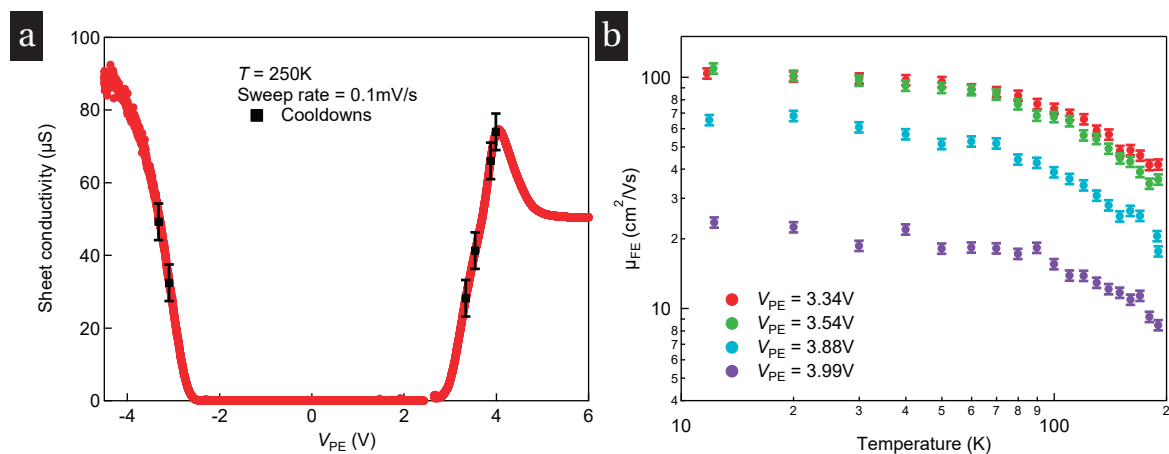


Figure 7.11 – Electrostatic disorder effect on monolayer MoSe₂. (a) Ambipolar transport at 250K, black markers indicate points, where cooling cycles were performed. (b) Four-probe field-effect mobility as a function of temperature for different values of V_{PE} .

Finally, we discuss the effect of disorder on the electron side in monolayer MoSe₂ to complete the picture of the impact electrostatic disorder has on CB of TMDCs. On Figure 7.11 we plot the ambipolar curve of our MoSe₂ (only one direction of sweep is shown for simplicity) with black markers, indicating points, where cooling cycles were performed. On Figure 7.11b we plot temperature dependence of mobility μ_{FE} . Increasing the electrolyte

voltage, we can quench the low temperature mobility in CB from $110 \text{ cm}^2 \cdot \text{V}^{-1} \cdot \text{s}^{-1}$ to $25 \text{ cm}^2 \cdot \text{V}^{-1} \cdot \text{s}^{-1}$. On the hole side we did not observe such a mobility modulation.

7.3.6 Conclusions

In this section we demonstrated devices which exhibit band-like transport on both electron and hole side. We employed EDLT technique to achieve ambipolar transport and low contact resistances in monolayer MoSe_2 and WSe_2 . Our study shed light on all pros and cons of the studied devices and can lead to an improvement of both the material quality and device design. From the material point of view, this is the first demonstration of clear ambipolar band-like transport in synthetic monolayers of TMDCs, indicating high quality of the material and low density of trap states at the band edge.

We measured transport properties and provided an overview of different transport mechanisms. Although EDLT has a drawback of electrostatic disorder, widely discussed in this thesis and emphasized in this Chapter, it has a potential to be a platform for a variety of fundamental studies [40, 49, 55]. Combining EDLTs with one of the approaches of "clean" sample fabrication one can achieve for example high mobilities and doping levels or electric fields in the same device. One of strategies, which could be used, is protection of our material with mono- or bilayer h-BN flakes, preserving clean interface. This strategy appears to be very promising in the case of STO [87]. Another option is to employ manipulation of carrier injection in the contact region, while keeping the sample channel encapsulated in h-BN layers and use of solid gates [206] for carrier density modulation.

7.4 Conclusion & Outlook

In this chapter we provided a general picture on different approaches to growth of 2D semiconductors and on device design. The points, which we demonstrated, are summarized below:

- Monolayer MoS_2 grown by the combination of solid (MoO_3) and gas phase (H_2S), which adds flexibility to the process, discussed in Chapter 6. Our material exhibits mobility and defect density similar to the state of the art devices based on CVD and exfoliated material.
- Temperature dependent measurements and ambipolar insulator to metal transition in monolayer MoSe_2 and WSe_2 grown by CVD method.
- Ambipolar band-like transport achieved indicates high quality of our material.

Chapter 7. High-quality synthetic 2D transition metal dichalcogenide semiconductors

- Contact resistances to both CB and VB of monolayer MoSe₂ were studied, also at low temperatures. We demonstrated asymmetry of carrier injection and we pointed towards possible mechanisms beyond this.
- Finally, we expanded our discussion on disorder effect on conductivity in CB of monolayer TMDCs, which provided complementary information to Chapter 5.

CVD is a promising technique for scalable production of large-area samples. We discussed in this Chapter different types of material in monolayer form - MoS₂, MoSe₂ and WSe₂, which have promising properties and which are comparable with state of the art samples in the scientific community. We also demonstrated strategies towards both p- and n-type transistors. The sapphire substrate, on which all growth was performed, is actively used in industrial applications. Sapphire/TMDC stack can act as a platform for a variety of electronic or optoelectronic devices. Before transfer to other substrates will be possible on production level, transfer of TMDC should be significantly improved. In case successful methods for large area transfer will be developed, we foresee applications in flexible circuits, where TMDCs can significantly outperform the organic electronics.

8 Conclusion

This thesis discussed a variety of 2D materials (MoS_2 , MoSe_2 , WS_2 , WSe_2 , ReS_2) with the focus on two important performance limiting factors - structural disorder (grain boundaries in CVD MoS_2) and electrostatic disorder (a striking example being monolayer ReS_2 with the possibility of complete conductivity suppression by means of disorder modulation). These two factors can dramatically change the performance of devices based on these materials and impact such figures of merit as mobility, subthreshold swing and optical response of transistors or optoelectronic devices. The summary of this thesis is below:

- We demonstrate the first comprehensive transport study of monolayer WS_2 varying carrier density and temperature. Our study demonstrates high quality of material and further roots towards device optimization.
- We perform the first study of EDLT based on ReS_2 . We show that disorder can lead to dramatic modulation of mobility and change transport regimes depending on disorder strength. We develop a theoretical model, which allows us to explain our findings. We expand discussion of disorder effect on CB of TMDCs on other materials, in particular, MoS_2 and MoSe_2 .
- We engineer grain boundaries performing first epitaxial CVD growth of MoS_2 . We carefully prepare sapphire substrates to achieve atomically smooth interfaces, where vdW epitaxy is possible. Large area material shows transport properties similar to single grains of MoS_2 .
- We explore different CVD-grown monolayers of TMDCs. The signature of high electrical quality of our material is the observation of ambipolar insulator to metal transition in monolayers of MoSe_2 and WSe_2 .

The discussed topics are among many intensively investigated in 2D materials community. We believe that our conclusions regarding grain boundaries and electrostatic

Chapter 8. Conclusion

disorder are universal for many 2D materials. Semiconducting monolayer is a pure interface exposed to multiple sources of scattering - both intrinsic (such as grain boundaries and point defects) and extrinsic (such as potential variation). 2D materials are proposed for multiple electronic and optoelectronic applications, as well as new device concepts based on spin and valley physics are foreseen. Information regarding disorder can help to optimize devices of any of the abovementioned types.

Abbreviations & Symbols

AFM	Atomic-force-microscopy
ALD	Atomic-layer-deposition
Å	Ångström
Au	Gold
B	Magnetic field
BF	Bright-field TEM imaging
h-BN	Hexagonal boron nitride
BP	Black phosphorous
c	Speed of light
°C	Celsius
C_{bg}	Back-gate capacitance
$C_{EMIM-TFSI}$	Capacitance of [EMIM][TFSI] polymer electrolyte
CB	Conduction band
CMi	Center of micronanotechnology
CMOS	Complementary metal-oxide-semiconductor
CPD	Contact potential difference
C_{tg}	Top-gate capacitance
CVD	Chemical Vapor Deposition
Cr	Chromium
DF	Dark-field TEM imaging
DP	Diffraction pattern
e	Elementary charge
e-beam	Electron-beam
E_C	Energy conduction band
E_g	Band gap
[EMIM]-[TFSI]	1-Ethyl-3-methylimidazolium bis(trifluoromethylsulfonyl)imide
E_V	Energy valence band
ϵ_0	Permittivity of free space
ϵ_r	Relative permittivity
ϵ_s	Permittivity of semiconductor

Abbreviations & Symbols

f	Frequency
F	Noise factor
Fe	Iron
FET	Field-effect transistor
FF	Filling factor
FFT	Fast Fourier transform
h	Planck's constant
H	Hydrogen
HE	Hall effect
I_{ds}	Drain-source current
i.e.	id est or "that is"
IL	Ionic liquid
IPA	Isopropyl alcohol
I_{PE}	Leakage current through polymer electrolyte
ITRS	International Technology Roadmap for Semiconductors
K	Kelvin
L_{ch}	Channel length
LED	Light Emitting Diodes
$LiClO_4$	Lithium perchlorate
M	Transition-metal atom
MBE	Molecular beam epitaxy
MIBK	Methyl isobutyl ketone
min.	minute
MMA	Methyl methacrylate
Mo	Molybdenum
MoS_2	Molybdenum disulfide
$MoSe_2$	Molybdenum diselenide
μ	Mobility
μ_{2C}	Two-contact field-effect mobility
μ_{FE}	Field-effect mobility
μ_{Hall}	Hall mobility
N_2	Nitrogen
Ni	Nickel
O	Oxygen
Pd	Paladium
PE	Polymer electrolyte
PL	Photoluminescence
PMMA	Poly(methyl methacrylate)
Pt	Platinum

q	Elementary charge
R	Resistance
Re	Rhenium
Ref.	Reference
ReS ₂	Rhenium disulphide
rpm.	Rotations per minute
RT	Room temperature
s	second
S	Sulfur
SAED	Selected-area electron diffraction
Se	Selenium
Si	Silicon
SO	Spin-orbit coupling
SS	Subthreshold swing
STEM	Scanning transmission electron microscopy
Ta	Tantalum
Te	Tellurium
TEM	Transmission electron microscopy
Ti	Titanium
TMDC	Transition metal dichalcogenides
UHV	Ultra-High Vacuum
VB	Valence band
V_{bg}	Back-gate potential
V_{ds}	Drain-source bias
V_g	Gate potential
V_{PE}	Polymer electrolyte voltage
V_s	Source bias
VHE	valley Hall effect
V_{tg}	Top-gate potential
V_{th}	Threshold voltage
W	Tungsten
W_{ch}	Channel width
WS ₂	Tungsten disulfide
WSe ₂	Tungsten diselenide
wt. %	weight %
X	Chalcogen atom
2D	Two-dimensional
3D	Three-dimensional

Bibliography

- [1] K. S. Novoselov, A. K. Geim, S. V. Morozov, D. Jiang, Y. Zhang, S. V. Dubonos, I. V. Grigorieva, and A. A. Firsov, "Electric field effect in atomically thin carbon films," *Science*, vol. 306, no. 5696, pp. 666–669, 2004.
- [2] K. S. Novoselov, A. K. Geim, S. V. Morozov, D. Jiang, M. I. Katsnelson, I. V. Grigorieva, S. V. Dubonos, and A. A. Firsov, "Two-dimensional gas of massless Dirac fermions in graphene," *Nature*, vol. 438, no. 7065, pp. 197–200, 2005.
- [3] A. K. Geim and K. S. Novoselov, "The rise of graphene," *Nature Materials*, vol. 6, no. 3, pp. 183–191, 2007.
- [4] J. Wilson and A. Yoffe, "The transition metal dichalcogenides discussion and interpretation of the observed optical, electrical and structural properties," *Advances in Physics*, vol. 18, no. 73, pp. 193–335, 1969.
- [5] B. Radisavljevic, A. Radenovic, J. Brivio, V. Giacometti, and A. Kis, "Single-layer MoS₂ transistors," *Nature Nanotechnology*, vol. 6, no. 3, pp. 147–150, 2011.
- [6] T. Roy, M. Tosun, J. S. Kang, A. B. Sachid, S. B. Desai, M. Hettick, C. C. Hu, and A. Javey, "Field-effect transistors built from all two-dimensional material components," *ACS Nano*, vol. 8, no. 6, pp. 6259–6264, 2014.
- [7] D. Akinwande, N. Petrone, and J. Hone, "Two-dimensional flexible nanoelectronics," *Nature Communications*, vol. 5, 2014.
- [8] S. Bertolazzi, J. Brivio, and A. Kis, "Stretching and breaking of ultrathin MoS₂," *ACS Nano*, vol. 5, no. 12, pp. 9703–9709, 2011.
- [9] X. Xu, W. Yao, D. Xiao, and T. F. Heinz, "Spin and pseudospins in layered transition metal dichalcogenides," *Nature Physics*, vol. 10, no. 5, pp. 343–350, 2014.
- [10] D. Dumcenco, D. Ovchinnikov, K. Marinov, P. Lazić, M. Gibertini, N. Marzari, O. L. Sanchez, Y.-C. Kung, D. Krasnozhon, M.-W. Chen, S. Bertolazzi, P. Gillet, A. Fontcuberta i Morral, A. Radenovic, and A. Kis, "Large-area epitaxial monolayer MoS₂," *ACS Nano*, vol. 9, no. 4, pp. 4611–4620, 2015.

Bibliography

- [11] D. Dumcenco, D. Ovchinnikov, O. L. Sanchez, P. Gillet, D. T. L. Alexander, Sorin Lazar, A. Radenovic, and A. Kis, "Large-area MoS₂ grown using H₂S as the sulphur source," *2D Materials*, vol. 2, no. 4, p. 044005, 2015.
- [12] D. Ovchinnikov, A. Allain, Y.-S. Huang, D. Dumcenco, and A. Kis, "Electrical transport properties of single-layer WS₂," *ACS Nano*, vol. 8, no. 8, pp. 8174–8181, 2014.
- [13] D. Ovchinnikov, F. Gargiulo, A. Allain, D. J. Pasquier, D. Dumcenco, C.-H. Ho, O. V. Yazyev, and A. Kis, "Disorder engineering and conductivity dome in ReS₂ with electrolyte gating," *Nature Communications*, vol. 7, p. 12391, 2016.
- [14] L. Wang, I. Meric, P. Y. Huang, Q. Gao, Y. Gao, H. Tran, T. Taniguchi, K. Watanabe, L. M. Campos, D. A. Muller, J. Guo, P. Kim, J. Hone, K. L. Shepard, and C. R. Dean, "One-dimensional electrical contact to a two-dimensional material," *Science*, vol. 342, no. 6158, pp. 614–617, 2013.
- [15] L. Wang, Y. Gao, B. Wen, Z. Han, T. Taniguchi, K. Watanabe, M. Koshino, J. Hone, and C. R. Dean, "Evidence for a fractional fractal quantum Hall effect in graphene superlattices," *Science*, vol. 350, no. 6265, pp. 1231–1234, 2015.
- [16] X. Cui, G.-H. Lee, Y. D. Kim, G. Arefe, P. Y. Huang, C.-H. Lee, D. A. Chenet, X. Zhang, L. Wang, F. Ye, F. Pizzocchero, B. S. Jessen, K. Watanabe, T. Taniguchi, D. A. Muller, T. Low, P. Kim, and J. Hone, "Multi-terminal transport measurements of MoS₂ using a van der Waals heterostructure device platform," *Nature Nanotechnology*, vol. 10, no. 6, pp. 534–540, 2015.
- [17] R. Suzuki, M. Sakano, Y. J. Zhang, R. Akashi, D. Morikawa, A. Harasawa, K. Yaji, K. Kuroda, K. Miyamoto, T. Okuda, K. Ishizaka, R. Arita, and Y. Iwasa, "Valley-dependent spin polarization in bulk MoS₂ with broken inversion symmetry," *Nature Nanotechnology*, vol. 9, no. 8, pp. 611–617, 2014.
- [18] K. F. Mak, C. Lee, J. Hone, J. Shan, and T. F. Heinz, "Atomically thin MoS₂: A new direct-gap semiconductor," *Physical Review Letters*, vol. 105, no. 13, p. 136805, 2010.
- [19] A. Splendiani, L. Sun, Y. Zhang, T. Li, J. Kim, C.-Y. Chim, G. Galli, and F. Wang, "Emerging photoluminescence in monolayer MoS₂," *Nano Letters*, vol. 10, no. 4, pp. 1271–1275, 2010.
- [20] O. V. Yazyev and A. Kis, "MoS₂ and semiconductors in the flatland," *Materials Today*, vol. 18, no. 1, p. 30, 2015.
- [21] K. F. Mak, K. He, C. Lee, G. H. Lee, J. Hone, T. F. Heinz, and J. Shan, "Tightly bound trions in monolayer MoS₂," *Nature Materials*, vol. 12, no. 3, pp. 207–211, 2013.

- [22] K. F. Mak, K. He, J. Shan, and T. F. Heinz, "Control of valley polarization in monolayer MoS₂ by optical helicity," *Nature Nanotechnology*, vol. 7, no. 8, pp. 494–498, 2012.
- [23] S. Tongay, H. Sahin, C. Ko, A. Luce, W. Fan, K. Liu, J. Zhou, Y.-S. Huang, C.-H. Ho, J. Yan, D. F. Ogletree, S. Aloni, J. Ji, S. Li, J. Li, F. M. Peeters, and J. Wu, "Monolayer behaviour in bulk ReS₂ due to electronic and vibrational decoupling," *Nature Communications*, vol. 5, 2014.
- [24] O. B. Aslan, D. A. Chenet, A. M. van der Zande, J. C. Hone, and T. F. Heinz, "Linearly polarized excitons in single- and few-layer ReS₂ crystals," *ACS Photonics*, vol. 3, no. 1, pp. 96–101, 2016.
- [25] I. Gutiérrez-Lezama, B. A. Reddy, N. Ubrig, and A. F. Morpurgo, "Electroluminescence from indirect band gap semiconductor ReS₂," *2D Mater.*, vol. 3, no. 4, p. 045016, 2016.
- [26] D. A. Chenet, O. B. Aslan, P. Y. Huang, C. Fan, A. M. van der Zande, T. F. Heinz, and J. C. Hone, "In-plane anisotropy in mono- and few-layer ReS₂ probed by Raman spectroscopy and scanning transmission electron microscopy," *Nano Letters*, 2015.
- [27] F. J. Ohkawa and Y. Uemura, "Theory of valley splitting in an n-channel (100) inversion layer of Si. Formulation by extended zone effective mass theory," *Journal of the Physical Society of Japan*, vol. 43, no. 3, pp. 907–916, 1977.
- [28] L. J. Sham, S. J. Allen, A. Kamgar, and D. C. Tsui, "Valley-valley splitting in inversion layers on a high-index surface of silicon," *Physical Review Letters*, vol. 40, no. 7, pp. 472–475, 1978.
- [29] D. Xiao, G.-B. Liu, W. Feng, X. Xu, and W. Yao, "Coupled spin and valley physics in monolayers of MoS₂ and other group-VI dichalcogenides," *Physical Review Letters*, vol. 108, no. 19, p. 196802, 2012.
- [30] J. R. Schaibley, H. Yu, G. Clark, P. Rivera, J. S. Ross, K. L. Seyler, W. Yao, and X. Xu, "Valleytronics in 2D materials," *Nature Reviews Materials*, vol. 1, p. 16055, 2016.
- [31] I. Guillaumon, H. Suderow, S. Vieira, L. Cario, P. Diener, and P. Rodière, "Superconducting density of states and vortex cores of 2H-NbS₂," *Physical Review Letters*, vol. 101, no. 16, 2008.
- [32] D. C. Freitas, P. Rodière, M. R. Osorio, E. Navarro-Moratalla, N. M. Nemes, V. G. Tissen, L. Cario, E. Coronado, M. García-Hernández, S. Vieira, M. Núñez-Regueiro, and H. Suderow, "Strong enhancement of superconductivity at high pressures within the charge-density-wave states of 2H-TaS₂ and 2H-TaSe₂," *Physical Review B*, vol. 93, no. 18, 2016. 00000.

Bibliography

- [33] S. Nagata, T. Aochi, T. Abe, S. Ebisu, T. Hagino, Y. Seki, and K. Tsutsumi, “Superconductivity in the layered compound 2H-TaS₂,” *Journal of Physics and Chemistry of Solids*, vol. 53, no. 10, p. 1263, 1992.
- [34] E. Revolinsky, G. A. Spiering, and D. J. Beerntsen, “Superconductivity in the niobium-selenium system,” *Journal of Physics and Chemistry of Solids*, vol. 26, no. 6, p. 1034, 1965.
- [35] T. Valla, A. V. Fedorov, P. D. Johnson, J. Xue, K. E. Smith, and F. J. DiSalvo, “Charge-density-wave-induced modifications to the quasiparticle self-energy in 2H-TaSe₂,” *Physical Review Letters*, vol. 85, no. 22, p. 4762, 2000.
- [36] M. M. Ugeda, A. J. Bradley, Y. Zhang, S. Onishi, Y. Chen, W. Ruan, C. Ojeda-Aristizabal, H. Ryu, M. T. Edmonds, H.-Z. Tsai, A. Riss, S.-K. Mo, D. Lee, A. Zettl, Z. Hussain, Z.-X. Shen, and M. F. Crommie, “Characterization of collective ground states in single-layer NbSe₂,” *Nature Physics*, vol. 12, no. 1, 2016.
- [37] J. M. Kosterlitz and D. J. Thouless, “Ordering, metastability and phase transitions in two-dimensional systems,” *Journal of Physics C: Solid State Physics*, vol. 6, no. 7, p. 3719, 1973.
- [38] X. Xi, Z. Wang, W. Zhao, J.-H. Park, K. T. Law, H. Berger, L. Forró, J. Shan, and K. F. Mak, “Ising pairing in superconducting NbSe₂ atomic layers,” *Nature Physics*, vol. 12, no. 2, pp. 139–143, 2016.
- [39] W.-Y. He, B. T. Zhou, J. J. He, T. Zhang, and K. T. Law, “Nodal topological superconductivity in monolayer NbSe₂,” *arXiv:1604.02867 [cond-mat]*, 2016.
- [40] J. T. Ye, Y. J. Zhang, R. Akashi, M. S. Bahramy, R. Arita, and Y. Iwasa, “Superconducting dome in a gate-tuned band insulator,” *Science*, vol. 338, no. 6111, pp. 1193–1196, 2012.
- [41] W. Shi, J. Ye, Y. Zhang, R. Suzuki, M. Yoshida, J. Miyazaki, N. Inoue, Y. Saito, and Y. Iwasa, “Superconductivity series in transition metal dichalcogenides by ionic gating,” *Sci. Rep.*, vol. 5, 2015.
- [42] S. Jo, D. Costanzo, H. Berger, and A. F. Morpurgo, “Electrostatically induced superconductivity at the surface of WS₂,” *Nano Letters*, vol. 15, no. 2, pp. 1197–1202, 2015.
- [43] D. Costanzo, S. Jo, H. Berger, and A. F. Morpurgo, “Gate-induced superconductivity in atomically thin MoS₂ crystals,” *Nature Nanotechnology*, vol. 11, pp. 339–344, 2016.

- [44] J. M. Lu, O. Zheliuk, I. Leermakers, N. F. Q. Yuan, U. Zeitler, K. T. Law, and J. T. Ye, "Evidence for two-dimensional Ising superconductivity in gated MoS₂," *Science*, vol. 350, no. 6266, pp. 1353–1357, 2015.
- [45] Y. Saito, Y. Nakamura, M. S. Bahramy, Y. Kohama, J. Ye, Y. Kasahara, Y. Nakagawa, M. Onga, M. Tokunaga, T. Nojima, Y. Yanase, and Y. Iwasa, "Superconductivity protected by spin-valley locking in ion-gated MoS₂," *Nature Physics*, vol. 12, pp. 144–149, 2016.
- [46] Y. Saito, T. Nojima, and Y. Iwasa, "Highly crystalline 2D superconductors," *Nature Reviews Materials*, vol. 2, p. 16094, 2016.
- [47] S. Bertolazzi, D. Krasnozhan, and A. Kis, "Nonvolatile memory cells based on MoS₂/graphene heterostructures," *ACS Nano*, vol. 7, pp. 3246–3252, 2013.
- [48] V. Podzorov, M. E. Gershenson, C. Kloc, R. Zeis, and E. Bucher, "High-mobility field-effect transistors based on transition metal dichalcogenides," *Applied Physics Letters*, vol. 84, no. 17, pp. 3301–3303, 2004.
- [49] H. Yuan, M. S. Bahramy, K. Morimoto, S. Wu, K. Nomura, B.-J. Yang, H. Shimotani, R. Suzuki, M. Toh, C. Kloc, X. Xu, R. Arita, N. Nagaosa, and Y. Iwasa, "Zeeman-type spin splitting controlled by an electric field," *Nature Physics*, vol. 9, no. 9, pp. 563–569, 2013.
- [50] B. Radisavljevic, M. B. Whitwick, and A. Kis, "Small-signal amplifier based on single-layer MoS₂," *Applied Physics Letters*, vol. 101, p. 043103, 2012.
- [51] D. Krasnozhan, D. Lembke, C. Nyffeler, Y. Leblebici, and A. Kis, "MoS₂ transistors operating at Gigahertz frequencies," *Nano Letters*, vol. 14, no. 10, pp. 5905–5911, 2014.
- [52] D. Krasnozhan, S. Dutta, C. Nyffeler, Y. Leblebici, and A. Kis, "High-frequency, scaled MoS₂ transistors," in *2015 IEEE International Electron Devices Meeting (IEDM)*, pp. 27.4.1–27.4.4, 2015.
- [53] O. Lopez-Sanchez, D. Lembke, M. Kayci, A. Radenovic, and A. Kis, "Ultrasensitive photodetectors based on monolayer MoS₂," *Nature Nanotechnology*, vol. 8, no. 7, pp. 497–501, 2013.
- [54] O. Lopez-Sanchez, E. A. Llado, V. Koman, A. F. I. Morral, A. Radenovic, and A. Kis, "Light generation and harvesting in a van der Waals heterostructure," *ACS Nano*, vol. 8, no. 3, pp. 3042–3048, 2014.

Bibliography

- [55] Y. J. Zhang, T. Oka, R. Suzuki, J. T. Ye, and Y. Iwasa, "Electrically switchable chiral light-emitting transistor," *Science*, vol. 344, no. 6185, pp. 725–728, 2014.
- [56] D. Vella, D. Ovchinnikov, N. Martino, V. Vega-Mayoral, D. Dumcenco, Y.-C. Kung, M.-R. Antognazza, A. Kis, G. Lanzani, D Mihailovic, and C. Gadermaier, "Unconventional electroabsorption in monolayer MoS₂," *2D Materials*, vol. 4, no. 2, p. 021005, 2017.
- [57] R. Kappera, D. Voiry, S. E. Yalcin, B. Branch, G. Gupta, A. D. Mohite, and M. Chhowalla, "Phase-engineered low-resistance contacts for ultrathin MoS₂ transistors," *Nature Materials*, vol. 13, no. 12, pp. 1128–1134, 2014.
- [58] A. Allain and A. Kis, "Electron and hole mobilities in single-layer WSe₂," *ACS Nano*, vol. 8, no. 7, pp. 7180–7185, 2014.
- [59] H. Fang, S. Chuang, T. C. Chang, K. Takei, T. Takahashi, and A. Javey, "High-performance single layered WSe₂ p-FETs with chemically doped contacts," *Nano Letters*, vol. 12, no. 7, pp. 3788–3792, 2012.
- [60] A. Allain, J. Kang, K. Banerjee, and A. Kis, "Electrical contacts to two-dimensional semiconductors," *Nature Materials*, vol. 14, no. 12, pp. 1195–1205, 2015.
- [61] Y.-S. Huang, "Preparation, electrical and modulation optical properties of 2H-MoSe₂," *Chinese Journal of Physics*, vol. 22, no. 4, pp. 43–53, 1984.
- [62] H. Schäfer, *Chemical transport reactions*. New York: Academic Press, 1964.
- [63] M. B. Dines, "Lithium intercalation via n-Butyllithium of the layered transition metal dichalcogenides," *Materials Research Bulletin*, vol. 10, no. 4, pp. 287–291, 1975.
- [64] J. N. Coleman, M. Lotya, A. O'Neill, S. D. Bergin, P. J. King, U. Khan, K. Young, A. Gaucher, S. De, R. J. Smith, I. V. Shvets, S. K. Arora, G. Stanton, H.-Y. Kim, K. Lee, G. T. Kim, G. S. Duesberg, T. Hallam, J. J. Boland, J. J. Wang, J. F. Donegan, J. C. Grunlan, G. Moriarty, A. Shmeliov, R. J. Nicholls, J. M. Perkins, E. M. Grieveson, K. Theuwissen, D. W. McComb, P. D. Nellist, and V. Nicolosi, "Two-dimensional nanosheets produced by liquid exfoliation of layered materials," *Science*, vol. 331, no. 6017, pp. 568–571, 2011.
- [65] V. Nicolosi, M. Chhowalla, M. G. Kanatzidis, M. S. Strano, and J. N. Coleman, "Liquid exfoliation of layered materials," *Science*, vol. 340, no. 6139, p. 1226419, 2013.
- [66] G. Eda, H. Yamaguchi, D. Voiry, T. Fujita, M. Chen, and M. Chhowalla, "Photoluminescence from chemically exfoliated MoS₂," *Nano Letters*, vol. 11, no. 12, pp. 5111–5116, 2011.

- [67] A. Koma and K. Yoshimura, "Ultrasharp interfaces grown with van der Waals epitaxy," *Surface Science*, vol. 174, no. 1–3, pp. 556–560, 1986.
- [68] A. Koma, "Van der Waals epitaxy for highly lattice-mismatched systems," *Journal of Crystal Growth*, vol. 201–202, pp. 236–241, 1999.
- [69] O. Lehtinen, H.-P. Komsa, A. Pulkin, M. B. Whitwick, M.-W. Chen, T. Lehnert, M. J. Mohn, O. V. Yazyev, A. Kis, U. Kaiser, and A. V. Krasheninnikov, "Atomic scale microstructure and properties of Se-deficient two-dimensional MoSe₂," *ACS Nano*, vol. 9, no. 3, pp. 3274–3283, 2015.
- [70] A. Roy, H. C. P. Movva, B. Satpati, K. Kim, R. Dey, A. Rai, T. Pramanik, S. Guchhait, E. Tutuc, and S. K. Banerjee, "Structural and electrical properties of MoTe₂ and MoSe₂ grown by Molecular Beam Epitaxy," *ACS Applied Materials & Interfaces*, vol. 8, no. 11, pp. 7396–7402, 2016.
- [71] S. Barja, S. Wickenburg, Z.-F. Liu, Y. Zhang, H. Ryu, M. M. Ugeda, Z. Hussain, Z.-X. Shen, S.-K. Mo, E. Wong, M. B. Salmeron, F. Wang, M. F. Crommie, D. F. Ogletree, J. B. Neaton, and A. Weber-Bargioni, "Charge density wave order in 1D mirror twin boundaries of single-layer MoSe₂," *Nature Physics*, vol. 12, no. 8, pp. 751–756, 2016.
- [72] A. M. van der Zande, P. Y. Huang, D. A. Chenet, T. C. Berkelbach, Y. You, G.-H. Lee, T. F. Heinz, D. R. Reichman, D. A. Muller, and J. C. Hone, "Grains and grain boundaries in highly crystalline monolayer molybdenum disulphide," *Nature Materials*, vol. 12, no. 6, pp. 554–561, 2013.
- [73] S. Najmaei, Z. Liu, W. Zhou, X. Zou, G. Shi, S. Lei, B. I. Yakobson, J.-C. Idrobo, P. M. Ajayan, and J. Lou, "Vapour phase growth and grain boundary structure of molybdenum disulphide atomic layers," *Nature Materials*, vol. 12, no. 8, pp. 754–759, 2013.
- [74] S. Najmaei, M. Amani, M. L. Chin, Z. Liu, A. G. Birdwell, T. P. O'Regan, P. M. Ajayan, M. Dubey, and J. Lou, "Electrical transport properties of polycrystalline monolayer molybdenum disulfide," *ACS Nano*, vol. 8, no. 8, pp. 7930–7937, 2014.
- [75] H. Schmidt, S. Wang, L. Chu, M. Toh, R. Kumar, W. Zhao, A. H. Castro Neto, J. Martin, S. Adam, B. Özyilmaz, and G. Eda, "Transport properties of monolayer MoS₂ grown by chemical vapor deposition," *Nano Letters*, vol. 14, no. 4, pp. 1909–1913, 2014.
- [76] J. W. Chung, Z. R. Dai, and F. S. Ohuchi, "WS₂ thin films by metal organic chemical vapor deposition," *Journal of Crystal Growth*, vol. 186, no. 1, pp. 137–150, 1998.

Bibliography

- [77] K. Kang, S. Xie, L. Huang, Y. Han, P. Y. Huang, K. F. Mak, C.-J. Kim, D. Muller, and J. Park, “High-mobility three-atom-thick semiconducting films with wafer-scale homogeneity,” *Nature*, vol. 520, no. 7549, pp. 656–660, 2015.
- [78] C. Huang, S. Wu, A. M. Sanchez, J. J. P. Peters, R. Beanland, J. S. Ross, P. Rivera, W. Yao, D. H. Cobden, and X. Xu, “Lateral heterojunctions within monolayer MoSe_2 – WSe_2 semiconductors,” *Nature Materials*, vol. 13, no. 12, pp. 1096–1101, 2014.
- [79] X. Duan, C. Wang, J. C. Shaw, R. Cheng, Y. Chen, H. Li, X. Wu, Y. Tang, Q. Zhang, A. Pan, J. Jiang, R. Yu, Y. Huang, and X. Duan, “Lateral epitaxial growth of two-dimensional layered semiconductor heterojunctions,” *Nature Nanotechnology*, vol. 9, no. 12, pp. 1024–1030, 2014.
- [80] M.-Y. Li, Y. Shi, C.-C. Cheng, L.-S. Lu, Y.-C. Lin, H.-L. Tang, M.-L. Tsai, C.-W. Chu, K.-H. Wei, J.-H. He, W.-H. Chang, K. Suenaga, and L.-J. Li, “Epitaxial growth of a monolayer WSe_2 - MoS_2 lateral p-n junction with an atomically sharp interface,” *Science*, vol. 349, no. 6247, pp. 524–528, 2015.
- [81] Y. Chen, “Nanofabrication by electron beam lithography and its applications: A review,” *Microelectronic Engineering*, vol. 135, pp. 57–72, 2015.
- [82] K. Ueno, S. Nakamura, H. Shimotani, H. T. Yuan, N. Kimura, T. Nojima, H. Aoki, Y. Iwasa, and M. Kawasaki, “Discovery of superconductivity in KTaO_3 by electrostatic carrier doping,” *Nature Nanotechnology*, vol. 6, no. 7, pp. 408–412, 2011.
- [83] H. Yuan, H. Shimotani, A. Tsukazaki, A. Ohtomo, M. Kawasaki, and Y. Iwasa, “High-density carrier accumulation in ZnO field-effect transistors gated by electric double layers of ionic liquids,” *Adv. Funct. Mater.*, vol. 19, no. 7, pp. 1046–1053, 2009.
- [84] D. Braga, I. Gutiérrez Lezama, H. Berger, and A. F. Morpurgo, “Quantitative determination of the band gap of WS_2 with ambipolar ionic liquid-gated transistors,” *Nano Letters*, vol. 12, no. 10, pp. 5218–5223, 2012.
- [85] S. Jo, N. Ubrig, H. Berger, A. B. Kuzmenko, and A. F. Morpurgo, “Mono- and bilayer WS_2 light-emitting transistors,” *Nano Letters*, vol. 14, no. 4, pp. 2019–2025, 2014.
- [86] Y. Yu, F. Yang, X. F. Lu, Y. J. Yan, ChoYong-Heum, L. Ma, X. Niu, S. Kim, Y.-W. Son, D. Feng, S. Li, S.-W. Cheong, X. H. Chen, and Y. Zhang, “Gate-tunable phase transitions in thin flakes of 1T-TaS_2 ,” *Nature Nanotechnology*, vol. 10, no. 3, pp. 270–276, 2015.
- [87] P. Gallagher, M. Lee, T. A. Petach, S. W. Stanwyck, J. R. Williams, K. Watanabe, T. Taniguchi, and D. Goldhaber-Gordon, “A high-mobility electronic system at an electrolyte-gated oxide surface,” *Nature Communications*, vol. 6, 2015.

- [88] J. Pu, Y. Yomogida, K.-K. Liu, L.-J. Li, Y. Iwasa, and T. Takenobu, "Highly flexible MoS₂ thin-film transistors with ion gel dielectrics," *Nano Letters*, vol. 12, no. 8, pp. 4013–4017, 2012.
- [89] "<https://physik.uni-paderborn.de/en/lindner/research/temstem/>."
- [90] H. Sawada, T. Sasaki, F. Hosokawa, and K. Suenaga, "Atomic-resolution STEM imaging of graphene at low voltage of 30 kV with resolution enhancement by using large convergence angle," *Physical Review Letters*, vol. 114, no. 16, p. 166102, 2015.
- [91] O. L. Krivanek, M. F. Chisholm, V. Nicolosi, T. J. Pennycook, G. J. Corbin, N. Dellby, M. F. Murfitt, C. S. Own, Z. S. Szilagy, M. P. Oxley, S. T. Pantelides, and S. J. Pennycook, "Atom-by-atom structural and chemical analysis by annular dark-field electron microscopy," *Nature*, vol. 464, no. 7288, pp. 571–574, 2010.
- [92] D. B. Williams and C. B. Carter, *Transmission Electron Microscopy*. Boston, MA: Springer US, 2009. DOI: 10.1007/978-0-387-76501-3.
- [93] W. Melitz, J. Shen, A. C. Kummel, and S. Lee, "Kelvin probe force microscopy and its application," *Surface Science Reports*, vol. 66, no. 1, pp. 1–27, 2011.
- [94] V. Panchal, R. Pearce, R. Yakimova, A. Tzalenchuk, and O. Kazakova, "Standardization of surface potential measurements of graphene domains," *Scientific Reports*, vol. 3, p. 2597, 2013.
- [95] A. L. Elías, N. Perea-López, A. Castro-Beltrán, A. Berkdemir, R. Lv, S. Feng, A. D. Long, T. Hayashi, Y. A. Kim, M. Endo, H. R. Gutiérrez, N. R. Pradhan, L. Balicas, T. E. Mallouk, F. López-Urías, H. Terrones, and M. Terrones, "Controlled synthesis and transfer of large-area WS₂ sheets: from single layer to few layers," *ACS Nano*, vol. 7, no. 6, pp. 5235–5242, 2013.
- [96] Z. Y. Zhu, Y. C. Cheng, and U. Schwingenschlögl, "Giant spin-orbit-induced spin splitting in two-dimensional transition-metal dichalcogenide semiconductors," *Physical Review B*, vol. 84, no. 15, 2011.
- [97] K. F. Mak, K. L. McGill, J. Park, and P. L. McEuen, "The valley Hall effect in MoS₂ transistors," *Science*, vol. 344, no. 6191, pp. 1489–1492, 2014.
- [98] L. Liu, S. B. Kumar, Y. Ouyang, and J. Guo, "Performance limits of monolayer transition metal dichalcogenide transistors," *IEEE Transactions on Electron Devices*, vol. 58, no. 9, pp. 3042–3047, 2011.

Bibliography

- [99] Z. Wu, S. Xu, H. Lu, A. Khamoshi, G.-B. Liu, T. Han, Y. Wu, J. Lin, G. Long, Y. He, Y. Cai, Y. Yao, F. Zhang, and N. Wang, “Even–odd layer-dependent magnetotransport of high-mobility Q-valley electrons in transition metal disulfides,” *Nature Communications*, vol. 7, p. 12955, 2016.
- [100] H. Qiu, T. Xu, Z. Wang, W. Ren, H. Nan, Z. Ni, Q. Chen, S. Yuan, F. Miao, F. Song, G. Long, Y. Shi, L. Sun, J. Wang, and X. Wang, “Hopping transport through defect-induced localized states in molybdenum disulphide,” *Nature Communications*, vol. 4, p. 2642, 2013.
- [101] Z. Yu, Y. Pan, Y. Shen, Z. Wang, Z.-Y. Ong, T. Xu, R. Xin, L. Pan, B. Wang, L. Sun, J. Wang, G. Zhang, Y. W. Zhang, Y. Shi, and X. Wang, “Towards intrinsic charge transport in monolayer molybdenum disulfide by defect and interface engineering,” *Nature Communications*, vol. 5, p. 5290, 2014.
- [102] B. Radisavljevic and A. Kis, “Mobility engineering and a metal-insulator transition in monolayer MoS₂,” *Nature Materials*, vol. 12, pp. 815–820, 2013.
- [103] B. Fallahazad, H. C. Movva, K. Kim, S. Larentis, T. Taniguchi, K. Watanabe, S. K. Banerjee, and E. Tutuc, “Shubnikov-de Haas oscillations of high-mobility holes in monolayer and bilayer WSe₂: Landau level degeneracy, effective mass, and negative compressibility,” *Physical Review Letters*, vol. 116, no. 8, p. 086601, 2016.
- [104] D. Jariwala, V. K. Sangwan, D. J. Late, J. E. Johns, V. P. Dravid, T. J. Marks, L. J. Lauhon, and M. C. Hersam, “Band-like transport in high mobility unencapsulated single-layer MoS₂ transistors,” *Applied Physics Letters*, vol. 102, no. 17, pp. –, 2013.
- [105] B. W. H. Baugher, H. O. H. Churchill, Y. Yang, and P. Jarillo-Herrero, “Intrinsic electronic transport properties of high-quality monolayer and bilayer MoS₂,” *Nano Letters*, vol. 13, no. 9, pp. 4212–4216, 2013.
- [106] F. Withers, T. H. Bointon, D. C. Hudson, M. F. Craciun, and S. Russo, “Electron transport of WS₂ transistors in a hexagonal boron nitride dielectric environment,” *Scientific Reports*, vol. 4, p. 4967, 2014.
- [107] Q. Yue, Z. Shao, S. Chang, and J. Li, “Adsorption of gas molecules on monolayer MoS₂ and effect of applied electric field,” *Nanoscale Research Letters*, vol. 8, no. 1, p. 425, 2013.
- [108] R. Fivaz and E. Mooser, “Mobility of charge carriers in semiconducting layer structures,” *Physical Review*, vol. 163, no. 3, pp. 743–755, 1967.

- [109] S. H. El-Mahalawy and B. L. Evans, "Temperature dependence of the electrical conductivity and hall coefficient in 2h-MoS₂, MoSe₂, WSe₂, and MoTe₂," *physica status solidi (b)*, vol. 79, no. 2, pp. 713–722, 1977.
- [110] W. Sik Hwang, M. Remskar, R. Yan, V. Protasenko, K. Tahy, S. Doo Chae, P. Zhao, A. Konar, H. (Grace) Xing, A. Seabaugh, and D. Jena, "Transistors with chemically synthesized layered semiconductor WS₂ exhibiting 10⁵ room temperature modulation and ambipolar behavior," *Applied Physics Letters*, vol. 101, no. 1, p. 013107, 2012.
- [111] W. Zhu, T. Low, Y.-H. Lee, H. Wang, D. B. Farmer, J. Kong, F. Xia, and P. Avouris, "Electronic transport and device prospects of monolayer molybdenum disulphide grown by chemical vapour deposition," *Nature Communications*, vol. 5, p. 3087, 2014.
- [112] K. Kaasbjerg, K. S. Thygesen, and K. W. Jacobsen, "Phonon-limited mobility in n-type single-layer MoS₂ from first principles," *Physical Review B*, vol. 85, no. 11, p. 115317, 2012.
- [113] K. Kaasbjerg, K. S. Thygesen, and A.-P. Jauho, "Acoustic phonon limited mobility in two-dimensional semiconductors: Deformation potential and piezoelectric scattering in monolayer MoS₂ from first principles," *Physical Review B*, vol. 87, no. 23, p. 235312, 2013.
- [114] N. Ma and D. Jena, "Charge scattering and mobility in atomically thin semiconductors," *Physical Review X*, vol. 4, no. 1, p. 011043, 2014.
- [115] Z.-Y. Ong and M. V. Fischetti, "Mobility enhancement and temperature dependence in top-gated single-layer MoS₂," *Physical Review B*, vol. 88, no. 16, p. 165316, 2013.
- [116] A. Lösche, "N. F. Mott, E. A. Davis. Electronic processes in non-crystalline materials," *Kristall und Technik*, vol. 7, no. 4, pp. K55–K56, 1972.
- [117] F. W. Van Keuls, X. L. Hu, H. W. Jiang, and A. J. Dahm, "Screening of the Coulomb interaction in two-dimensional variable-range hopping," *Physical Review B*, vol. 56, no. 3, pp. 1161–1169, 1997.
- [118] S. Ghatak, A. N. Pal, and A. Ghosh, "Nature of electronic states in atomically thin MoS₂ field-effect transistors," *ACS Nano*, vol. 5, no. 10, pp. 7707–7712, 2011.
- [119] Y. Cui, R. Xin, Z. Yu, Y. Pan, Z.-Y. Ong, X. Wei, J. Wang, H. Nan, Z. Ni, Y. Wu, T. Chen, Y. Shi, B. Wang, G. Zhang, Y.-W. Zhang, and X. Wang, "High-performance monolayer WS₂ field-effect transistors on high- κ dielectrics," *Advanced Materials*, vol. 27, no. 35, pp. 5230–5234, 2015.

Bibliography

- [120] M. W. Iqbal, M. Z. Iqbal, M. F. Khan, M. A. Shehzad, Y. Seo, J. H. Park, C. Hwang, and J. Eom, "High-mobility and air-stable single-layer WS₂ field-effect transistors sandwiched between chemical vapor deposition-grown hexagonal BN films," *Scientific Reports*, vol. 5, p. 10699, 2015.
- [121] K. Ueno, S. Nakamura, H. Shimotani, A. Ohtomo, N. Kimura, T. Nojima, H. Aoki, Y. Iwasa, and M. Kawasaki, "Electric-field-induced superconductivity in an insulator," *Nature Materials*, vol. 7, pp. 855–858, Nov. 2008.
- [122] J. T. Ye, S. Inoue, K. Kobayashi, Y. Kasahara, H. T. Yuan, H. Shimotani, and Y. Iwasa, "Liquid-gated interface superconductivity on an atomically flat film," *Nature Materials*, vol. 9, no. 2, pp. 125–128, 2010.
- [123] T. Mimura, "The early history of the high electron mobility transistor (HEMT)," *IEEE Transactions on Microwave Theory and Techniques*, vol. 50, no. 3, pp. 780–782, 2002.
- [124] K. M. Burson, W. G. Cullen, S. Adam, C. R. Dean, K. Watanabe, T. Taniguchi, P. Kim, and M. S. Fuhrer, "Direct imaging of charged impurity density in common graphene substrates," *Nano Letters*, vol. 13, no. 8, pp. 3576–3580, 2013.
- [125] Y.-C. Lin, C.-C. Lu, C.-H. Yeh, C. Jin, K. Suenaga, and P.-W. Chiu, "Graphene annealing: How clean can it be?," *Nano Letters*, vol. 12, no. 1, pp. 414–419, 2012.
- [126] Y. Zhang, Y.-W. Tan, H. L. Stormer, and P. Kim, "Experimental observation of the quantum Hall effect and Berry's phase in graphene," *Nature*, vol. 438, no. 7065, pp. 201–204, 2005.
- [127] K. S. Novoselov, Z. Jiang, Y. Zhang, S. V. Morozov, H. L. Stormer, U. Zeitler, J. C. Maan, G. S. Boebinger, P. Kim, and A. K. Geim, "Room-temperature quantum Hall effect in graphene," *Science*, vol. 315, no. 5817, pp. 1379–1379, 2007.
- [128] C. R. Dean, A. F. Young, I. Meric, C. Lee, L. Wang, S. Sorgenfrei, K. Watanabe, T. Taniguchi, P. Kim, K. L. Shepard, and J. Hone, "Boron nitride substrates for high-quality graphene electronics," *Nature Nanotechnology*, vol. 5, no. 10, pp. 722–726, 2010.
- [129] I. Meric, C. R. Dean, N. Petrone, L. Wang, J. Hone, P. Kim, and K. L. Shepard, "Graphene field-effect transistors based on boron nitride dielectrics," *Proceedings of the IEEE*, vol. 101, no. 7, pp. 1609–1619, 2013.
- [130] L. Wang, Z. Chen, C. R. Dean, T. Taniguchi, K. Watanabe, L. E. Brus, and J. Hone, "Negligible environmental sensitivity of graphene in a hexagonal boron nitride/graphene/h-BN sandwich structure," *ACS Nano*, vol. 6, no. 10, pp. 9314–9319, 2012.

- [131] S. J. Haigh, A. Gholinia, R. Jalil, S. Romani, L. Britnell, D. C. Elias, K. S. Novoselov, L. A. Ponomarenko, A. K. Geim, and R. Gorbachev, "Cross-sectional imaging of individual layers and buried interfaces of graphene-based heterostructures and superlattices," *Nature Materials*, vol. 11, no. 9, pp. 764–767, 2012.
- [132] H. C. P. Movva, A. Rai, S. Kang, K. Kim, B. Fallahazad, T. Taniguchi, K. Watanabe, E. Tutuc, and S. K. Banerjee, "High-mobility holes in dual-gated WSe₂ field-effect transistors," *ACS Nano*, vol. 9, no. 10, pp. 10402–10410, 2015.
- [133] B. Chamlagain, Q. Li, N. J. Ghimire, H.-J. Chuang, M. M. Perera, H. Tu, Y. Xu, M. Pan, D. Xiaio, J. Yan, D. Mandrus, and Z. Zhou, "Mobility improvement and temperature dependence in MoSe₂ field-effect transistors on parylene-c substrate," *ACS Nano*, vol. 8, no. 5, pp. 5079–5088, 2014.
- [134] Y. Saito and Y. Iwasa, "Ambipolar insulator-to-metal transition in black phosphorus by ionic-liquid gating," *ACS Nano*, vol. 9, no. 3, pp. 3192–3198, 2015.
- [135] L. Li, G. J. Ye, V. Tran, R. Fei, G. Chen, H. Wang, J. Wang, K. Watanabe, T. Taniguchi, L. Yang, X. H. Chen, and Y. Zhang, "Quantum oscillations in a two-dimensional electron gas in black phosphorus thin films," *Nature Nanotechnology*, vol. 10, no. 7, pp. 608–613, 2015.
- [136] L. Li, F. Yang, G. J. Ye, Z. Zhang, Z. Zhu, W. Lou, X. Zhou, L. Li, K. Watanabe, T. Taniguchi, K. Chang, Y. Wang, X. H. Chen, and Y. Zhang, "Quantum Hall effect in black phosphorus two-dimensional electron system," *Nature Nanotechnology*, vol. 11, no. 7, pp. 593–597, 2016.
- [137] G. Long, D. Maryenko, J. Shen, S. Xu, J. Hou, Z. Wu, W. K. Wong, T. Han, J. Lin, Y. Cai, R. Lortz, and N. Wang, "Achieving ultrahigh carrier mobility in two-dimensional hole gas of black phosphorus," *Nano Letters*, vol. 16, no. 12, pp. 7768–7773, 2016.
- [138] H. Li, J. Wu, X. Huang, Z. Yin, J. Liu, and H. Zhang, "A universal, rapid method for clean transfer of nanostructures onto various substrates," *ACS Nano*, vol. 8, no. 7, pp. 6563–6570, 2014.
- [139] Y.-C. Lin, H.-P. Komsa, C.-H. Yeh, T. Björkman, Z.-Y. Liang, C.-H. Ho, Y.-S. Huang, P.-W. Chiu, A. V. Krasheninnikov, and K. Suenaga, "Single-layer ReS₂: Two-dimensional semiconductor with tunable in-plane anisotropy," *ACS Nano*, 2015.
- [140] P. Blake, E. W. Hill, A. H. C. Neto, K. S. Novoselov, D. Jiang, R. Yang, T. J. Booth, and A. K. Geim, "Making graphene visible," *Applied Physics Letters*, 2007.

Bibliography

- [141] M. M. Benameur, B. Radisavljevic, J. S. Héron, S. Sahoo, H. Berger, and A. Kis, “Visibility of dichalcogenide nanolayers,” *Nanotechnology*, vol. 22, no. 12, p. 125706, 2011.
- [142] C. M. Corbet, C. McClellan, A. Rai, S. S. Sonde, E. Tutuc, and S. K. Banerjee, “Field effect transistors with current saturation and voltage gain in ultrathin ReS₂,” *ACS Nano*, 2014.
- [143] E. Liu, Y. Fu, Y. Wang, Y. Feng, H. Liu, X. Wan, W. Zhou, B. Wang, L. Shao, C.-H. Ho, Y.-S. Huang, Z. Cao, L. Wang, A. Li, J. Zeng, F. Song, X. Wang, Y. Shi, H. Yuan, H. Y. Hwang, Y. Cui, F. Miao, and D. Xing, “Integrated digital inverters based on two-dimensional anisotropic ReS₂ field-effect transistors,” *F*, vol. 6, 2015.
- [144] M. Rahman, K. Davey, and S.-Z. Qiao, “Advent of 2d rhenium disulfide (ReS₂): Fundamentals to applications,” *Advanced Functional Materials*, 2017.
- [145] Y. Yomogida, J. Pu, H. Shimotani, S. Ono, S. Hotta, Y. Iwasa, and T. Takenobu, “Ambipolar organic single-crystal transistors based on ion gels,” *Advanced Materials*, vol. 24, no. 32, pp. 4392–4397, 2012.
- [146] C. Ho, M. Hsieh, C. Wu, Y. Huang, and K. Tiong, “Dichroic optical and electrical properties of rhenium dichalcogenides layer compounds,” *Journal of Alloys and Compounds*, vol. 442, no. 1–2, pp. 245–248, 2007.
- [147] N. R. Pradhan, A. McCreary, D. Rhodes, Z. Lu, S. Feng, E. Manousakis, D. Smirnov, R. Namburu, M. Dubey, A. R. H. Walker, H. Terrones, M. Terrones, V. Dobrosavljevic, and L. Balicas, “Metal to insulator quantum-phase transition in few-layered ReS₂,” *Nano Letters*, vol. 15, no. 12, pp. 8377–8384, 2015.
- [148] H. Shibata and J.-i. Oide, “Analysis of the Hall effect device using an anisotropic material,” *Journal of Applied Physics*, vol. 88, no. 8, pp. 4813–4817, 2000.
- [149] W L V Price, “Extension of van der Pauw’s theorem for measuring specific resistivity in discs of arbitrary shape to anisotropic media,” *Journal of Physics D: Applied Physics*, vol. 5, no. 6, p. 1127, 1972.
- [150] Y.-H. Chang, W. Zhang, Y. Zhu, Y. Han, J. Pu, J.-K. Chang, W.-T. Hsu, J.-K. Huang, C.-L. Hsu, M.-H. Chiu, T. Takenobu, H. Li, C.-I. Wu, W.-H. Chang, A. T. S. Wee, and L.-J. Li, “Monolayer MoSe₂ grown by chemical vapor deposition for fast photodetection,” *ACS Nano*, vol. 8, no. 8, pp. 8582–8590, 2014.
- [151] J.-K. Huang, J. Pu, C.-L. Hsu, M.-H. Chiu, Z.-Y. Juang, Y.-H. Chang, W.-H. Chang, Y. Iwasa, T. Takenobu, and L.-J. Li, “Large-area synthesis of highly crystalline WSe₂ monolayers and device applications,” *ACS Nano*, vol. 8, no. 1, pp. 923–930, 2014.

- [152] A. G. Zabrodskii, "The coulomb gap: The view of an experimenter," *Philosophical Magazine Part B*, vol. 81, no. 9, pp. 1131–1151, 2001.
- [153] N. F. Mott, "Conduction in non-crystalline materials," *Philosophical Magazine*, vol. 19, no. 160, pp. 835–852, 1969.
- [154] K. Shimakawa, "Multiphonon hopping of electrons on defect clusters in amorphous germanium," *Phys. Rev. B*, vol. 39, no. 17, pp. 12933–12936, 1989.
- [155] I. Zvyagin, "Multiphonon hopping in disordered semiconductors," *Soviet Physics Journal*, vol. 19, no. 2, pp. 162–167, 1976.
- [156] Somaditya Sen and A Ghosh, "Multiphonon assisted hopping in strontium vanadate semiconducting glasses," *Journal of Physics: Condensed Matter*, vol. 11, no. 6, p. 1529, 1999.
- [157] S. Bhattacharya, B. K. Chaudhuri, and H. Sakata, "Multiphonon hopping conduction in nonconventional chromium-doped $\text{Bi}_3\text{Pb}_1\text{Sr}_3\text{Ca}_3\text{Cu}_{4-n}\text{Cr}_n\text{O}_x$ ($n=0.025-0.2$) glasses with nanocrystalline particles and clusters," *Journal of Applied Physics*, vol. 88, no. 9, pp. 5033–5042, 2000.
- [158] T. Serin, A. Yildiz, Ş. Şahin, and N. Serin, "Multiphonon hopping of carriers in CuO thin films," *Physica B: Condensed Matter*, vol. 406, no. 19, pp. 3551–3555, 2011.
- [159] W. Xie, S. Wang, X. Zhang, C. Leighton, and C. D. Frisbie, "High conductance 2D transport around the Hall mobility peak in electrolyte-gated rubrene crystals," *Phys. Rev. Lett.*, vol. 113, no. 24, p. 246602, 2014. 00003.
- [160] S.-i. Machida, Y. Nakayama, S. Duhm, Q. Xin, A. Funakoshi, N. Ogawa, S. Kera, N. Ueno, and H. Ishii, "Highest-occupied-molecular-orbital band dispersion of rubrene single crystals as observed by angle-resolved ultraviolet photoelectron spectroscopy," *Phys. Rev. Lett.*, vol. 104, no. 15, p. 156401, 2010.
- [161] Y. Xia, W. Xie, P. P. Ruden, and C. D. Frisbie, "Carrier localization on surfaces of organic semiconductors gated with electrolytes," *Phys. Rev. Lett.*, vol. 105, no. 3, p. 036802, 2010.
- [162] W. Xie, F. Liu, S. Shi, P. P. Ruden, and C. D. Frisbie, "Charge density dependent two-channel conduction in organic electric double layer transistors (EDLTs)," *Advanced Materials*, vol. 26, no. 16, pp. 2527–2532, 2014.
- [163] E. Abrahams, P. W. Anderson, D. C. Licciardello, and T. V. Ramakrishnan, "Scaling theory of localization: absence of quantum diffusion in two dimensions," *Phys. Rev. Lett.*, vol. 42, no. 10, pp. 673–676, 1979.

Bibliography

- [164] P. W. Anderson, "Absence of diffusion in certain random lattices," *Phys. Rev.*, vol. 109, no. 5, pp. 1492–1505, 1958.
- [165] F. Gargiulo, G. Autès, N. Virk, S. Barthel, M. Rösner, M. Toller, Lisa R. T. O. Wehling, and O. V. Yazyev, "Electronic transport in graphene with aggregated hydrogen adatoms," *Phys. Rev. Lett.*, vol. 113, no. 24, p. 246601, 2014.
- [166] E. N. Economou, *Green's Functions in Quantum Physics*, vol. 7 of *Springer Series in Solid-State Sciences*. Berlin, Heidelberg: Springer Berlin Heidelberg, 2006.
- [167] F. Evers and A. D. Mirlin, "Anderson transitions," *Rev. Mod. Phys.*, vol. 80, no. 4, pp. 1355–1417, 2008.
- [168] R. Kubo, "Statistical-mechanical theory of irreversible processes. I. general theory and simple applications to magnetic and conduction problems," *J. Phys. Soc. Jpn.*, vol. 12, no. 6, pp. 570–586, 1957.
- [169] F. Gargiulo, C. A. Perroni, V. M. Ramaglia, and V. Cataudella, "Electronic transport within a quasi-two-dimensional model for rubrene single-crystal field effect transistors," *Phys. Rev. B*, vol. 84, no. 24, p. 245204, 2011.
- [170] Z. Chen, H. Yuan, Y. Xie, D. Lu, H. Inoue, Y. Hikita, C. Bell, and H. Y. Hwang, "Dual-gate modulation of carrier density and disorder in an oxide two-dimensional electron system," *Nano Letters*, vol. 16, no. 10, pp. 6130–6136, 2016.
- [171] K. Friemelt, M.-C. Lux-Steiner, and E. Bucher, "Optical properties of the layered transition-metal-dichalcogenide ReS_2 : Anisotropy in the van der Waals plane," *Journal of Applied Physics*, vol. 74, no. 8, pp. 5266–5268, 1993.
- [172] C. H. Ho, P. C. Yen, Y. S. Huang, and K. K. Tiong, "Photoreflectance study of the excitonic transitions of rhenium disulphide layer compounds," *Phys. Rev. B*, vol. 66, no. 24, p. 245207, 2002.
- [173] B. Radisavljevic, M. B. Whitwick, and A. Kis, "Integrated circuits and logic operations based on single-layer MoS_2 ," *ACS Nano*, vol. 5, pp. 9934–9938, 2011.
- [174] H. I. Rasool, C. Ophus, W. S. Klug, A. Zettl, and J. K. Gimzewski, "Measurement of the intrinsic strength of crystalline and polycrystalline graphene," *Nature Communications*, vol. 4, p. 2811, 2013.
- [175] K. Q. Dang and D. E. Spearot, "Effect of point and grain boundary defects on the mechanical behavior of monolayer MoS_2 under tension via atomistic simulations," *Journal of Applied Physics*, 2014.

- [176] T. H. Ly, J. Zhao, M. O. Cichocka, L.-J. Li, and Y. H. Lee, "Dynamical observations on the crack tip zone and stress corrosion of two-dimensional MoS₂," *Nature Communications*, vol. 8, p. 14116, 2017.
- [177] M. Gonschorek, J.-F. Carlin, E. Feltin, M. A. Py, and N. Grandjean, "High electron mobility lattice-matched AlInN-GaN field-effect transistor heterostructures," *Applied Physics Letters*, vol. 89, no. 6, p. 062106, 2006.
- [178] Y. Yu, C. Li, Y. Liu, L. Su, Y. Zhang, and L. Cao, "Controlled scalable synthesis of uniform, high-quality monolayer and few-layer MoS₂ films," *Scientific Reports*, vol. 3, p. 1866, 2013.
- [179] Y. Zhang, Y. Zhang, Q. Ji, J. Ju, H. Yuan, J. Shi, T. Gao, D. Ma, M. Liu, Y. Chen, X. Song, H. Y. Hwang, Y. Cui, and Z. Liu, "Controlled growth of high-quality monolayer WS₂ layers on sapphire and imaging its grain boundary," *ACS Nano*, vol. 7, no. 10, pp. 8963–8971, 2013.
- [180] M. Yoshimoto, T. Maeda, T. Ohnishi, H. Koinuma, O. Ishiyama, M. Shinohara, M. Kubo, R. Miura, and A. Miyamoto, "Atomic-scale formation of ultrasoft surfaces on sapphire substrates for high-quality thin-film fabrication," *Applied Physics Letters*, vol. 67, no. 18, pp. 2615–2617, 1995.
- [181] S. Curiotto and D. Chatain, "Surface morphology and composition of c-, a- and m-sapphire surfaces in O₂ and H₂ environments," *Surface Science*, vol. 603, no. 17, pp. 2688–2697, 2009.
- [182] J. Brivio, D. T. L. Alexander, and A. Kis, "Ripples and layers in ultrathin MoS₂ membranes," *Nano Letters*, vol. 11, pp. 5148–5153, 2011.
- [183] M. Nonnenmacher, M. P. O'Boyle, and H. K. Wickramasinghe, "Kelvin probe force microscopy," *Applied Physics Letters*, vol. 58, no. 25, pp. 2921–2923, 1991.
- [184] Y.-J. Yu, Y. Zhao, S. Ryu, L. E. Brus, K. S. Kim, and P. Kim, "Tuning the graphene work function by electric field effect," *Nano Letters*, vol. 9, no. 10, pp. 3430–3434, 2009.
- [185] G. Hao, Z. Huang, Y. Liu, X. Qi, L. Ren, X. Peng, L. Yang, X. Wei, and J. Zhong, "Electrostatic properties of few-layer MoS₂ films," *AIP Advances*, vol. 3, no. 4, p. 042125, 2013.
- [186] O. L. Sanchez, D. Ovchinnikov, S. Misra, A. Allain, and A. Kis, "Valley polarization by spin injection in a light-emitting van der Waals heterojunction," *Nano Letters*, vol. 16, pp. 5792–5797, 2016.

Bibliography

- [187] H. Kim, D. Dumcenco, M. Frégnaux, A. Benayad, M.-W. Chen, Y.-C. Kung, A. Kis, and O. Renault, “Free-standing electronic character of monolayer MoS₂ in van der Waals epitaxy,” *Physical Review B*, vol. 94, no. 8, p. 081401, 2016.
- [188] A. A. Mitioglu, K. Galkowski, A. Surrente, L. Klotkowski, D. Dumcenco, A. Kis, D. K. Maude, and P. Plochocka, “Magnetoexcitons in large area CVD-grown monolayer MoS₂ and MoSe₂ on sapphire,” *Physical Review B*, vol. 93, no. 16, p. 165412, 2016.
- [189] J. Feng, K. Liu, M. Graf, D. Ovchinnikov, A. Kis, and A. Radenovic, “Single-layer MoS₂ nanopores as nanopower generators,” *Nature*, vol. 536, pp. 197–200, 2016.
- [190] R. Zan, Q. M. Ramasse, R. Jalil, T. Georgiou, U. Bangert, and K. S. Novoselov, “Control of radiation damage in MoS₂ by graphene encapsulation,” *ACS Nano*, vol. 7, pp. 10167–10174, Nov. 2013.
- [191] W. Zhou, X. Zou, S. Najmaei, Z. Liu, Y. Shi, J. Kong, J. Lou, P. M. Ajayan, B. I. Yakobson, and J.-C. Idrobo, “Intrinsic structural defects in monolayer molybdenum disulfide,” *Nano Letters*, vol. 13, no. 6, pp. 2615–2622, 2013.
- [192] H. Wang, Z. Lu, S. Xu, D. Kong, J. J. Cha, G. Zheng, P.-C. Hsu, K. Yan, D. Bradshaw, F. B. Prinz, and Y. Cui, “Electrochemical tuning of vertically aligned MoS₂ nanofilms and its application in improving hydrogen evolution reaction,” *Proceedings of the National Academy of Sciences*, vol. 110, no. 49, pp. 19701–19706, 2013.
- [193] E. Ponomarev, I. Gutiérrez-Lezama, N. Ubrig, and A. F. Morpurgo, “Ambipolar light-emitting transistors on chemical vapor deposited monolayer MoS₂,” *Nano Letters*, vol. 15, no. 12, pp. 8289–8294, 2015.
- [194] M. R. Laskar, D. N. Nath, L. Ma, E. W. L. II, C. H. Lee, T. Kent, Z. Yang, R. Mishra, M. A. Roldan, J.-C. Idrobo, S. T. Pantelides, S. J. Pennycook, R. C. Myers, Y. Wu, and S. Rajan, “p-type doping of MoS₂ thin films using Nb,” *Applied Physics Letters*, 2014.
- [195] J. Suh, T.-E. Park, D.-Y. Lin, D. Fu, J. Park, H. J. Jung, Y. Chen, C. Ko, C. Jang, Y. Sun, R. Sinclair, J. Chang, S. Tongay, and J. Wu, “Doping against the native propensity of MoS₂: Degenerate hole doping by cation substitution,” *Nano Letters*, vol. 14, no. 12, pp. 6976–6982, 2014.
- [196] G. Froehlicher and S. Berciaud, “Raman spectroscopy of electrochemically gated graphene transistors: Geometrical capacitance, electron-phonon, electron-electron, and electron-defect scattering,” *Physical Review B*, vol. 91, no. 20, p. 205413, 2015.
- [197] X. Wang, Y. Gong, G. Shi, W. L. Chow, K. Keyshar, G. Ye, R. Vajtai, J. Lou, Z. Liu, E. Ringe, B. K. Tay, and P. M. Ajayan, “Chemical vapor deposition growth of crystalline monolayer MoSe₂,” *ACS Nano*, vol. 8, no. 5, pp. 5125–5131, 2014.

-
- [198] E. Gourmelon, J. C. Bernède, J. Pouzet, and S. Marsillac, “Textured MoS₂ thin films obtained on tungsten: Electrical properties of the W/MoS₂ contact,” *Journal of Applied Physics*, 2000.
- [199] A. Dankert, L. Langouche, M. V. Kamalakar, and S. P. Dash, “High-performance molybdenum disulfide field-effect transistors with spin tunnel contacts,” *ACS Nano*, vol. 8, no. 1, pp. 476–482, 2014.
- [200] C. Maurel, R. Coratger, F. Ajustron, J. Beauvillain, and P. Gerard, “Electrical characteristics of metal/semiconductor nanocontacts using light emission in a scanning tunneling microscope,” *Journal of Applied Physics*, 2003.
- [201] S. Das, H.-Y. Chen, A. V. Penumatcha, and J. Appenzeller, “High performance multi-layer MoS₂ transistors with scandium contacts,” *Nano Letters*, vol. 13, no. 1, pp. 100–105, 2013.
- [202] Y. Guo, D. Liu, and J. Robertson, “Chalcogen vacancies in monolayer transition metal dichalcogenides and Fermi level pinning at contacts,” *Applied Physics Letters*, 2015.
- [203] X. Lu, M. I. B. Utama, J. Lin, X. Gong, J. Zhang, Y. Zhao, S. T. Pantelides, J. Wang, Z. Dong, Z. Liu, W. Zhou, and Q. Xiong, “Large-area synthesis of monolayer and few-layer MoSe₂ films on SiO₂ substrates,” *Nano Letters*, vol. 14, no. 5, pp. 2419–2425, 2014.
- [204] J. Lin, S. T. Pantelides, and W. Zhou, “Vacancy-induced formation and growth of inversion domains in transition-metal dichalcogenide monolayer,” *ACS Nano*, vol. 9, no. 5, pp. 5189–5197, 2015.
- [205] Z. Lin, B. R. Carvalho, E. Kahn, R. Lv, R. Rao, H. Terrones, M. A. Pimenta, and M. Terrones, “Defect engineering of two-dimensional transition metal dichalcogenides,” *2D Materials*, vol. 3, no. 2, p. 022002, 2016.
- [206] J. I.-J. Wang, Y. Yang, Y.-A. Chen, K. Watanabe, T. Taniguchi, H. O. H. Churchill, and P. Jarillo-Herrero, “Electronic transport of encapsulated graphene and WSe₂ devices fabricated by pick-up of prepatterned h-BN,” *Nano Letters*, vol. 15, no. 3, pp. 1898–1903, 2015.

List of Publications

Journal Articles

- D. Vella, D. Ovchinnikov, N. Martino, V. Vega-Mayoral, D. Dumcenco, Y.-C. Kung, M.-R. Antognazza, A. Kis, G. Lanzani, D. Mihailovic, C. Gadermaier "Unconventional electroabsorption in monolayer MoS₂", *2D Materials*, Volume 4, Number 2, 2017
- D. Dumcenco, D. Ovchinnikov, K. Marinov, A. Kis; "High-quality synthetic 2D transition metal dichalcogenide semiconductors", *46th European Solid-State Device Research Conference (ESSDERC)*, 2016
- G. Santoruvo, A. Allain, D. Ovchinnikov, E. Matioli "Magneto-ballistic transport in GaN nanowires", *Applied Physics Letters* 109 (10), 103102, 2016
- O. Lopez Sanchez, D. Ovchinnikov, S. Misra, A. Allain, A. Kis "Valley polarization by spin injection in a light-emitting van der Waals heterojunction", *Nano Letters* 16 (9), 5792-5797, 2016
- D. Ovchinnikov, F. Gargiulo, A. Allain, D. J. Pasquier, D. Dumcenco, C.-H. Ho, O. Yazyev, A. Kis "Disorder engineering and conductivity dome in ReS₂ with electrolyte gating", *Nature Communications* 7, Article number: 12391, 2016
- J. Feng, M. Graf, K. Liu, D. Ovchinnikov, D. Dumcenco, M. Heiranian, V. Nandigana, N. R. Aluru, A. Kis, A. Radenovic "Single-layer MoS₂ nanopores as nanopower generators", *Nature* 536, 197–200, 2016
- D. Dumcenco, D. Ovchinnikov, O. Lopez Sanchez, P. Gillet, D. T. L. Alexander, S. Lazar, A. Radenovic, A. Kis "Large-area MoS₂ grown using H₂S as the sulphur source", *2D Materials*, Volume 2, Number 4, 2015
- D. Dumcenco, D. Ovchinnikov, K. Marinov, P. Lazić, M. Gibertini, N. Marzari, O. Lopez Sanchez, Y.-C. Kung, D. Krasnozhon, M.-W. Chen, S. Bertolazzi, P. Gillet, A. Fontcuberta i Morral, A. Radenovic, A. Kis "Large Area Epitaxial Monolayer MoS₂", *ACS Nano*, 9 (4), pp 4611–4620, 2015

List of Publications

- D. Ovchinnikov, A. Allain, Y.-S. Huang, D. Dumcenco, A. Kis "Electrical Transport Properties of Single-Layer WS₂", *ACS Nano*, 8 (8), pp 8174–8181, 2014
- A. M. Markeev, A. G. Chernikova, A. A. Chouprik, S. A. Zaitsev, D. Ovchinnikov, H. Althues and S. Dorfler "Atomic layer deposition of Al₂O₃ and Al_xTi_{1-x}O_y thin films on N₂O plasma pretreated carbon materials", *J. Vac. Sci. Technol. A* 31, 01A135, 2013
- A. I. Soshnikov, K. S. Kravchuk, I. I. Maslenikov, D. Ovchinnikov, V. N. Reshetov "Measuring the local resistivity by the nanoindentation and force-spectroscopy methods", *Instruments and experimental techniques*, Volume 56, Issue 2, pp 233-239, March 2013

Journal Articles *submitted*

- S. Manzeli, D. Ovchinnikov, D. Pasquier, O. Yazyev, A. Kis "Two-dimensional Transition Metal Dichalcogenides" *Nature Review Materials*, *under review*.

Talks

- "Disorder engineering and conductivity dome in ReS₂ with polymer electrolyte gating" **Graphene 2017 (Barcelona, Spain, 2017)**
- "Structural and electrostatic disorder in 2D semiconductors" **Seminar at Moscow Institute of Physics and Technology, (Moscow, Russia, 2017)**
- "Electrical transport properties of ReS₂ with polymer electrolyte gating in the high-doping limit" **Flatlands Beyond Graphene 2016 (Bled, Slovenia, 2016)**
- "Electrical transport properties of ReS₂ with polymer electrolyte gating in the high-doping limit" **APS March 2016 Meeting (Baltimore, USA, 2016)**
- "Investigation of grain boundaries in CVD grown MoS₂" **MRS Fall 2015 Meeting (Boston, USA, 2015)**

Posters

- "Electrical Properties of Large-Area CVD MoS₂" **Flatlands Beyond Graphene 2015 (Tel-Aviv, Israel, 2015)**
- "Electrical transport properties of single-layer WS₂" **Flatlands Beyond Graphene 2014 (Dublin, Ireland, 2014)**

Curriculum Vitae

Address Route de Geneve 1, CH-1028, Preverenges

Email dmitry.ovchinnikov@epfl.ch

Professional Experience

01/13 – present **Laboratory of Nanoscale Electronics and Structures (LANES)**, EPFL, Lausanne
Doctoral assistant

09/11 – 12/12 **General Chemistry Department, Moscow Institute of Physics and Technology**, Moscow, Russia
Minor Research Scientist

09/08 – 08/11 **Technological Institute for Superhard and Novel Materials**, Moscow, Russia
Research Assistant

Education

01/13 – 04/17 **École Polytechnique Fédérale de Lausanne**, Lausanne
PhD in Microelectronics and microengineering

10/04 – 12/10 **Moscow Institute of Physics and Technology (State University)**, Moscow, Russia
M.Sc.

10/04 – 12/10 **Moscow Institute of Physics and Technology (State University)**, Moscow, Russia
B.Sc.

Research interests

2D materials
Electric double layer transistor (EDLT) characterization
Quantum transport
Electrostatic disorder
Ferromagnetic insulators
Scanning transmission electron microscopy (STEM)
Scanning probe microscopy (SPM)
Atomic layer deposition (ALD)

Technical Skills

Production of 2D crystals, extensive experience with CVD material
Heterostructure fabrication
Microfabrication skills - electron beam lithography, evaporation, etching, photolithography
(Scanning) Transmission Electron Microscopy ((S)TEM) with aberration correction
Kelvin Probe Force Microscopy (KPFM), Scanning Gate Microscopy (SGM)
EDLT based on variety of 2D crystals characterization
Charge transport as a function of temperature and magnetic fields
Microsoft Office, Igor Pro, LaTeX, Adobe Illustrator, Design CAD